

17 May 94 DEAN

Supervisor: Dr. J. McKenna
Co-Supervisor: Dr. D. Pitman

Measuring b-Fragmentation through the Decay $\bar{B}^0 \rightarrow D^{*+} l^- \bar{\nu}$
using the OPAL detector at CERN

by
Fan Liu

B.Sc., Tsinghua University, Beijing, P.R.China, 1991.

A thesis submitted in partial fulfillment
of the requirements for the degree of
Master of Science
in the Department of Physics and Astronomy.

We accept this thesis as conforming
to the required standard.

Dr. J. McKenna, Supervisor (Department of Physics and Astronomy, University of
British Columbia)

Dr. D. Pitman, Co-Supervisor (Department of Physics and Astronomy)

Dr. G. Beer, Departmental Member (Department of Physics and Astronomy)

Dr. M. Serra, Outside Member (Department of Computer Science)

Dr. T. Mattison, External Examiner (Stanford Linear Accelerator Center)

© Fan Liu, 1993
University of Victoria.

All rights reserved. This thesis may not be reproduced in whole or in part,
by photocopy or other means, without the permission of the author.

Supervisor: Dr. J. McKenna
Co-Supervisor: Dr. D. Pitman

Abstract

This thesis describes the b-quark fragmentation measured using B^0 mesons which arise from the decay of the Z^0 resonance, produced by e^+e^- annihilations. The data were collected by the OPAL detector at the LEP accelerator at CERN, Switzerland.

The B^0 meson is reconstructed through its decay $B^0 \rightarrow D^*l\nu$, in which $D^* \rightarrow D^0\pi$, followed by $D^0 \rightarrow K\pi$. The mean value of the fraction of the available energy carried by the primary b flavoured hadron is determined to be

$$\langle x_E \rangle_{B^0}^{e,\mu} = 0.741_{-0.028}^{+0.025+0.032}_{-0.016}$$

and

$$\langle x_E \rangle_{B^0}^{e,\mu} = 0.719_{-0.046}^{+0.034+0.011}_{-0.006}$$

using two different techniques.

The measurement is in excellent agreement with the previous measurements made by the OPAL collaboration obtained using inclusive muons from the b flavoured hadron decays which gives

$$\langle x_E \rangle_b^{\mu \text{ hadron}} = 0.726 \pm 0.007 \pm 0.022$$

The Peterson fragmentation function is a widely used parameterization for describing the heavy quark fragmentation process. The above result also yielded the Peterson fragmentation parameter ϵ_b for the b-quark to be:

$$\epsilon_b^{e,\mu} = 0.0019_{-0.0018}^{+0.0028+0.0026}_{-0.0051}$$

and

$$\epsilon_b^{e,\mu} = 0.0041_{-0.0033}^{+0.0070+0.0009}_{-0.0018}$$

corresponding to the two techniques presented in this thesis respectively. The measurement is also in good agreement with the previous measurement of $\epsilon_b^\mu = 0.0035$ by OPAL using inclusive muons from b hadron decays.

This analysis makes use of the reconstructed D^*l energy, which retains most of the B^0 energy, to estimate the fragmentation of the b-quark. Thus, the systematic error obtained for $\langle x_E \rangle_{B^0}$ measurement in this analysis is smaller compared to that of the previous analysis in which only the leptons from b hadron decays were used.

Preface

Examiners:

Dr. J. McKenna, Supervisor (Department of Physics and Astronomy, University of British Columbia)

Dr. D. Pitman, Co-Supervisor (Department of Physics and Astronomy)

Dr. G. Beer, Departmental Member (Department of Physics and Astronomy)

Dr. M. Serra, Outside Member (Department of Computer Science)

Dr. T. Mattison, External Examiner (Stanford Linear Accelerator Center)

that of the b -quark is often used to measure the $\langle z_E \rangle$. However, even though they are energetic, these leptons only carry away a small portion of the energy from the b -quark during the fragmentation process.

In the analysis presented here, the fragmentation of the b -quark is studied with the B^0 meson which is hadronized from b -quark. The B^0 meson is reconstructed through its decay $B^0 \rightarrow D^+ l^- \nu$. The analysis makes use of the reconstruction of the $D^+ l^-$ system which retains most of the B energy. Thus, a much smaller systematic error is obtained compared to that of the previous OPAL analysis.

The data were taken by the OPAL experiment at CERN between 1990 and 1992. The Monte Carlo simulated sample is used in this analysis to understand the kinematic features, the systematic errors and the efficiencies for the selection criteria for the chosen decay channel. The same set of selection criteria is then applied to the data.

This analysis measures the mean energy fraction taken away by the the B^0 meson from the b -quark, namely $\langle z_E \rangle_{B^0}$, and the ϵ_b in the Peterson fragmentation function, a widely used parameterization function for describing the heavy quark fragmentation.

Preface

The theory of *QCD* describes the strong interaction between quarks, and in particular, seeks to explain how hadrons are held together. The fragmentation of quarks into hadrons is of great importance in studying the theory of *QCD*. The precise description of the fragmentation process of a heavy quark must be calculated by non-perturbative *QCD* which is still under development. At present, this mechanism can only be investigated through the comparison of experimental measurements with the theoretical predictions. The b-quark fragmentation can be studied by measuring the mean energy fraction taken away by the the B^0 meson from the primary b-quark, namely $\langle x_E \rangle$. The Peterson fragmentation function is a widely used model to describe the fragmentation process of the b-quark.

Previous measurements have been done by the OPAL collaboration, using leptons from b flavoured hadron decay. Since the b-quark is very massive, the leptons from a b-quark decay can be very energetic. A lepton with high momentum and high transverse momentum can serve as a clear signature for the b-quark. Therefore, an extrapolation of the energy of an energetic lepton to that of the b-quark is often used to measure the $\langle x_E \rangle$. However, even though they are energetic, these leptons only carry away a small portion of the energy from the b-quark during the fragmentation process.

In the analysis presented here, the fragmentation of the b-quark is studied with the B^0 meson which is hadronized from b-quark. The B^0 meson is reconstructed through its decay $B^0 \rightarrow D^*l\nu$. The analysis makes use of the reconstruction of the D^*l system which retains most of the B energy. Thus, a much smaller systematic error is obtained compared to that of the previous OPAL analysis.

The data were taken by the OPAL experiment at CERN between 1990 and 1992. The Monte Carlo simulated sample is used in this analysis to understand the kinematic features, the systematic errors and the efficiencies for the selection criteria for the chosen decay channel. The same set of selection criteria is then applied to the data.

This analysis measures the mean energy fraction taken away by the the B^0 meson from the b-quark, namely $\langle x_E \rangle_{B^0}$, and the c_b in the Peterson fragmentation function, a widely used parameterization function for describing the heavy quark fragmentation.

This thesis work is based on my involvement with the OPAL collaboration at CERN starting in the summer of 1992, during which period I started the off-line data analysis for the b-quark fragmentation measurement. During the 7 months at CERN in the summers of 1992 and 1993, I was assigned shifts at the site of the OPAL experiment. I learned a lot about the data acquisition system and the running of a large particle physics experiment.

During the period while I was at CERN, I worked with many OPAL collaborators. By participating in the working group discussions, I was exposed to the off-line data analysis in high energy physics. I am grateful for this experience.

course made my first step in the field of experimental particle physics much more enjoyable, many thanks go to her for the detailed proofreading and great help with my English in preparing this thesis. Thanks Tom Mattson for the clear suggestions and many good comments to my thesis. Thanks Richard Keefer for his knowledge about the statistics.

I greatly appreciate the chance to work with my fellow office inmates for their insights and moral support. Special thanks to Johannes Steurer for many of the helpful hints, suggestions in physics as well as in computer techniques.

Finally, I want to thank Jia Hui for all his love, support, and patience over the past year.

Acknowledgments

This thesis would not have been possible without the help of a number of people. I am deeply indebted to my supervisor, Janis McKenna, for her helpful advice and guidance to my work, the patient chats and discussions as well as lots of the encouragements and care she has given me through out the past two and half years. I would like to thank my Co-supervisor, Dale Pitman, whose course made my first step in the field of experimental particle physics much more enjoyable, many thanks go to her for the detailed proofreading and great help with my English in preparing this thesis. Thanks Tom Mattison for the clear suggestions and many good comments to my thesis. Thanks Richard Keeler for his knowledge about the statistics.

I greatly appreciate the chance to work with my fellow office inmates for their insights and moral support. Special thanks to Johannes Steuerer for many of the helpful hints, suggestions in physics as well as in computer techniques.

Finally, I want to thank Jin Hui for all his love, support, and patience over the past year.

Table of Contents

Abstract	ii
Table of Contents	viii
<p>To my dear Grandma and Grandpa, to my mom, dad and my sister, to everyone in my big family for their great love and unfailing support which have led me to this point of my life. I am deeply indebted to them.</p>	
Preface	iv
Acknowledgement	vi
Dedication	vii
1 Introduction	1
1.1 The Standard Model	2
1.1.1 Fundamental Forces	2
1.1.2 Particles in the Standard Model	3
1.1.3 QCD	6
1.2 Background Knowledge for This Analysis	7
1.2.1 Z^0 Decay	7
1.2.2 The B^0 Meson and the Decay Channels Under Study	8
1.2.3 b-quark Fragmentation	10
2 The OPAL Detector	15
2.1 The Central Tracking System	16
2.1.1 The dE/dx Measurement	19
2.1.2 The dE/dx Weight	22

Table of Contents

Abstract	II
Table of Contents	VIII
List of Tables	XIV
List of Figures	XVIII
Preface	IV
Acknowledgement	VI
Dedication	VII
1 Introduction	1
1.1 The Standard Model	2
1.1.1 Fundamental Forces	2
1.1.2 Particles in the Standard Model	3
1.1.3 QCD	6
1.2 Background Knowledge for This Analysis	7
1.2.1 Z^0 Decay	7
1.2.2 The B^0 Meson and the Decay Channels Under Study	8
1.2.3 b-quark Fragmentation	10
2 The OPAL Detector	15
2.1 The Central Tracking System	16
2.1.1 The dE/dx Measurement	19
2.1.2 The dE/dx Weight	22

2.1.3	Track Resolution	23
2.2	ElectroMagnetic Calorimeter	24
2.3	Hadron Calorimeter	25
2.4	Muon Chambers	25
3	The Fragmentation of Heavy Mesons	27
3.1	The Region of Interest for the Fragmentation	27
3.2	Fragmentation Models	28
3.3	The Peterson Fragmentation Function	31
3.4	Experimental Evaluation of Heavy Quark Fragmentation Function .	
34		
4	Monte Carlo Study of Kinematics	39
4.1	JETSET and GOPAL	39
4.2	π Momentum	41
4.3	D^* Momentum	42
4.4	Kinematic Studies for Leptons	43
4.5	Some Kinematic Studies of the Background for D^*	45
5	Event Selection and B Reconstruction	51
5.1	Track Quality	52
5.2	Event Selection	53

5.2.1	D^* selection	54
5.2.2	Lepton Identification	57
5.3	The Efficiency and Purity of the Event Selection	58
5.3.1	Signal of D^* from B^0 decay	63
5.3.2	Background Estimation	65
5.3.3	Correction for the Missing ν Energy	67
6	x_E Measurement Using the Corrected B^0 Energy	73
6.1	The measurement of $x_E(B^0)$ distribution	74
6.1.1	Correction for muon efficiency	74
6.1.2	Correction for electron efficiency	79
6.1.3	Correction for the shift of the $\langle x_E \rangle$	81
6.1.4	Combining the D^*e and $D^*\mu$ Samples	82
6.2	Evaluation of the Systematic Error	84
7	x_E Measurement Using Only the D^*l Energy	92
7.1	Introduction	92
7.2	The measurement of $x_E(D^*l)$ distribution	93
7.3	Calculating the χ^2	95
7.4	Correcting for the D^{**} effect	97
7.5	The Systematic Error study	99

8 Discussion 105

9 Conclusion 112

List of Tables

Bibliography 115

Glossary 119

1.1 The Fundamental Forces in Nature. (The gravitational force is not included) 2

1.2 Some of the lowest-mass mesons constructed from quarks. 5

5.1 Efficiencies for track quality cuts on Monte Carlo Sample. Given in parentheses are percentages of tracks remained compared to previous selection after each cut 60

6.1 Number of Candidates for each $x_E(B^0)$ bins; these numbers have not been corrected for efficiencies. 77

6.2 Muon identification efficiencies for various muon momenta. 77

6.3 Efficiencies for each $x_E(B^0)$ bin for $D^*\mu$ events. 78

6.4 The Momentum Dependence of the Efficiencies. Note: p and p_1 in the Table are in GeV/c 81

6.5 Efficiencies for each $x_E(B^0)$ bin for D^*e events. 81

List of Tables

6.5	The numbers of B^0 events in each $x_E(B^0)$ bin after being corrected for lepton identification efficiencies and the efficiencies for selection.	83
6.6	The D^*e and the combined samples using the corrected B^0 energy.	84
6.7	The results for the $\langle x_E \rangle_{B^0}$ and ϵ_1 measurement for the D^*e , the $D^*\mu$ and the combined samples using the corrected B^0 energy.	85
<hr/>		
1.1	The Fundamental Forces in Nature. (The gravitational force is not included)	2
1.2	Some of the lowest-mass mesons constructed from quarks.	5
5.1	Efficiencies for track quality cuts on Monte Carlo Sample. Given in parentheses are percentages of tracks remained compared to previous selection after each cut	60
6.1	Number of Candidates for each $x_E(B^0)$ bins; these numbers have not been corrected for efficiencies.	77
6.2	Muon identification efficiencies for various muon momenta.	77
6.3	Efficiencies for each $x_E(B^0)$ bin for $D^*\mu$ events.	78
6.4	The Momentum Dependence of the Efficiencies. Note: p and p_t in the Table are in GeV/c	81
6.5	Efficiencies for each $x_E(B^0)$ bin for D^*e events.	81
	source for systematic error study.	102

6.6	The numbers of B^0 events in each $x_E(B^0)$ bin <i>after</i> being corrected for lepton identification efficiencies and the efficiencies for the event selection.	109
6.7	The results for the $\langle x_E \rangle_{B^0}$ and ϵ_b measurement for the D^*e , the $D^*\mu$ and the combined samples using the corrected B^0 energy.	83
6.8	Change in the $\langle x_E \rangle_{B^0}$ and the Peterson parameter ϵ_b from various sources of systematic uncertainties (D^*e)	90
6.9	Change in the $\langle x_E \rangle_{B^0}$ and the Peterson parameter ϵ_b from various sources of systematic uncertainties ($D^*\mu$)	91
7.1	Number of Candidates for each $x_E(D * l)$ bins <i>before</i> efficiency correction.	94
7.2	Number of Candidates for each $x_E(D * l)$ bins <i>after</i> efficiency correction.	95
7.3	The results from fitting the Monte Carlo simulated $x_E(D * l)$ spectrum to that of the data after correcting for the small systematic shift described in Section 7.3.	100
7.4	Change in the $\langle x_E \rangle_{B^0}$ and the Peterson parameter ϵ_b from various source for systematic error study.	101
7.5	Change in the $\langle x_E \rangle_{B^0}$ and the Peterson parameter ϵ_b from various source for systematic error study.	102

8.1 Published fragmentation measurements. 109

8.2 The results for the $\langle x_E \rangle_{B^0}$ and ϵ_b measurement for the D^*e ,
the $D^*\mu$ and the combined samples using the corrected B^0 energy. 110

8.3 The results from fitting the Monte Carlo simulated $x_E(D^*l)$ spec-
trum to that of the data after correcting for the small systematic
shift described in Section 7.3. 110

9.1 The final results for the $\langle x_E \rangle_{B^0}$ and ϵ_b measurement presented
in this analysis. The results with superscript **1** are obtained us-
ing the corrected B^0 energy. The results with superscript **2** are
obtained using the $x_E(D^*l)$ spectrum. 113

2.2 Specific ionization measurements (dE/dx) for various particle species. 21

3.1 Schematic overview of the space-time distribution for the various
stages of jet development 29

3.2 Schematic picture for the Colour String Model 30

3.3 The scaled momentum ($z = E_{hadron}/E_{quark}$) distribution of kaons
and pions. The spectrum characterizes a soft distribution for the
fragmentation of light quarks, meaning that it peaks at low values
of z 31

3.4 The Peterson Function for Heavy Quarks 34

List of Figures

3.5	Mean Value of $\langle z \rangle$ as a function of z_0	35
3.6	Comparison of $\langle z \rangle$ and $\langle z_0 \rangle$ as a function of z_0 in the Lund Model; plot b) is the ratio of $\langle z \rangle$ to $\langle z_0 \rangle$ as a function of z_0	37
<hr/>		
1.1	Feynman diagram for the semileptonic decay of $\bar{B}^0 \rightarrow D^* l \bar{\nu}$	10
1.2	Feynman diagram for the strong decay $D^* \rightarrow D^0 \pi$	11
1.3	Feynman diagram for the decay $D^0 \rightarrow K^- \pi^+$	11
2.1	The Overview of the OPAL Detector	17
2.2	Specific ionization measurements (dE/dx) for various particle species.	21
3.1	Schematic overview of the space-time distribution for the various stages of jet development	29
3.2	Schematic picture for the Colour String Model	30
3.3	The scaled momentum ($z = E_{hadron}/E_{quark}$) distribution of kaons and pions. The spectrum characterizes a <i>soft</i> distribution for the fragmentation of light quarks, meaning that it peaks at low values of z	31
3.4	The Peterson Function for Heavy Quarks	34
5.1	$z_0(B^0)$ plot for the background events (Monte Carlo)	62

3.5	Mean Value of $\langle z \rangle$ as a function of ϵ_b	35
3.6	Plot a) shows the comparison of $\langle z \rangle$ and $\langle x_E \rangle$ as a function of ϵ_b in the Lund Model; plot b) is the ratio of $\langle z \rangle$ to $\langle x_E \rangle$ as a function of ϵ_b	37
3.7	The mean value of x_E as a function of ϵ_b	38
4.1	The momentum distributions of π from D^* decay (solid line) and from D^0 decay (dotted line).	42
4.2	$x(D^*)$ distribution. D^* 's from B decay are shown by the solid line; the dotted line represents the D^* 's from c directly. An b -enriched sample is obtained in the $x(D^*) < 0.5$ region.	48
4.3	Lepton Momentum study (JETSET level); a) the momentum spectrum of the lepton; b) the transverse momentum of the lepton with respect to the jet axis. Leptons are from b and u, d, s or c quarks, respectively. The selection criteria for leptons used are indicated on the plot.	49
4.4	D^* background study (JETSET level). Shown are the distribution of the invariant mass of D^*l when D^* are from: $D^{*0} \rightarrow D^* + \pi^-$ (broken line); $\bar{B}^0 \rightarrow D^{*+}D_x X$ (solid line); B^0 decay (dotted line). The arrow shows the requirement of invariant mass $M(D^*l) > 3 \text{ GeV}/c^2$ for the selection.	50
5.1	$x_E(B^0)$ plot for the background events (Monte Carlo)	62

5.2	ΔM for events with a high p and p_t lepton in the same hemisphere (1990+1991+1992 data from OPAL); a) right-sign combination for signal; b) wrong-sign combination for the background	70
	each of the Monte Carlo with specific q	103
5.3	Correction for the missing energy; the effect of the correction as a function of $M(D^*l)$. a) $E_b^{D^*l}/E_b^{MCtree}$; b) E_b^{corr}/E_b^{MCtree} , where $E_b^{corr} = E_b^{D^*l}m_{B^0}/m_{D^*l}$	71
	The histograms show the shape of the distributions simulated by	
5.4	Correction for the missing energy; the effect of the correction as a function of E_b^{MCtree} . a) $E_b^{D^*l}/E_b^{MCtree}$. b) E_b^{corr}/E_b^{MCtree} , where $E_b^{corr} = E_b^{D^*l}m_{B^0}/m_{D^*l}$	72
6.1	The ΔM plots for each $x_E(B^0)$ ($D^*\mu$). Each plot represents the fitting function for the D^*l signal in different bins of $x_E(B^0)$. The N on each plot shows the number of B^0 candidates, as well as its error, in that particular bin obtained from the fit.	75
	reconstructed to estimate the energy of the B^0 meson. The statis-	
6.2	The ΔM plots for each $x_E(B^0)$ (D^*e). Each plot represents the fitting function for the D^*l signal in different bins of $x_E(B^0)$. The N on each plot shows the number of B^0 candidates, as well as its error, in that particular bin obtained from the fit.	76
	from the previous OPAL measurement.	111
6.3	The $x_E(B^0)$ spectrum for $D^*\mu$	79
6.4	The $x_E(B^0)$ spectrum for D^*e	80
6.5	The $x_E(B^0)$ spectrum obtained using the D^*e and $D^*\mu$ combined samples.	85

- 7.1 The calculated χ^2 with respect to the Peterson parameter ϵ_b . Each value of χ^2 is obtained from fitting the $x_E(D^*l)$ spectrum ($D^*\mu, D^*e$ and combined $D^*l(l = e, \mu)$ samples), for the data and each of the Monte Carlo with specific ϵ_b^i 103
- 7.2 The $x_E(D^*l)$ distributions for $D^*\mu, D^*e$ and $D^*l(l = e, \mu)$ samples respectively. The dots show the measurements from data. The histograms show the shape of the distributions simulated by Monte Carlo with ϵ_b being ϵ_b^- (dotted line), ϵ_b^{min} (dash line) and ϵ_b^+ (dash-dot line), where $\epsilon_b^-, \epsilon_b^{min}, \epsilon_b^+$ are obtained by the fit described in the text. 104
- 8.1 The comparison of various LEP measurements of the fragmentation of b-quarks, $\langle x_E \rangle_b$, to the $\langle x_E \rangle_{B^0}$ obtained by this analysis. All the previous results at LEP use solely leptons from b-hadron decays while in this analysis, the D^*l system has been reconstructed to estimate the energy of the B^0 meson. The statistical errors are shown with solid lines, while dotted lines represent systematic uncertainties. The solid vertical line shows the result from the previous OPAL measurement. 111

Force	Range (m)	Mediators
Electromagnetic	∞	photon
Weak	10^{-16}	W^+, W^-, Z^0
Strong	$\leq 10^{-16}$	8 gluons

Chapter 1

Introduction

The fragmentation of heavy quarks into heavy hadrons is of both theoretical and experimental interest. Many experiments have been done on this topic using a variety of methods. The main purpose of this thesis is to study the fragmentation of the b-quarks. The Peterson fragmentation function which attempts to depict the features of the b-quark fragmentation is discussed. The measurement is performed through the reconstruction of B^0 mesons from the Z^0 decay.

This Chapter is a short introduction to the Standard Model. The Standard Model is also the framework of the theory of Quantum Chromodynamics (QCD) which describes the forces and interactions between particles within 10^{-15} m in distance, where the fragmentation occurs. The data used in this analysis were taken using the OPAL detector at LEP. Chapter 2 is a brief description of the OPAL detector and some of the main techniques for particle identification. Chapter 3 is a brief theoretical and experimental overview of the fragmentation functions and the models which describe them. Chapter 4 follows with a discussion of the Monte Carlo study on the kinematics for the specific decay channel used in this analysis. Chapter 5 through Chapter 7 are the main parts of the analysis with a detailed description of the event reconstruction, the b fragmentation measurement, and the systematic error study. Chapter 8 and

<i>Force</i>	<i>Range (m)</i>	<i>Mediators</i>
Electromagnetic	∞	photon
Weak	10^{-18}	W^+, W^-, Z^0
Strong	$\leq 10^{-15}$	8 gluons

Table 1.1: The Fundamental Forces in Nature. (The gravitational force is not included)

9 contain the discussion and conclusion.

1.1 Standard Model

1.1.2 Particles in the Standard Model

There are many excellent reviews of the Standard Model, see for example in reference [1]. In this chapter, only a brief summary of the Standard Model will be presented.

1.1.1 Fundamental Forces

There are four fundamental forces in nature: *strong*, *electromagnetic*, *weak*, and *gravitational*. Listed in Table 1.1 is a brief summary of the interaction range and the mediator exchanged in the interaction for various forces.

The electromagnetic interaction is characterized by emitting or exchanging photons which couple to the electrical charge of the interacting particle; the

weak force occurs by exchanging an intermediate boson (W^\pm or Z^0). This force only becomes important within the range of 10^{-18} m. The first theory of the weak force was presented by Fermi [2] in 1933, later refined by Lee and Yang, Feynman and Gell-Mann [3], and many others in the late 1950's, and put into its present Standard Model framework by Glashow, Weinberg and Salam in the 1960's [4][5][6][7]. It is often referred as the GWS theory in which the weak and electrodynamic interactions are different manifestations of a single *electroweak* force. The theory describing the strong force is QCD and is discussed in further detail in Section 1.1.3.

1.1.2 Particles in the Standard Model

The Standard Model assumes that the basic particles in nature are fermions and gauge bosons. The fundamental fermions are pointlike and structureless, with half-integer spin. The fermions can be subdivided into the categories of quarks and leptons, which interact with each other by exchanging gauge bosons. Bosons have integer spin. Two quarks interact with each other via the strong force by exchanging a gauge boson called the *gluon*. They interact via the electro-magnetic force by exchanging photons and they may interact weakly via Z^0 or W boson exchange as mentioned above.

There are six quarks, six leptons and eight gluons in the Standard Model. Free quarks do not exist in the Standard Model and they have not been directly

observed by experiment so far. Quarks are always bound together by the strong force to form a composite object called a *hadron*. A hadron composed of a quark and an anti-quark is called a *meson* and a hadron with three quarks or three anti-quarks is called a *baryon* or *anti-baryon*. The quarks carry colour, a quantum number related to *QCD* which will be discussed further in the next section, but the formed final state, the *hadron*, must be colourless. The above mentioned *meson* and *baryon* are the simplest constructions for a colourless object.

$$\begin{pmatrix} u \\ d \end{pmatrix} \begin{pmatrix} c \\ s \end{pmatrix} \begin{pmatrix} t \\ b \end{pmatrix}$$

$$\begin{pmatrix} e \\ \nu_e \end{pmatrix} \begin{pmatrix} \mu \\ \nu_\mu \end{pmatrix} \begin{pmatrix} \tau \\ \nu_\tau \end{pmatrix}$$

There are six different ‘*flavours*’ of quarks. They are named: up, down, charm, strange, bottom and top, or are referred to as the *u*, *d*, *c*, *s*, *b*, *t*-quark. The *u*, *c*, and *t*¹ quarks have $+\frac{2}{3}$ units of electrical charge *e*. Each such quark is associated with a quark with charge $-\frac{1}{3}e$, called the *d*, *s*, and *b*-quarks respectively; the doublets form the *families*. The particles *e*, *μ*, and *τ* are charged leptons with electrical charge of $-1e$; while the neutrinos ν_e , ν_μ and ν_τ carry no electrical charge. Each charged lepton has an associated neutrino which forms a so-called lepton *family*. The neutrinos are assumed to be massless in

¹The *t*-quark has been predicted by the Standard Model but has not been observed by experiments so far.

Meson	Quark content	Isospin	Mass (MeV/c ²)
$\pi^+(\pi^-)$	$ud, \bar{u}\bar{d}$	1	139.5679 ± 0.0007
π^0	$(u\bar{u} - d\bar{d})/\sqrt{2}$	1	134.9743 ± 0.0008
$K^+(K^-)$	$u\bar{s}, \bar{u}s,$	1/2	493.646 ± 0.009
$K^0(\bar{K}^0)$	$d\bar{s}, \bar{d}s$	1/2	497.676 ± 0.030
$D^+(D^-)$	$c\bar{d}, \bar{c}d$	1/2	1869.3 ± 0.5
$D^0(\bar{D}^0)$	$c\bar{u}, \bar{c}u$	1/2	1864.5 ± 0.5
$B^+(B^-)$	$\bar{b}u, b\bar{u}$	1/2	5278.6 ± 2.0
$B^0(\bar{B}^0)$	$\bar{b}d, b\bar{d}$	1/2	5278.7 ± 2.1

Table 1.2: Some of the lowest-mass mesons constructed from quarks.

the Standard Model which agrees with the experimental measurements so far. There are three lepton *families* in the Standard Model.

Each particle has an antiparticle partner. The antiparticles have the same mass and the same coupling strength to the basic forces as their corresponding particles, but all the internal quantum numbers such as charge, spin, baryon number, are opposite to those of their counterpart particles. If the internal quantum numbers of a particle are all zero, the antiparticle and particle are identical. Such an example is the π^0 . Listed in Table 1.2[8] are some of the lowest-mass mesons constructed from quarks.

1.1.3 QCD

The strong force is responsible for nuclear and quark binding. It becomes the dominant force at an interaction distance less than $10^{-15} m$. This is the region where the fragmentation process occurs. Quantum Chromo-Dynamics is the theory of strong interactions. It is a local gauge theory based on an $SU(3)$ symmetry group. It implies a new quantum number “colour” which has three values generally denoted by red, green, and blue. In the standard theory, colour is carried only by quarks and the eight vector bosons called gluons. Colour is conserved in all the interactions. The strong force is mediated by the exchange of gluons and its coupling constant, α_s , is dependent upon energy and is given by:

$$\alpha_s(Q^2) = \frac{4\pi}{(11 - 2/3N_f)\ln(Q^2/\Lambda^2)}$$

where Λ is a QCD scale parameter which is experimentally determined to be $100 \sim 400 MeV$; Q^2 is the momentum transferred during the interaction; N_f is the number of flavours accessible at energy scale Q^2 (for Z^0 , $N_f = 5$). Due to the Heisenberg uncertainty principle (which relates the knowledge of the measurement of momentum and position of a particle), when the distance between the quarks becomes very small, the energy transferred, Q^2 , gets very large. Therefore in small regions of space-time, quarks and gluons act “asymptotically” free when $Q^2 \rightarrow \infty$. This is because the coupling strength between quarks becomes very small (*i.e.*, $\alpha_s \rightarrow 0$) as $Q^2 \rightarrow \infty$. For decreasing Q^2 however, $\alpha_s(Q^2)$ increases very quickly. This is the basis of colour confinement: no free

coloured objects can exist outside a small space-time region. As a consequence, the well-developed mathematical tool of perturbative calculation is restricted to QCD processes when the energy transferred is very large (high Q^2). At low Q^2 however, the theoretical predictions are difficult since QCD is no longer perturbative. Non-perturbative QCD is being developed but is still far away from an application. Therefore so far, the study of the metamorphosis of partons into hadrons still requires a phenomenological model. Further details of some of these models will be discussed later in Chapter 3, along with the theory on the fragmentation of hadrons.

1.2 Background knowledge for this analysis

The following subsections introduce some background knowledge used for the specific analysis presented in this thesis.

1.2.1 Z^0 Decay

In this analysis, the B^0 meson is used to study the fragmentation properties of the b-quark. The Z^0 is used in this analysis as the production source of B^0 mesons.

The Z^0 is a gauge boson with rest mass $91.183 \pm 0.007 \pm 0.006$ GeV/ c^2 lifetime of $1.63 \pm 0.14_{-0.11}^{+0.10}$ ps [12]. Its spin and parity are given by $I(J^P) = \frac{1}{2}(0^-)$

[8]. It was first observed directly in proton-antiproton collisions in 1983 [9]. The Z^0 can be produced through e^+e^- annihilation and a large enhancement in the cross section is evident when the center of mass energy is equal to the Z^0 mass. Experimentally, this large enhancement yields high rates of the Z^0 production which make it possible to determine the couplings of fermions to the Z^0 . Although about 10% of the Z^0 's decay into lepton pairs, most of them decay into quark pairs which will then form hadrons. The branching ratio for this hadronic decay is [8]:

$$Br(Z^0 \rightarrow q\bar{q}) = (69.80 \pm 0.33)\%$$

This high production rate of quark-antiquark pairs from which mesons and hadrons are formed, provides the practical opportunity to study in detail the properties of quarks.

1.2.2 The B^0 Meson and the Decay Channels Under Study

The b quark was proposed as the fifth quark in 1973 by Kobayashi and Maskawa[7], who introduced a six-quark model with three quark families as a possible explanation for the observed CP violation in K meson decays. The first experimental evidence of the existence of the b quark was established by the discovery of Υ resonance (a $b\bar{b}$ bound state) in 1977 at Fermilab[11].

The $B^0(\bar{b}d, \text{ or } b\bar{d} \text{ for } \bar{B}^0)$ has a mass of $5.2787 \pm 0.0021 \text{ GeV}/c^2$ [8] and a lifetime of $1.63 \pm 0.14_{-0.11}^{+0.10} \text{ ps}$ [12]. Its spin and parity are given by $I(J^P) = \frac{1}{2}(0^-)$

[8]. Since the lifetime of the B^0 is very short, it can only be detected by its decay products.

In this analysis, a specific B^0 decay channel is chosen to study the fragmentation of the b-quark. The advantages of choosing this particular decay channel will be discussed later in Chapter 4. The decays that were studied (charge conjugation implied) are:

$$\bar{B}^0 \rightarrow D^{*+} l^- \bar{\nu}_l$$

$$D^{*+} \rightarrow D^0 \pi^+$$

$$D^0 \rightarrow \pi^+ K^-$$

D^{*+} mesons consist of a c quark and \bar{d} quark in an excited (spin 1) state with mass $2010.1 \pm 0.6 \text{ MeV}/c^2$ [8]. In the e^+e^- annihilations the D^{*+} mesons can be produced from the weak decay of B mesons, as shown in the *Feynman diagram* in Figure 1.1. The Feynman diagram is a useful method to describe the interactions between the particles with lines representing the incoming and outgoing particles and the intermediate exchanged particles. The arrows on the quarks and leptons represent the direction, or time evolution of the interaction. The branching ratio for this decay mode is $Br(\bar{B}^0 \rightarrow D^{*+} l^- \bar{\nu}) = (4.9 \pm 0.8)\%$ [8].

The D^* decays via the strong force which conserves hadronic flavour, with

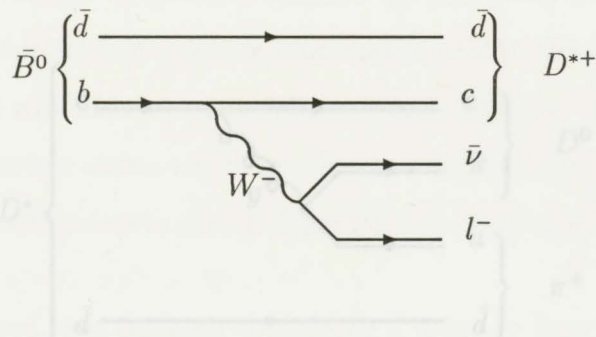


Figure 1.1: Feynman diagram for the semileptonic decay of $\bar{B}^0 \rightarrow D^{*+} l^- \bar{\nu}$.

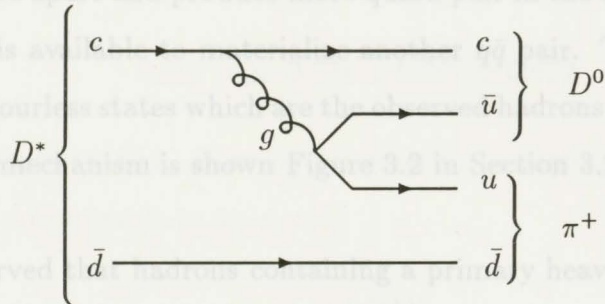
a decay branching ratio of $Br(D^* \rightarrow D^0 \pi) = (55 \pm 4)\%$ [8]. This decay is shown in the Feynman diagram in Figure 1.2.

The D^0 decays weakly through W emission into a kaon and a pion as shown in Figure 1.3. The branching ratio for this decay is measured to be $Br(D^0 \rightarrow K \pi) = (3.65 \pm 0.21)\%$ [8].

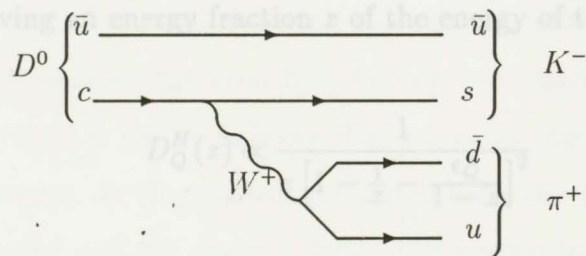
1.2.3 b-quark Fragmentation

Fragmentation is a process by which a $q\bar{q}$ pair evolves into a system of colourless hadrons. It is dominated by nonperturbative processes. A pictorial description

of the fragmentation process is that the colour force between the two quarks increases as the distance between the two quarks increases, similar to the tension of a stretched rubber band. The string will break when the energy stored in the string is high enough to produce another $q\bar{q}$ pair from the vacuum. These $q\bar{q}$ pairs also move apart and produce more quark pair in the same manner until no more energy is available to produce another pair. The produced quarks group into colourless states which are the hadrons. A schematic picture of this string fragmentation is shown in Figure 3.2 in Section 3.2.



It is observed that hadrons containing a primary heavy quark should carry more of the initial quark energy, on average, than a light quark. This tendency for the heavy quark to carry away a large fraction of energy from the initial quark is termed as "hard fragmentation". There are several empirical models which attempt to describe the heavy quark fragmentation. The Peterson fragmentation function [13] model, so far the most widely accepted, is used in this analysis to study the fragmentation of the b quarks. This model predicts the probability of a hadron H having energy fraction z of the energy of the initial quark Q as:



with c_0 being the only free parameter in this expression. Since the energy of the quark is unmeasurable, this property is determined experimentally by $\langle z_H \rangle$ which is defined as the energy of the hadron divided by the beam energy. More details are given in Section 3.2.

Figure 1.3: Feynman diagram for the decay $D^0 \rightarrow K^- \pi^+$.

of the fragmentation process is that the colour force between the two quarks increases as the distance between the two quarks increases, similar to the tension of a stretched rubber band. The string will break when the energy stored in the string is high enough to produce another $q\bar{q}$ pair from the vacuum. These $q\bar{q}$ pairs also move apart and produce more quark pair in the same manner until no more energy is available to materialize another $q\bar{q}$ pair. The produced quarks group into colourless states which are the observed hadrons. A schematic picture of this string mechanism is shown Figure 3.2 in Section 3.2.

It is observed that hadrons containing a primary heavy quark should carry more of the initial quark energy, on average, than a light quark. This tendency for the B meson to carry away a large fraction of energy from the initial quark is termed as “hard fragmentation”. There are several empirical models which attempt to describe the heavy quark fragmentation. The Peterson fragmentation function[13] model, so far the most widely accepted, is used in this analysis to study the fragmentation of the b quarks. This model predicts the probability of a hadron H having an energy fraction z of the energy of the initial quark Q as:

$$D_Q^H(z) \propto \frac{1}{z \left[1 - \frac{1}{z} - \frac{\epsilon_Q}{1-z} \right]^2}$$

with ϵ_Q being the only free parameter in this expression. Since the energy of the quark is unmeasurable, this property is determined experimentally by $\langle x_E \rangle$ which is defined as the energy of the hadron divided by the beam energy. More details about this Peterson fragmentation function will be discussed in

Chapter 3.

The fragmentation functions for both b and c-quarks have been measured at LEP, using only muons from b-hadron decay. OPAL has measured the $\langle x_E \rangle$ of the b-quarks to be [14] :

$$\langle x_E \rangle_b^\mu = 0.726 \pm 0.007 \pm 0.022$$

The error is conservative, allowing for possible modeling uncertainties. This measurement corresponds to an ϵ_b of

$$\epsilon_b = 0.0035$$

Using leptons from b-hadron decay to extrapolate from the lepton's energy to the total energy of the B hadrons is not the only way to investigate the fragmentation of b quarks. Ideally, one would like to entirely reconstruct the B meson. This can be done, for example, through the decay channel $B^0 \rightarrow D^- \pi^+$. However, very few B^0 mesons decaying through this channel have been reconstructed at LEP because the branching ratio is too small ($(3.2 \pm 0.7) \times 10^{-3}$). The branching ratio is the probability that a specific process of decay or interaction would occur. In the analysis presented here, the D^* and the lepton are both reconstructed and the energy of the D^*l system is used to estimate the energy of the B^0 . Only the neutrino remains unmeasured. Therefore, it is possible to better reconstruct the B energy and to study the b-quark fragmentation function in a more direct way than with the inclusive lepton spectrum.

Using the hadronic Z^0 decays collected between 1990 and 1992 at LEP with the OPAL detector, an analysis of partially reconstructed B^0 decays into a D^* meson together with an identified lepton is presented in this analysis.

The OPAL Detector

The data used in this analysis was taken by the OPAL detector. A great deal of information was collected by the detector, used for particle identification of various species and for event reconstruction.

OPAL (Omni Purpose Apparatus at LEP) is one of the four large detectors built for the e^+e^- storage ring LEP at CERN. Its purpose is to detect all types of interactions occurring in e^+e^- collisions at a center of mass energy of about 90 GeV and to achieve efficient and accurate reconstruction and classification of events. A full description of the detector can be found in reference [15] and an overview of the OPAL detector is shown in Figure 2.1. The whole detector is maintained in a magnetic field of 0.435 Tesla.

The OPAL coordinate system is defined as follows:

- the origin of the coordinate system is at the nominal interaction point at the center of the detector[16];

Chapter 2

The OPAL Detector

The data used in this analysis was taken by the OPAL detector. A great deal of information was collected by the detector, used for particle identification of various species and for event reconstruction.

OPAL (Omni Purpose Apparatus at LEP) is one of the four large detectors built for the e^+e^- storage ring LEP at CERN. Its purpose is to detect all types of interactions occurring in e^+e^- collisions at a center of mass energy of about 90 GeV and to achieve efficient and accurate reconstruction and classification of events. A full description of the detector can be found in reference [15] and an overview of the OPAL detector is shown in Figure 2.1. The whole detector is maintained in a magnetic field of 0.435 Tesla.

The OPAL coordinate system is defined as follows:

- the origin of the coordinate system is at the nominal interaction point at the center of the detector[16];

- z axis : along the e^- beam direction;
- x axis : horizontal and directed towards the center of the LEP ring;
- y axis : perpendicular to x, z axis;
- ϕ is measured from the x around z (azimuthal angle)
- θ is measured from z axis (polar angle)

The z -axis is inclined by 1.39% with respect to the horizontal. It follows that the y -axis will have a similar inclination with respect to vertical.

2.1 The Central Tracking System

The central tracking system consists of a silicon microvertex detector and three drift chamber devices, the vertex chamber, the jet chamber and the Z -chamber, inside a solenoidal magnet.

The Silicon Microvertex detector (SI) consists of two barrels of silicon microstrip detectors at radii 6 and 7.5 *cm*. There are 11 ladders in the inner layer and 14 in the outer layer. Each ladder is 18 *cm* long and consists of 3 detectors chained together. Its purpose is to provide a precise measurement for the vertex of the tracks and to improve the resolution for the measurement of momentum as compared to the measurement obtained with the drift chamber alone.

The Central Vertex chamber (CV) is a high resolution cylindrical jet-type drift chamber which is close to the interaction point. The drift time to the axially placed sense wires can be measured precisely so that the $r - \phi$ position of a track can be calculated. The time difference between signals at either end of the sense wire gives a fast but relatively coarse z coordinate measurement which is used by the OPAL track triggering and in pattern recognition [16]. The vertex chamber has 'stereo' layers, which are tilted at a small angle with respect to the axial layers. These stereo layers provide a measurement of position in the z direction.

The Central Jet chamber (CJ) is a large drift chamber with an inner radius of 25 cm, an outer radius of 185 cm and is divided into 24 sectors in ϕ . Each sector in ϕ can provide up to 159 signal hits digitizations along the radial direction of a track. The jet chamber provides at least 20 points per track from these 159 signal wires which cover 95% of the solid angle. Similar to the vertex chamber, a measurement of the drift time determines the coordinates of wire hits of a track in the $r - \phi$ plane. The ionization energy loss of the charged particles, known as dE/dx , is calculated from summing the charges received at each end of a wire and allows identification of particles for certain momentum values. This dE/dx measurement will be discussed in detail again later in this section. The z coordinate of a track in CJ is measured using the charge division technique. At polar angles of $|\cos\theta| > 0.73$, the z coordinate of a track is measured by its exit point in the chamber. This endpoint is determined from the last $r - \phi$ hit on a track using the known z position of the hit wire. A track with its z measured

this way is said to have a “CJ endpoint” measurement.

The drift chambers designed to measure precisely the z coordinate of a track are called CZ chambers. They have an overall resolution of 100-350 μm for the range $44^\circ \leq \theta \leq 136^\circ$.

2.1.1 The dE/dx Measurement

The Central Jet chamber (CJ) measures the energy loss of ionization per As a charged particle traverses a medium, it loses energy through ionization of the medium. The mean rate of energy loss $(dE/dx)^1$ is given by the Bethe-Bloch equation: [17]

$$-\frac{dE}{dx} = 4\pi N_A r_e^2 m_e c^2 z^2 \frac{Z}{A\beta^2} \left[\ln \left(\frac{2m_e c^2 \gamma^2 \beta^2}{I} - \beta^2 - \frac{\delta}{2} \right) \right]$$

with

- N_A : Avagadro's number
- A : atomic weight of the medium
- z : charge of the incident particle (units of e)
- Z : atomic number of the medium
- m_e : electron mass

¹The dx is measured in mass per unit area, *e.g.*, in $g\text{ cm}^{-2}$.

- r_e : radius of electron = 2.817×10^{-13} cm
- I : mean ionization potential of the medium ($\sim 16Z^{0.9}$ eV for $Z > 1$)
- δ : density correction
- β : v/c , the velocity of the charged particle in units of the speed of light
- γ : $1/\sqrt{1 - \beta^2}$

The Central Jet chamber (CJ) measures the energy loss of ionization per unit length (dE/dx) of a particle when it travels across the chamber gas. The central detector is contained in a pressure vessel that maintains a pressure of 4 bar. It has been optimized to provide the best resolution for particle separation.

The charge deposited on the wire is proportional to the energy loss of the particle. When a particle travels through the OPAL jet chamber, the N_{sample} (up to 159) independent energy loss measurements will be distributed in a Landau distribution. The mean energy loss measurement could be extracted by comparing our distribution of N measurements to a Landau distribution. The resolution of dE/dx for the OPAL jet chamber has been determined to be [18]:

$$\frac{\sigma(dE/dx)}{(dE/dx)} = \sigma_{159} \left(\frac{159}{N_{sample}} \right)^{0.43} \quad (2.1)$$

where σ_{159} is the resolution obtained when all the 159 dE/dx samples (N_{sample}) are used in the energy loss measurements. Figure 2.2 shows the dependence of

specific ionization measurement (dE/dx) on the momentum for various particle species. As one can see, at low momentum range, e, μ, π , and K may be easily distinguished. However, the difference in dE/dx is not significant enough, relative to the error on the dE/dx measurement, to distinguish different species at higher momentum range.

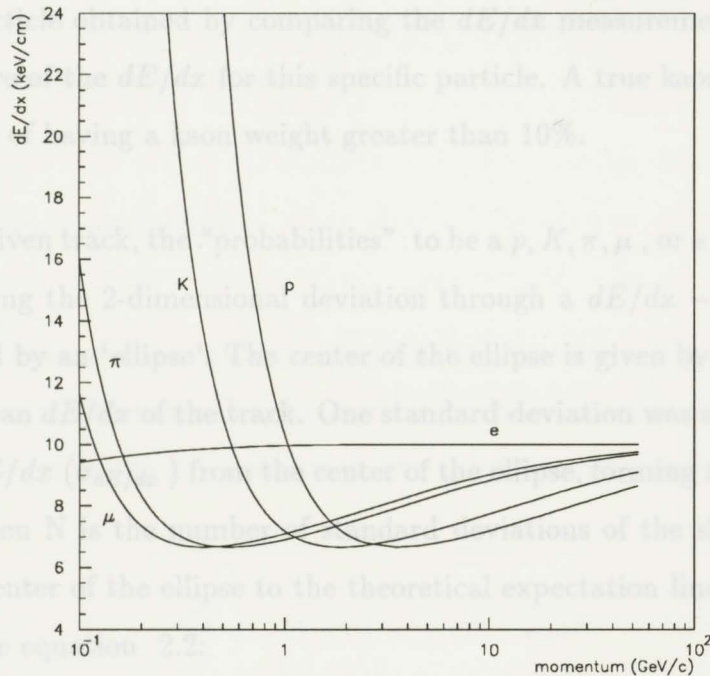


Figure 2.2: Specific ionization measurements (dE/dx) for various particle species.

In the reconstruction of the B^0 through its D^*l decay, the final detectable decay products are 2 pions, a lepton and a kaon. The dE/dx measurement is

important in the identification of the leptons and kaons. A dE/dx weight is used for identifying kaons. A given measurement of the track is away from the expected value for a kaon.

2.1.2 The dE/dx Weight

The dE/dx weight is the probability for a measured track to be identified as a specific particle obtained by comparing the dE/dx measurements to the theoretical curve of the dE/dx for this specific particle. A true kaon track has 90% probability of having a kaon weight greater than 10%.

For a given track, the "probabilities" to be a p, K, π, μ , or e can be obtained by measuring the 2-dimensional deviation through a $dE/dx - p$ plot which is represented by an 'ellipse'. The center of the ellipse is given by the momentum and the mean dE/dx of the track. One standard deviation was assigned to the p (σ_p) and dE/dx ($\sigma_{dE/dx}$) from the center of the ellipse, forming the 2 axes of the ellipse. Then N is the number of standard deviations of the shortest distance from the center of the ellipse to the theoretical expectation line. N is obtained through the equation 2.2:

$$\delta = N \times \sqrt{\sigma_p^2 + \sigma_{dE/dx}^2} = N \times \sigma_{total} \quad (2.2)$$

in which δ is the distance of closest approach from the center of the ellipse to the theoretical curve of a chosen particle species. σ_{total} is the square-root deviation

of the $dE/dx-p$ measurement. Taking a kaon for example, N describes how far, in standard deviations, the given measurement of the track is away from the expected value for a kaon.

Assuming a Gaussian distribution for N , the confidence level for a track to be identified as a kaon is calculated according to N . This confidence level is termed the dE/dx weight. In this analysis, a track for a kaon candidate must have a dE/dx weight greater than 10%, which corresponds to less than $1.64\sigma_{total}$ away from the theoretical expectation.

2.1.3 Track Resolution

The momentum of the particle is obtained by measuring the curvature of the particle track in the magnetic field. For the jet chamber with a spatial resolution of $\sigma_{xy} = 135\mu m$ in the $x - y$ direction, the momentum resolution is given by:

$$\frac{\sigma_p}{p} = \sqrt{0.0004 + (0.0015 * p)^2} \quad (2.3)$$

where the momentum p is in GeV/c . As one can see, the momentum resolution of a track gets worse at higher momentum. The jet chamber also measures the z coordinate with a resolution of $\sigma_z = 6\text{ cm}$ by comparing the charge deposited at either end of each hit wire. If this data is combined with information obtained from the Z chambers, this resolution is improved to $\sigma_z = 100 - 235\mu m$.

2.2 Electromagnetic Calorimeter

The Electromagnetic Calorimeter at OPAL (ECAL) is outside the pressure vessel of the tracking system. It consists of a pre-shower counter (pre-sampler) and a lead glass calorimeter. The Electromagnetic Calorimeter is designed to detect and measure the energy and position of electrons, positrons and photons.

In dealing with electrons and photons at high energies, it is convenient to measure the thickness of the material in units of the radiation length X_0 , the mean distance over which an electron with high energy loses all but $1/e$ of its energy by bremsstrahlung. It is therefore an appropriate scale length for describing high-energy electromagnetic cascades [8]. The material in front of the calorimeter (*i.e.* the solenoid, central detector and pressure vessel *etc.*) is approximately 2 radiation lengths. This will cause a degradation of energy and spatial resolution because of electromagnetic showering before the lead glass.

The electromagnetic pre-sampler is located before the Electromagnetic Calorimeter and the magnetic coil. It consists of two concentric cylinders of limited streamer tubes with wires parallel to the beam axis and cathode strips oriented at $\pm 45^\circ$ with respect to the wires. It samples the energy of a particle before it passes through the magnetic coil, to enable one to correct for the degradation of energy as the particle goes through the coil. It provides a more precise measurement of the position and energy of showers.

The barrel region of the Electromagnetic Calorimeter covers $|\cos\theta| < 0.82$ and the endcap region covers $|\cos\theta|$ between 0.81 to 0.95.

2.3 Hadron Calorimeter

Outside the Electromagnetic calorimeter is the iron return yoke of the magnet, which is instrumented with streamer tubes with pads and strips to form a hadronic calorimeter(HCAL).

The hadronic calorimeter consists of three parts. The barrel($|\cos\theta| < 0.81$), the endcap ($0.815 < |\cos\theta| < 0.91$), and the pole tip ($0.91 < |\cos\theta| < 0.99$).

Hadronic energy is measured by combining the signals of the Electromagnetic Calorimeter and hadronic calorimeter since hadronic showers begin in the Electromagnetic part of the Calorimeter. The energy resolution of the hadronic calorimeter is $120\%/\sqrt{E}$, where E is in GeV .

2.4 Muon Chambers

Outside the hadronic calorimeter are the muon chambers, which are constructed of 4 layers of drift chambers, and which identify muons by range (most charged particles should have been stopped by the calorimeters before reaching the muon

chambers). The muon chambers are designed to identify muons by measuring the position and direction of all charged particles leaving the hadronic calorimeter. Ninety-three percent of the solid angle is covered by at least one layer of the muon chamber, but still there are gaps in the acceptance due to the beam pipe, the supporting legs and the cables. Each layer is constructed of 110 large-area drift chambers, 1.2 m wide and 90 mm deep. The barrel region covers $|\cos\theta| < 0.68$ for at least four layers; the endcap region covers $0.67 < |\cos\theta| < 0.98$.

The return yoke for the magnetic field in the hadronic calorimeter which has $8 \sim 14$ interaction lengths also serves as a muon filter.

3.1 The Region of Interest for the Fragmentation

The formation of a final state hadron involves small momentum transfer or low Q^2 . Although it is believed that the hadronization procedure is completely

described by *QCD*, the perturbative techniques are not applicable in this energy regime, and the details of this hadronization process are as yet incalculable. Low

zation processes must be described by a phenomenological model.

The goal in studying fragmentation is to determine how the collection of partons,

observable final state hadrons.

The Fragmentation of Heavy Mesons

Figure 3.1 is a schematic view of the space-time distribution for the various

As mentioned in Section 1.1.3, the fragmentation mechanism has not been well understood yet. The theoretical predictions are difficult in this regime since the *QCD* theory is no longer perturbative. The study of the metamorphosis of partons into hadrons still requires a phenomenological model. In this Chapter, the region where the fragmentation takes place is shown. The two main classes of fragmentation models, namely the Independent Jet Model and the Colour String Model both inspired by *QCD* are briefly described. In this Chapter an attempt is made to focus on understanding the features of the b-quark fragmentation as well as the Peterson fragmentation function, a widely used parametrization function for heavy quark fragmentation.

3.2 Fragmentation Models

3.1 The Region of Interest for the Fragmentation

Several models inspired by *QCD* have been widely employed to model the fragmentation and hadronization processes. Here are two frequently used models:

The formation of a final state hadron involves small momentum transfer or low Q^2 . Although it is believed that the hadronization procedure is completely

described by QCD , the perturbative techniques are not applicable in this energy regime, and the details of this hadronization process are as yet incalculable. Low energy hadronization processes must be described by a phenomenological model. The goal in studying fragmentation is to determine how the collection of partons, at large Q^2 and small distance, materializes into observable final state hadrons.

Figure 3.1 is a schematic view of the space-time distribution for the various stages of jet development. Within the innermost region, quarks behave as point-like Dirac particles. This regime is very hard to probe directly with current experimental facilities. Outside this region, hard partons travel about half a fermi ($1 fm = 10^{-15} m$) and form the crystallization points for distinct jets. This region has been well understood by perturbative QCD . In the outermost region, the particles emanate from the interaction point in several bundles forming what are known as *jets*. The region between $10^{-15} \sim 10^{-14} m$ in Figure 3.1 is our region of interest. This is the region where quarks hadronize within a few fermi and begin to fragment. This region is experimentally accessible but has not been very well understood yet.

3.2 Fragmentation Models

Several models inspired by QCD have been widely employed to model the fragmentation and hadronization processes. Here are two frequently used models:

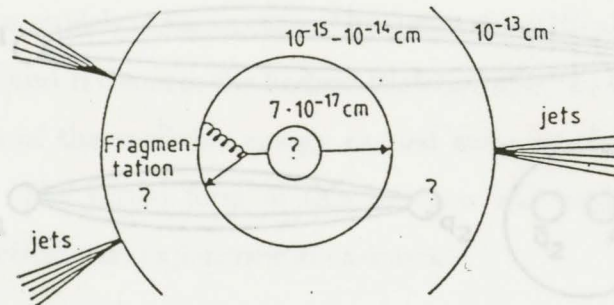


Figure 3.1: Schematic overview of the space-time distribution for the various stages of jet development

1. The basic assumptions in the Colour String Model agree better with the general ideas of QCD and quark & gluon coupling.
- **Independent Jet Model** [19]: Each parton fragments independently of the other partons until all the available energy is used up.
2. The Colour String Model is intrinsically Lorentz invariant and explicitly conserves momentum and flavour at each string breaking.
- **Color String Model** [19] : In the Lund colour string model, a colour singlet string, representing the colour field between the $q\bar{q}$ pair, joins the primary quarks. Gluons are just kinks in the string. As the primary quarks separate, the string tension increases linearly with the separation distance, until it is energetically favorable to create a lighter $q\bar{q}$ pair, breaking the string, thus forming the hadrons. Figure 3.2 is a schematic plot of this string breaking process.

Since the c-quark and b-quark are much heavier than other quarks, they are often produced in pairs. The String Model is in many aspects more favorable compared to the Independent Jet Model. A more detailed explanation can be found in reference [20]. Generally speaking, it is because :

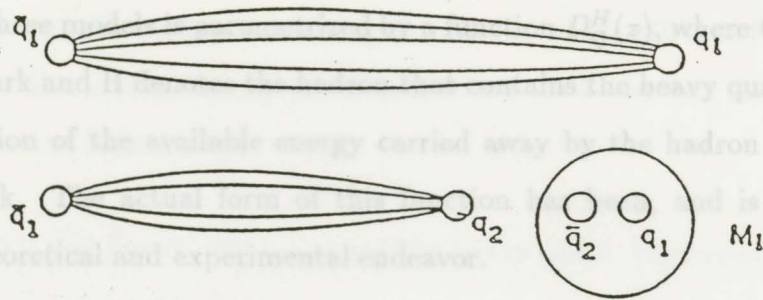


Figure 3.2: Schematic picture for the Colour String Model

1. The basic assumptions in the Colour String Model agree better with the general ideas of QCD and quark & gluon couplings.
2. The Colour String Model is intrinsically Lorentz invariant and explicitly conserves energy, momentum and flavour at each string break.

With our present insight into the Q^2 dependence of the structure of the hadronic events, the merging of the perturbative QCD shower approach with non-perturbative fragmentation schemes as supplied by string algorithms is the most promising way to proceed in this jet development regime [20].

Since the c -quark and b -quark are much heavier than other quarks, they are often referred to as *heavy quarks*, while the u -quark, d -quark and s -quark are referred to as *light quarks*; for the same reason, a meson which contains a heavy quark is often called a *heavy meson*. The fragmentation of heavy quarks into

hadrons is of great theoretical interest. The development of the fragmentation processes in these models is parametrized by a function $D_Q^H(z)$, where Q denotes the heavy quark and H denotes the hadron that contains the heavy quark, while z is the fraction of the available energy carried away by the hadron from the primary quark. The actual form of this function has been, and is still, the subject of theoretical and experimental endeavor.

purely kinematical considerations:

3.3 The Peterson Fragmentation Function

Substituting the fragmentation function $D_Q^H(z)$ for a heavy quark Q and a light quark q (i.e. $Q \rightarrow H(Qq) + q$). The energy transfer ΔE in this process is very small, which is of the order $100 \sim 400$ MeV. ΔE can be expressed as:

$$\Delta E = E_q = \sqrt{m_q^2 + z^2 p_0^2} + \sqrt{m_H^2 + (1-z)^2 p_0^2} - \sqrt{m_Q^2 + p_0^2} \quad (3.1)$$

where p_0 is the momentum of the primary quark Q and z is the momentum fraction carried by the hadron H , namely:

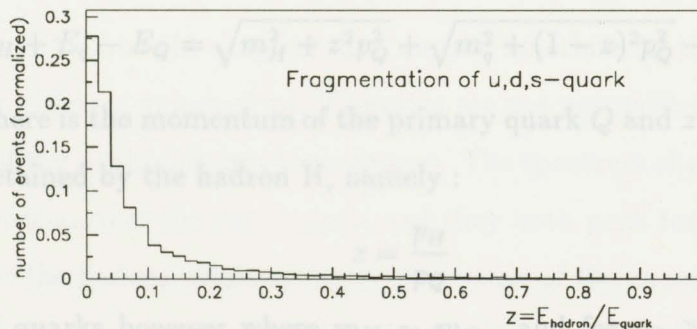


Figure 3.3: The scaled momentum ($z = E_{hadron}/E_{quark}$) distribution of kaons and pions. The spectrum characterizes a *soft* distribution for the fragmentation of light quarks, meaning that it peaks at low values of z .

where

Originally, it was assumed that $D_Q^H(z)$ for the heavy quarks would be similar to that for the light quarks, which fragment principally into many pions and kaons, with a distribution of z which falls steeply as z increases as shown in Figure 3.3. However, kinematic considerations of heavy quark fragmentation

into a hadron suggest that the energy and momentum of the heavy quark is retained by the specific hadron containing this quark, which will lead to a harder fragmentation distribution in z (i.e. the spectrum peak towards the higher z value) than for the light quarks.

Bjorken [21] and Suzuki [22] examined the heavy quark fragmentation using purely kinematical considerations:

Suppose a heavy quark Q fragments into a hadron $H(Q\bar{q})$ and a light quark q (i.e. $Q \rightarrow H(Q\bar{q}) + q$). The energy transfer ΔE in this process is very small, which is of the order $100 \sim 400 \text{ MeV}$. ΔE can be expressed as:

$$\Delta E = E_H + E_q - E_Q = \sqrt{m_H^2 + z^2 p_Q^2} + \sqrt{m_q^2 + (1-z)^2 p_Q^2} - \sqrt{m_Q^2 + p_Q^2} \quad (3.1)$$

where p_Q here is the momentum of the primary quark Q and z is the momentum fraction retained by the hadron H , namely :

$$z = \frac{p_H}{p_Q}$$

For heavy quarks however where $m_H \sim m_Q$, and for $p_Q \gg m_Q$, the Taylor expansion of 3.1 may be written as:

$$\Delta E = 1 - \frac{1}{z} - \frac{\epsilon_Q}{1-z}$$

where

$$\epsilon_Q \equiv \left[\frac{m_q}{m_Q} \right]^2 \quad (3.2)$$

Since the transition amplitude is proportional to $(\Delta E)^{-1}$, and if an extra $1/z$ for phase space (see ref. [20], p214) is included, the energy spectrum of the

hadron H as a function of z is obtained. This spectrum may be written in terms of $D_Q^H(z)$ more explicitly as

$$D_Q^H(z) \propto \frac{1}{z \left[1 - \frac{1}{z} - \frac{\epsilon_Q}{1-z} \right]^2} \quad (3.3)$$

Considering the effective mass of a u-quark as 0.3 GeV , that of the c-quark to be 1.5 GeV and that of the b-quark to be 4.7 GeV , it is expected that $\langle \epsilon_c \rangle = 0.04$ for the c-quark and $\langle \epsilon_b \rangle = 0.004$ for the b-quark according to the definition of ϵ_Q shown in equation 3.2. Equation 3.3 is often referred to as the Peterson fragmentation function [13].

Figure 3.4 shows the shape of the Peterson functions for the b quark and the c quark for different values of ϵ_Q . The plots are not normalized in order that the positions of the peaks appear more obvious. The spectrum shape for the b quark is narrower than that for the c quark, and they both peak towards unity, which means that the hadron retains a large proportion of the energy and momentum of the initial heavy quark. Additionally, the heavier the primary quark is, the greater the average fraction of the energy carried away by the heavy meson. The heavy quark fragmentation is said to be a 'hard' fragmentation. Also, for both of the b and c quarks, there is a tendency for the spectrum to peak towards 1 as the ϵ_Q value decreases. Figure 3.5 shows the relationship of ϵ_Q to the mean value of z from another perspective. The spectrum tends to be 'softer' as the ϵ_Q increases.

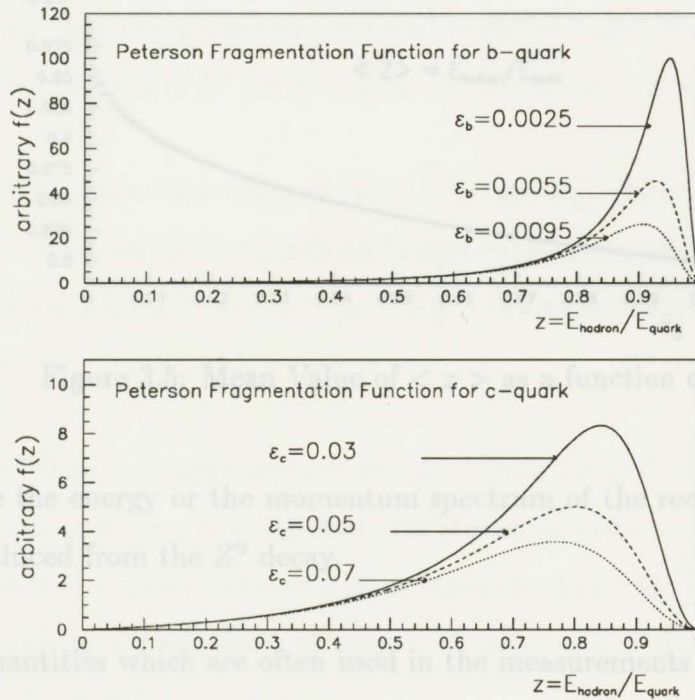


Figure 3.4: The Peterson Function for Heavy Quarks

3.4 Experimental Evaluation of the Heavy Quark Fragmentation Function

They are, in general, different from the fundamental parameter z for the following reasons:

The momentum of the initial quark p_Q must be obtained to measure z , the quantity that depicts the feature of the quark fragmentation. However, p_Q is not a measurable quantity due to the initial gluon radiation at the interaction vertex. The most direct method of measuring the fragmentation function is

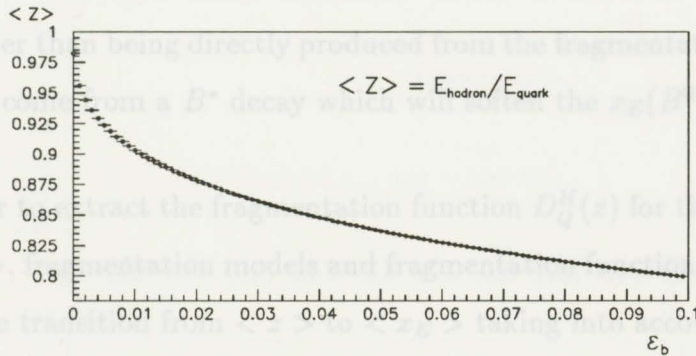


Figure 3.5: Mean Value of $\langle z \rangle$ as a function of ϵ_b

For the Peterson Fragmentation scheme, Figure 3.6 a) shows the relationship to measure the energy or the momentum spectrum of the reconstructed heavy meson produced from the Z^0 decay.

The quantities which are often used in the measurements are

$$x_E = \frac{E_{\text{meson}}}{E_{\text{beam}}}$$

or

$$x_p = \frac{P_{\text{meson}}}{P_{\text{beam}}}$$

They are, in general, different from the fundamental parameter z for the following reasons:

- a) Due to perturbative QCD gluon radiation, the energy available for the quark at the beginning of the fragmentation process may be less than E_{beam} , leading to $x_E \leq z$ as shown in Figure 3.6 a).

b) Initial photon radiation can also lower the quark energy .

c) Rather than being directly produced from the fragmentation of a b quark, the B^0 can come from a B^* decay which will soften the $x_E(B^0)$ spectrum.

In order to extract the fragmentation function $D_Q^H(z)$ for the b quark or the mean $\langle z \rangle$, fragmentation models and fragmentation functions have been used to study the transition from $\langle z \rangle$ to $\langle x_E \rangle$ taking into account the effects of a), b) and c).

For the Peterson Fragmentation scheme, Figure 3.6 a) shows the relationship between $\langle z \rangle$ and $\langle x_E \rangle$ using the Lund Model, as a function of ϵ . The dashed line represents the mean value of z as a function of ϵ_b . The dotted line is the mean value of x_E for the same ϵ_b range. Clearly, $\langle z \rangle$ does not agree with $\langle x_E \rangle$ by about 20%.

Figure 3.6: Plot a) shows the comparison of $\langle z \rangle$ and $\langle x_E \rangle$ as a function

of ϵ_b . Figure 3.6 b) is the ratio of $\langle z \rangle_b$ to $\langle x_E \rangle$ as a function of ϵ_b . As expected, the plots show that $\langle x_E \rangle$ is less than $\langle z \rangle$.

given the mean value of x_E . Then for this given ϵ_b , the variable x , which is more

Figure 3.7 is an expanded plot which again shows the mean value of x_E as a function of ϵ_b . The dots are measured from Monte Carlo generated events with different values of ϵ_b as input for the Peterson fragmentation function. The errors on the dots are statistical. The spectrum is fitted with a third-order polynomial. The fitting results are presented in the plot which shows the four parameters in the polynomial. With this function in hand, ϵ_b can be obtained,

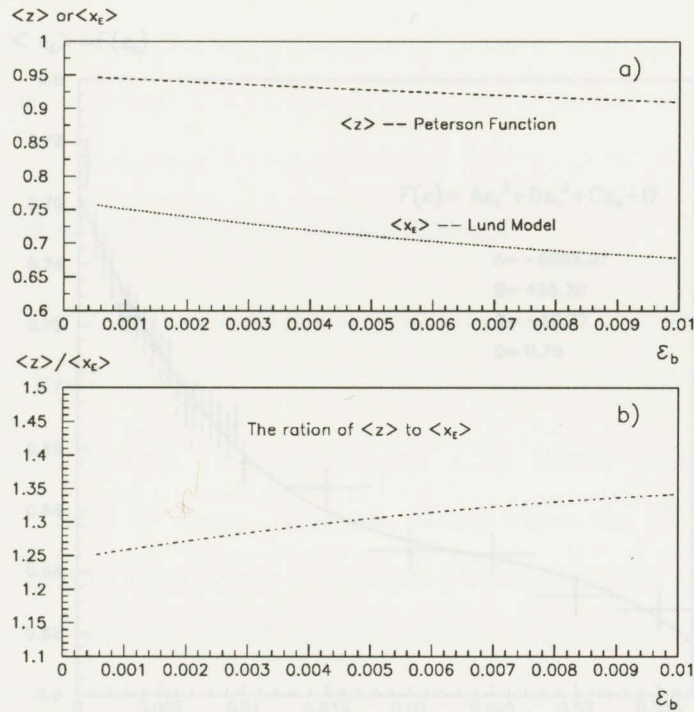


Figure 3.6: Plot a) shows the comparison of $\langle z \rangle$ and $\langle x_E \rangle$ as a function of ϵ_b in the Lund Model; plot b) is the ratio of $\langle z \rangle$ to $\langle x_E \rangle$ as a function of ϵ_b .

in this analysis for reconstructing the B^0 meson.
 given the mean value of x_E . Then for this given ϵ_b , the variable z , which is more fundamental in understanding the fragmentation scheme, can be obtained from Figure 3.5.

In Chapter 6, the measurement of $\langle x_E \rangle$ and ϵ_b for the B^0 meson using the data obtained from the experiment will be described in detail. The next Chapter studies the kinematic feature of the particles in the specific decay channels chosen

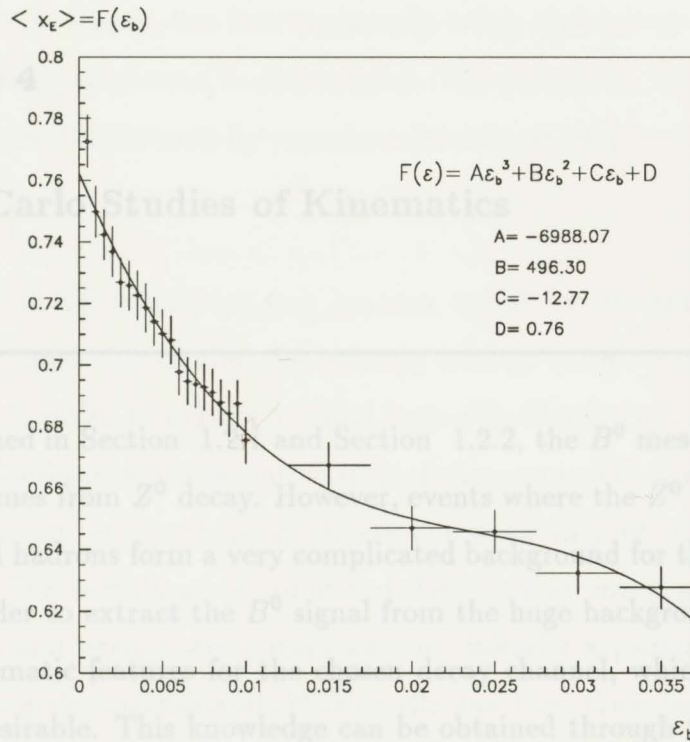


Figure 3.7: The mean value of x_E as a function of ϵ_b

in this analysis for reconstructing the B^0 meson.

4.1 JETSET and GOPAL

The JETSET simulation from the LUND family of event generators is used for the kinematic study in this analysis [23]. The properties of jet fragmentation can be derived from strong interactions based on the Quantum Chromodynamics theory (QCD). JETSET uses phenomenological software models for jet frag-

mentation that generate complete events [23]. In a sense, JETSET is a model based on QCD theory, but it is constantly being updated as new information, parameters, is determined. The parameter values have been either determined and tuned by experimental data at OPAL, or are theoretically

Chapter 4

Monte Carlo Studies of Kinematics

The JETSET simulation can be very useful for designing a detector; it also can be used to examine the existing data in order to extract interesting

As mentioned in Section 1.2.1 and Section 1.2.2, the B^0 meson studied in this analysis comes from Z^0 decay. However, events where the Z^0 decays into other leptons and hadrons form a very complicated background for the B^0 reconstruction. In order to extract the B^0 signal from the huge background, a knowledge of the kinematic features for the chosen decay channel, which distinguish the signal is desirable. This knowledge can be obtained through the studies of the Monte Carlo simulated sample. In this analysis, this sample is generated by the JETSET and GOPAL software package.

4.1 JETSET and GOPAL

The JETSET simulation from the LUND family of event generators is used for the kinematic study in this analysis [23]. The properties of jet fragmentation can be derived from strong interactions based on the Quantum ChromoDynamics theory (QCD). JETSET uses phenomenological software models for jet frag-

mentation that generate complete events [23]. In a sense, JETSET is a model based on QCD theory, but it is constantly being updated as new information, in the form of parameters, is determined. The parameter values have been either determined and tuned by experimental data at OPAL, or are theoretically motivated.

The JETSET simulation can be very useful for designing a detector; it also can be used to examine the existing data in order to extract interesting anomalies. In order to extract a signal from a data sample it is often necessary to make selections on certain attributes of the events which comprise the data sample. In any event, there is always the possibility of misidentification of particles. The usefulness of simulated data is that every particle's identity, momentum and energy, are always known. Initially a parton configuration is selected using electroweak and QCD results and then these partons are allowed to fragment into hadrons which decay further if unstable. The fragmentation is assumed to occur according to rules independent of the primary process. A probabilistic approach is taken to generate the events according to the decay branching ratios. Therefore these will show the same mean behavior as the experimentally observed events. Events of the type $e^+e^- \rightarrow Z^0$ with a center of mass energy of 91.31 GeV were generated using JETSET. The Z^0 's then decay into particles which can be analyzed. No detector reconstruction is done within JETSET.

In GOPAL, another software package written for the OPAL detector,

the full detector response is simulated: as a particle simulated by the Monte Carlo travels through each subdetector, the digitization for that subdetector is simulated and stored so that the simulated data and the real data taken from the experiment have the same format. The standard reconstruction codes for all subdetectors are then run on both the data and the Monte Carlo simulated data. The GOPAL [24] data is used for background and efficiency studies. It is termed here as the Monte Carlo simulation sample.

Conventionally, the data obtained from JETSET is termed a 'four-vector', referring to the energy and momenta (x, y, z component) of all particles. The momentum and energy distributions obtained with JETSET are used to provide a preliminary set of selection criteria to best extract the signal from the background on the basis of purely kinematic considerations. This will be discussed in detail in the following subsections.

4.3 D^* Momentum

4.2 π Momentum

As previously discussed, the D^* can come from the direct coupling of c quarks or b quarks with s . The D^* from primary c quarks are the main source of the background to the D^* from

JETSET one can have a closer look at the kinematic differences for the D^* from various sources, as shown in Figure 4.2.

$$\bar{B}^0 \rightarrow D^{*+} l^- \bar{\nu}_l$$

$$D^{*+} \rightarrow D^0 \pi_1^+$$

$$D^0 \rightarrow \pi_2^+ K^-$$

The D^* from primary c quark production are more energetic than the D^*

where π_1 is used to distinguish the slow pion from the D^* decay from the more energetic π_2 produced in the D^0 decay. Figure 4.1 shows the momentum distribution for the two pions. The distributions are quite distinct.

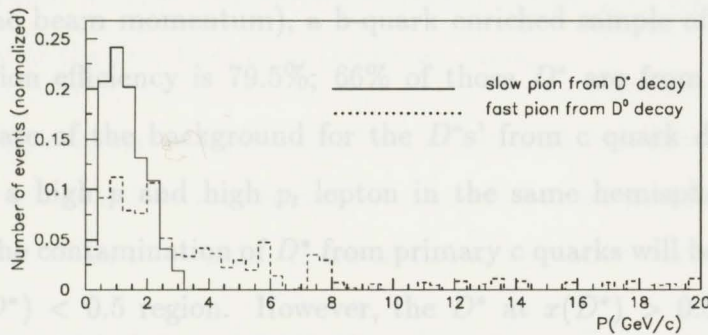


Figure 4.1: The momentum distributions of π from D^* decay (solid line) and from D^0 decay (dotted line).

4.3 D^* Momentum

As previously discussed, the D^* can come from the direct coupling of c quarks or b quarks with Z^0 . The D^* 's from primary c quarks are the main source of the background to the D^* from B^0 decay. Using JETSET one can have a closer look at the kinematic differences for the D^* from various sources, as shown in Figure 4.2.

The D^* from primary c quark production are more energetic than the D^*

from B decays since the latter are the cascade products from B^0 while the former are produced due the direct coupling of the c quark.

In the region where the momentum of the D^* is less than $22 \text{ GeV}/c$ (or equivalently, $x(D^*) < 0.5$ where $x(D^*)$ is defined as the momentum of the D^* over the beam momentum), a b -quark enriched sample of D^* is obtained. The selection efficiency is 79.5%; 66% of those D^* are from B decays. The rejection rate of the background for the D^* 's from c quark direct coupling is 51.9%. If a high p and high p_t lepton in the same hemisphere as the D^* is required, the contamination of D^* from primary c quarks will be largely reduced in the $x(D^*) < 0.5$ region. However, the D^* at $x(D^*) > 0.5$ are not simply rejected otherwise 34% of the D^* 's from B^0 will be thrown away. In the event selection, as it will be described later in Chapter 5, more strict selection criteria are imposed for the $x(D^*) < 0.5$ region to eliminate the D^* 's from c quarks. For the $x(D^*) > 0.5$ region, the requirement of leptons with high momentum and transverse momentum in the same hemisphere as the D^* will ensure that most of the D^* are from B^0 decay.

4.4 Kinematic Studies for Leptons

The channel studied involves the semileptonic decay of the B^0 . In the reconstruction of the B^0 from $D^* l\nu$, the correct identification of leptons from the B^0 decay is crucial. Leptons are a well-established signature of the decay of b -

flavoured and c-flavoured hadrons. They can come from various sources. Listed are three main sources which might affect this analysis.

- Semileptonic decay of a meson hadronized from primary quarks. They are also often referred to as *prompt leptons* because they are produced in the decay of the first hadron in the decay chain;
- Photon conversion from $\gamma \rightarrow e^+e^-$. When a photon passes through material such as a detector component, there is a small probability that it may convert to an e^+e^- pair. These electrons are called *conversion electrons*;
- Dalitz decay of π_0 and η mesons, where $\pi^0 \rightarrow e^+e^-\gamma$, and $\eta \rightarrow e^+e^-\gamma$.

4.5 Some Kinematic Studies of the Background for D^*

The background channels under study are as follows (charge conjugate implied):

The kinematic characteristics of the semileptonic decay of leptons from different kind of quarks are compared in figure 4.3. The quarks are from Z^0 decays from the e^+e^- production. p is the total momentum and p_t is the transverse momentum of the lepton with respect to the jet axis.

2. $B^0 \rightarrow B^{*+} D, X$ (X means anything other than a D meson)

In the first plot of Figure 4.3, it can be seen that electrons from primary b-flavored hadron decays (dotted line) have a harder momentum spectrum than electrons from the other light quarks (solid line) due to the hard b quark fragmentation. For the transverse momentum, the difference is even more drastic. Most of the leptons from u, d, s and c quarks have $p_t < 0.8 \text{ GeV}/c$, leaving mainly leptons from b quarks in the region where $p_t > 0.8 \text{ GeV}/c$. If the $p_t > 0.8 \text{ GeV}/c$

condition is implemented in the selection of the leptons, a clean sample of leptons from b-flavored hadrons can be obtained, with only a tiny contamination of leptons from c-quark decays. In this analysis, a cut of $p > 3 \text{ GeV}/c$ and $p_t > 0.8 \text{ GeV}/c$ is carried out for lepton selection. Since these are the standard selection criteria used in the OPAL $b \rightarrow l$ analysis [25], the background and efficiencies relating to these criteria have been well studied and are well understood. Moreover, this will also enable us to compare our results with the previous measurements of b fragmentation studies obtained using inclusive muons only.

4.5 Some Kinematic Studies of the Background for D^*

The background channels under study are as follows (charge conjugate implied):

1. $B^- \rightarrow D^{*0} l^- \bar{\nu}_l$

where $D^{*0} \rightarrow D^{*+} \pi^-$

2. $\bar{B}^0 \rightarrow D^{*+} D_x X$ (X means anything other than a D meson)

The D^{*0} is a bound state of a charm quark and a light (u,d) quark in its first excited ($l = 1$) p-wave state. A D^* from the D^{*0} decay is considered a source of background since a lepton from the B^- decay and a D^* from the D^{*0} decay can form a fake B^0 signal.

The decays of B^0 to states including a D^* and a D_x (where D_x represents any charmed meson that decays semileptonically, such as D^0, D^+, D_s etc.) are considered background events to the sample of $D^*l\nu$ due to the fact that the D_x might decay semileptonically as well. The D^* can be misassociated with a cascade lepton from D_x , instead of that from the primary decay of the B meson, to form a 'fake' B^0 signal.

Figure 4.4 shows the invariant mass of the D^*l for D^* s which arise from D^{**0} s decay (broken line); for D^* s which are accompanied by another D_x (solid line); and for D^* s from a real B^0 decay (dotted line). It is clearly shown that the D^* s which are accompanied by another D_x have the lowest kinetic energy. The D^*l for D^* from D^{**0} are also slightly lower in energy, on average, than that of the D^* from the $B^0 \rightarrow D^*l\nu$ decay. The invariant mass spectrum of $M(D^*l)$ taken for all the three sources mentioned above is populated in the region below $3 \text{ GeV}/c^2$. By requiring the $M(D^*l)$ for the selected B^0 candidates to be greater than $3 \text{ GeV}/c^2$, 83% of this background will be removed while 86% of the signal (i.e. D^* from B^0 decay) survives the cut.

However, the $M(D^*l)$ spectrum for D^* 's from D^{**} decay is similar to that of the D^* 's from B^0 decay. Thus only 30% of the D^* from this source are eliminated after requiring $M(D^*l) > 3 \text{ GeV}/c^2$. This contamination effect arising from D^{**0} will be considered as a source of systematic error and will be discussed in Chapter 6 and Chapter 7.

The selection criteria discussed above provide a part of the preliminary set of selection criteria for the event selection. Other selection criteria are imposed due to the imperfection of the detector in measuring the position, the energy momentum of the tracks, and due to the much more complicated background which can not be distinguished from the signal as easily as in the Monte Carlo sample. The techniques for the event selection are described in the next Chapter.

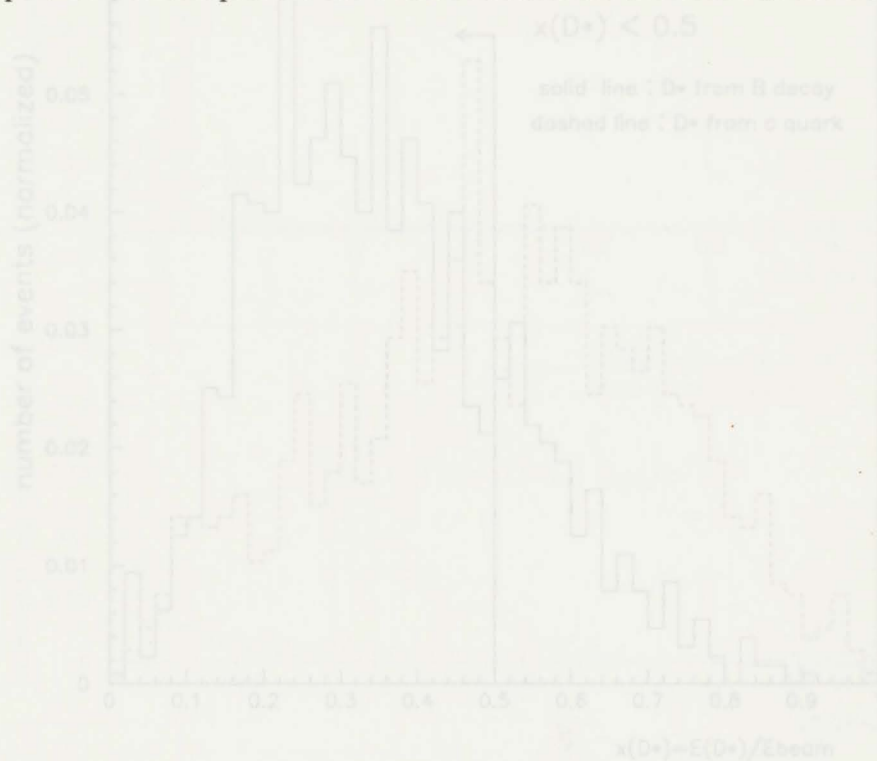


Figure 4.2: $x(D^*)$ distribution. D^* 's from B decay are shown by the solid line; the dotted line represents the D^* 's from c directly. An b -enriched sample is obtained in the $x(D^*) < 0.5$ region.

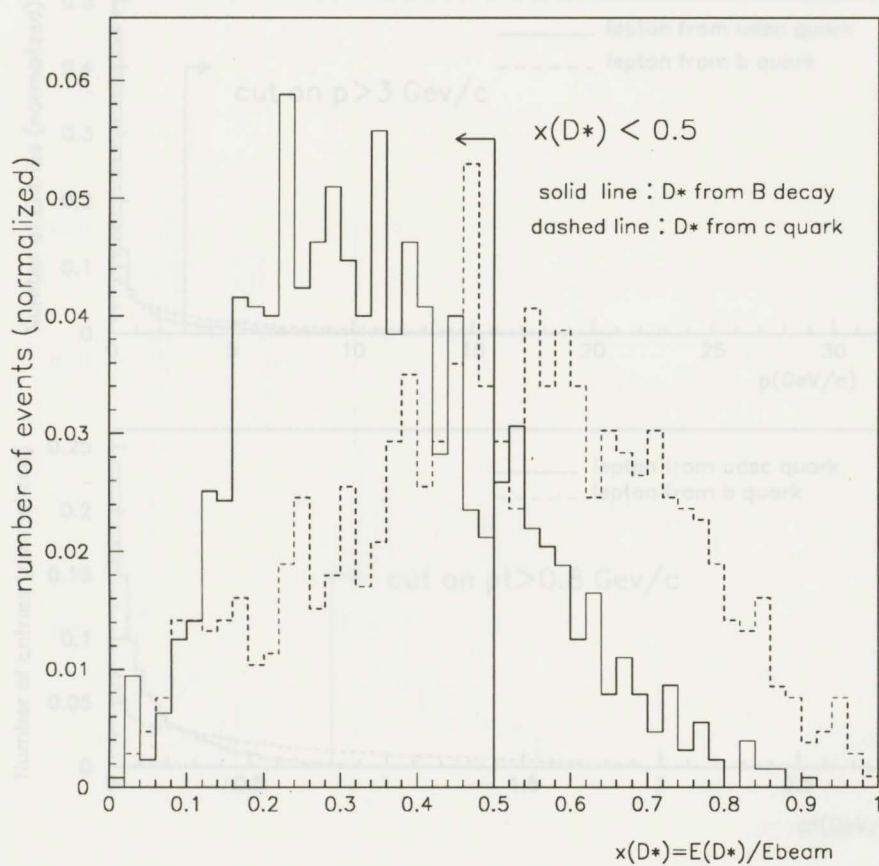


Figure 4.2: $x(D^*)$ distribution. D^* 's from B decay are shown by the solid line; the dotted line represents the D^* 's from c directly. An b -enriched sample is obtained in the $x(D^*) < 0.5$ region.

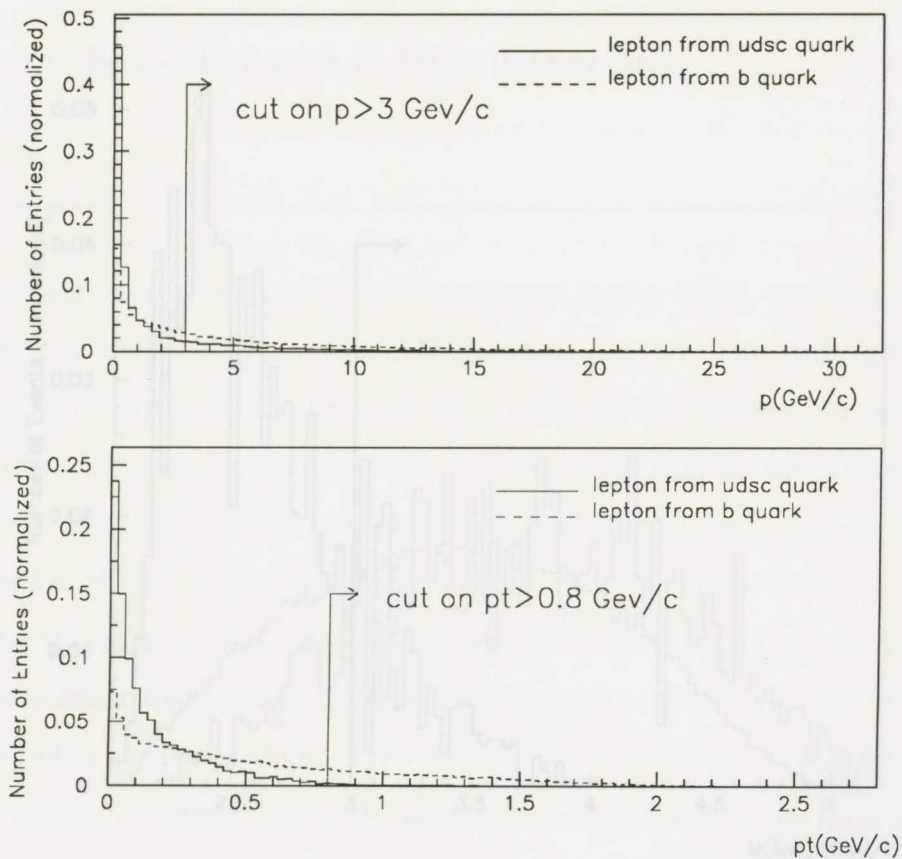


Figure 4.3: Lepton Momentum study (JETSET level); a) the momentum spectrum of the lepton; b) the transverse momentum of the lepton with respect to the jet axis. Leptons are from b and u, d, s or c quarks, respectively. The selection criteria for leptons used are indicated on the plot.

Chapter 5

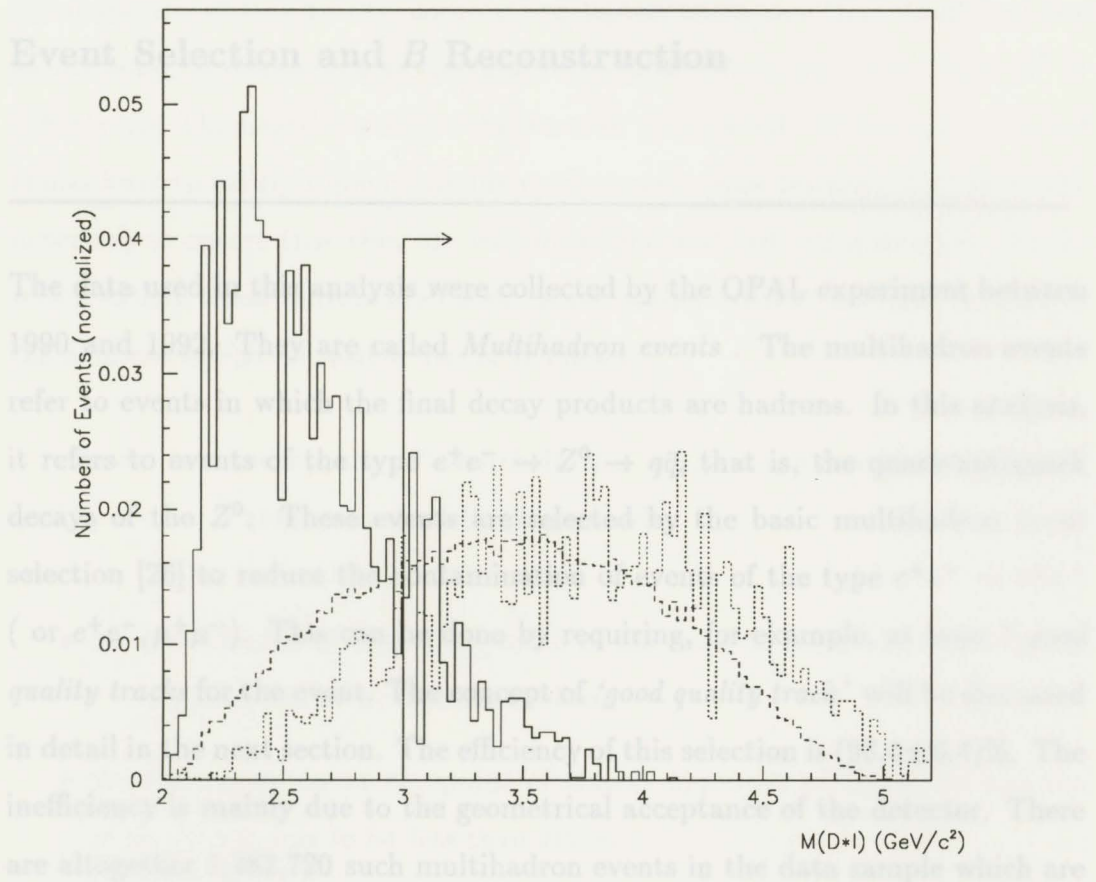
Event Selection and B Reconstruction

Figure 4.4: D^* background study (JETSET level). Shown are the distribution of the invariant mass of D^*l when D^* are from: $D^{**0} \rightarrow D^* + \pi^-$ (broken line); $\bar{B}^0 \rightarrow D^{**+} D_x X$ (solid line); B^0 decay (dotted line). The arrow shows the requirement of invariant mass $M(D^*l) > 3 \text{ GeV}/c^2$ for the selection.

Chapter 5

The reconstruction of the B^0 through the $B^0 \rightarrow D^* l \nu$ decay channel requires the detection of four tracks, namely, one lepton track, one kaon track and two $(K^*s)l\nu$. The neutrino escapes the detector undetected. All the reconstructed tracks have to satisfy some minimum requirements (now standard for the OPAL

detector) to ensure that they are well measured and well reconstructed. Tracks

The data used in this analysis were collected by the OPAL experiment between 1990 and 1992. They are called *Multihadron events*. The multihadron events refer to events in which the final decay products are hadrons. In this analysis, it refers to events of the type $e^+e^- \rightarrow Z^0 \rightarrow q\bar{q}$, that is, the quark-antiquark decays of the Z^0 . These events are selected by the basic multihadron event selection [26] to reduce the contamination of events of the type $e^+e^- \rightarrow \tau^+\tau^-$ (or $e^+e^-, \mu^+\mu^-$). This can be done by requiring, for example, at least 7 *good quality tracks* for the event. The concept of 'good quality track' will be discussed in detail in the next section. The efficiency of this selection is $(98.4 \pm 0.4)\%$. The inefficiency is mainly due to the geometrical acceptance of the detector. There are altogether 1,382,720 such multihadron events in the data sample which are used for this analysis.

than $250 \text{ MeV}/c$

* the number of signal wires which provide the hits for a specific track in the central tracking chamber has to be larger than 40, out of 159 maximum possible hits;

5.1 Track Quality

The reconstruction of the B^0 through the $B^0 \rightarrow D^* l \nu$ decay channel requires the detection of four tracks, namely, one lepton track, one kaon track and two pion tracks, corresponding to the final decay products in the decay chain $B^0 \rightarrow ((K\pi)\pi)l\nu$. The neutrino escapes the detector undetected. All the reconstructed tracks have to satisfy some minimum requirements (now standard for the OPAL detector) to ensure that they are well measured and well reconstructed. Tracks which satisfy these criteria are called 'good quality tracks', and will be used in the analysis of the reconstruction of B mesons.

Tracks selected for the B^0 search in this analysis are considered as 'good quality tracks' if they pass the following criteria:

- d_0 , the distance of closest approach of the track to the event vertex in the $r - \phi$ plane, has to be less than 0.5cm ;
- z_0 , the z-position at the point of closest approach of the track and the event vertex, has to be less than 20cm ;
- p_{xy} , the transverse momentum relative to the beam line, has to be larger than $250\text{ MeV}/c$;
- the number of signal wires which provide the hits for a specific track in the central tracking chamber has to be larger than 40, out of 159 maximum possible hits;

- at least two of the three tracks forming a D^* candidate are required to have either four z-chamber hits or have a “CJ endpoint”, which has been described in Section 2.1;
- each track must have been constrained successfully to the common event vertex in the the $r - \phi$ projection plane.

The efficiency of these track quality cuts will be estimated in section 5.3.

5.2 Event Selection

In order to reconstruct B^0 mesons in the decay chain $B^0 \rightarrow D^* l \nu$, an event sample with a lepton is obtained. Lepton candidates are identified by a set of selection criteria which has been optimized for the OPAL detector efficiency and signal-to-noise ratio. More details about this lepton identification will be discussed in Section 5.2.2. A D^* is reconstructed. For events containing an identified lepton, the invariant mass of the $D^* l$ is calculated. The reconstruction of B^0 through its semileptonic decay can be only *partially* accomplished since the neutrino is undetectable.

5.2.1 D^* selection

D^{*+-} mesons were identified through the following decay chain:

$$D^{*-} \rightarrow \pi_1^- D^0 \rightarrow \pi_1^- (K^- \pi_2^+)$$

where π_1 indicates a slow pion coming from the D^* decay. It tends to have lower momentum than the other pion coming from the D^0 decay. Because the mass difference between D^* and D^0 is very small, this leaves a very small amount of phase space for the pion from the D^* decay.

Firstly, all possible combinations of oppositely charged tracks in one event are combined to form D^0 or \bar{D}^0 candidates, assuming each track is a pion or kaon, without using any dE/dx information. The combination is retained if the invariant mass of this $K^+\pi^-$ (or $K^-\pi^+$) system lies within $\pm 75 \text{ MeV}/c^2$ of the nominal D^0 mass of $1864 \text{ MeV}/c^2$, which corresponds to about $\pm 2\sigma$ of the D^0 mass resolution.

$$\blacksquare \quad 1790 \text{ MeV}/c^2 < M(D^0)_{\text{cand}} < 1940 \text{ MeV}/c^2$$

Then each of the remaining tracks left in the event is assumed to be a pion, and each such track is added into a $K\pi$ combination to form a D^* candidate. Since the track is a candidate for the pion from the D^* decay (*i.e.* π_1), it is required to have the opposite charge of the pion track in the $K\pi$ combination. The invariant mass of this track and the D^0 candidate is calculated. It is accepted as a D^*

candidate if the mass difference, ΔM , of the D^* and the D^0 lies between $\pm 3\sigma$ in the ΔM resolution. i.e:

$$\blacksquare 0.142\text{GeV}/c^2 < \Delta M < 0.149\text{GeV}/c^2$$

Some of the candidates are random combinations of two tracks, known as combinatorial background.

A large suppression of the combinatorial background, especially at low $x(D^*)$ is achieved by exploiting the isotropic decay distribution of the D^0 in its own rest frame. The $x(D^*)$ is defined as the energy of the D^* candidate over the beam energy. Since the kaon and pion are both scalar particles (spin 0), there is no angle preference in the D^0 decay. That is, the decay is isotropic in the D^0 rest frame. For the background events in which the two selected tracks are not from a D^0 , the angular distribution in the D^0 rest frame, boosting them into the D^0 direction, will not have isotropic distribution. A requirement on the $\cos(\theta^*)$, where θ^* is defined as the angle between the direction of the kaon in the D^0 rest frame and the direction of the D^0 in the lab frame, can be used to help eliminate the combinatorial backgrounds. It is thus required that

$$\blacksquare \cos(\theta^*) < 0.8 \text{ for } x(D^*) < 0.5$$

$$\blacksquare \cos(\theta^*) < 0.9 \text{ for } x(D^*) > 0.5$$

In order to suppress the background at low $x(D^*)$ further, an additional require-

ment is implemented for the $x(D^*) < 0.5$ region. The probability of the dE/dX measurement for the kaon candidate has to be larger than 10%, which is equivalent to being about 1.64σ around the theoretical value of the dE/dx for a kaon. The background rate drops with increasing $x(D^*)$; therefore this requirement will not be applied for $x(D^*) > 0.5$ in order to increase the efficiency for the measurement in this region.

- $(dE/dX)_{weight} > 10\%$ for $x(D^*) < 0.5$
- no dE/dX requirement for $x(D^*) > 0.5$

Candidates with $x(D^*) < 0.2$ are not considered in this analysis because the combinatorial background rises rapidly in this region. The D^* from semileptonic B^0 decay must be accompanied by a lepton which has high momentum and high transverse momentum. The lepton identification will be sketched in the next subsection. Again, the invariant mass of this lepton track together with the D^* candidate is calculated and the combination is retained as a B^0 candidate.

Each event is divided into two hemispheres, each associated with one jet. For each event, the kaon and lepton are required to be in the same hemisphere. This is always the case for real D^*l events originating from B^0 decay. Among about 1,382,720 multihadron events taken with the OPAL detector at CERN during the running period between 1990 & 1992, about 75 such $B^0 \rightarrow D^*l\nu$ candidates meet all the selection criteria.

5.2.2 Lepton Identification

The lepton identification is performed by a standard identification package at OPAL. Detailed discussions about the identification criteria can be found in reference [27] and [28] for muon identification and reference [29] for electron identification. Only a brief description is presented here.

- *muon identification:*

As discussed in Chapter 2 of this thesis, track segments are reconstructed in the muon chambers. If the position of an extrapolated central detector track matches in both θ and ϕ the position of a muon chamber signal obtained using three out of a four possible layers of the muon chambers, the track is accepted as muon candidate. If more than one central detector track is associated with a muon segment, the track which is 'best' matched is taken as the muon candidate.

- *electron identification :*

The electron identification is based on the ionization loss dE/dx , measured in the jet chamber; the amplitude of the barrel presampler cluster associated with the central detector track (electrons will shower in the presampler while muons and hadrons will not); the lateral distribution of energy in the barrel lead-glass cluster associated with the track (on average, the energy of an electron shower is contained in a smaller number of blocks than that for a hadronic shower), and the comparison of the track

momentum with the lead-glass cluster energy. For the low momentum range, dE/dx alone is sufficient to separate electrons from misidentified hadrons. For the high energy range, the information from the presampler in the barrel region and lead-glass calorimeter information is necessary to keep this hadronic background low.

As discussed in Chapter 4 for the kinematic study using Monte Carlo simulated data, high momentum (p) and high transverse momentum (p_t) with respect to the jet direction is required for leptons to distinguish D^*l events from B decay from those produced by direct hadronization from c quarks, to obtain a b -enriched sample. The jet direction is obtained through the OPAL jet-finding routine using charged tracks and unassociated clusters in the electromagnetic calorimeter.

- $p_t > 0.8 \text{ GeV}/c$
- $p > 3 \text{ GeV}/c$

5.3 The Efficiency and Purity of the Event Selection

As discussed in section 5.1, the hadronic events have to pass a series of selection criteria to be considered B^0 candidates. In order to understand the criteria in terms of the efficiency and the purity of the selected sample, Monte Carlo simulations were performed. The output of a Monte Carlo simulated sample includes

the mass, energy, and momentum for each of the observable hadrons produced as well as complete information about all the intermediate hadrons. Therefore, the efficiency of the selection criteria can be calculated by examining how many generated B^0 pass the selection criteria. The purity is defined as the percentage of the number of generated B^0 Monte Carlo events in the reconstructed candidates, over the total number of the reconstructed B^0 candidates in the Monte Carlo sample.

The samples used here are known as *Primary Multihadron Monte Carlo events* which have been corrected for the efficiency responses of the OPAL detector in 1992. Every event is a decay of the type $Z^0 \rightarrow \text{Hadrons}$ and is generated by the JETSET7.3 Monte Carlo simulation package, with the Peterson fragmentation for charm and bottom quarks and Symmetric Lund fragmentation for light quarks. It includes a full simulation of all OPAL detectors.

In the given Monte Carlo simulation sample, there are 932 produced B^0 events which decay through the channel under study. However, of the four tracks for the final decay products (π_1, π_2, K and l), not all of them are well measured by the OPAL detector. Thus, the B^0 event may fail to be reconstructed. A closer look at the efficiencies of the 4 tracks using MC sample is shown by Table 5.1:

The error on the efficiency is calculated from equation 5.1 [30]

cut imposed	K	π_1	π_2	lepton(e, μ)
# of track in MC	932	932	932	932
good quality track	610(65.5%)	571(61.3%)	644(69.1%)	641(68.8%)
$(dE/dX)_{weight}^{Kaon}$	471(77.2%)	-	-	-
p and p_t	-	-	-	503(78.5%)
ϵ_{track}	471 (50.5 ± 1.6)%	571 (61.3 ± 1.6)%	644 (69.1 ± 1.5)%	503 (54.0 ± 1.6)%
ϵ_{D^*}		(21.4 ± 2.8)%		-
ϵ_l	-	-	-	(54.0 ± 1.6)%

Table 5.1: Efficiencies for track quality cuts on Monte Carlo Sample. Given in parentheses are percentages of tracks remained compared to previous selection after each cut

$$\Delta\epsilon_{eff} = \sqrt{\frac{\epsilon_{eff}(1 - \epsilon_{eff})}{N}} \quad (5.1)$$

If all the four tracks which form the B^0 candidates are required to be good tracks, the efficiency would be the product of the efficiencies for the four tracks, if there were no correlation between these efficiencies. This gives an efficiency of 11.6%. However, those efficiencies *do* have correlations since only 82 events are found out of 932 B^0 in the Monte Carlo data set which gives a total efficiency of $8.8\% \pm 3.1\%$.

The event selection and reconstruction are performed by trying different track combinations and by imposing the selection criteria on these tracks as discussed before. Eighty-two candidates in this Monte Carlo sample pass the

selection and are considered as B^0 candidates. Out of these 82 events, 75 events are generated B^0 which decay into the right channel which gives a purity of $(91.5 \pm 3.1)\%$. Seven events are background which are either not B^0 events but have met all selection requirements (4 events out of 7), or are true B^0 events but with either a 'fake' D^* with one of the K, π or π track being misidentified, or with a correct D^* but a misidentified lepton track (3 events out of 7).

In summary, Monte Carlo studies predict the efficiency of the selection to be $(8.8 \pm 3.1)\%$. Seventy-five B^0 candidates are reconstructed successfully and seven events are wrongly sampled. The purity of the reconstruction is therefore $(91.5 \pm 3.1)\%$.

A $x_E(B^0)$ plot for these background events is shown in Figure 5.1. There seems no obvious enhancement in any particular bin in the $x_E(B^0) > 0.2$ region which means the background should not distort the $x_E(B^0)$ shape for the signal events. However, this is statistically limited as only seven events are obtained from this Monte Carlo simulated background sample.

The following values for the branching ratios of various reactions in the decay chain are used in order to estimate the expected number of B^0 events from the data collected by the OPAL experiment:

$$Br(Z^0 \rightarrow q\bar{q} \rightarrow b\bar{b}) = 21.5\%$$

$$Br(\bar{b} \rightarrow B^0) = (44 \pm 12)\% [31]$$

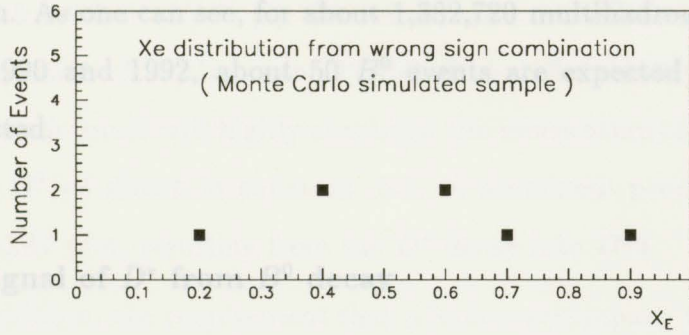


Figure 5.1: $x_E(B^0)$ plot for the background events (Monte Carlo)

$$Br(B^0 \rightarrow D^*lX) = (10.4 \pm 1.1)\% [32] \quad (l = e + \mu)$$

$$Br(D^* \rightarrow D^0\pi) = (55 \pm 4)\% [8]$$

$$Br(D^0 \rightarrow K\pi) = (3.65 \pm 0.21)\% [8]$$

With the identification efficiency for the selection being $(9.2 \pm 3.2)\%$ according to the previous calculation, the number of B^0 events expected from the multihadron data can be estimated as:

$$N_B \sim N_{hadron} \times Br(Z^0 \rightarrow b\bar{b}) \times 2 \times Br(\bar{b} \rightarrow B^0) \times Br(B^0 \rightarrow D^*lX) \\ \times Br(D^* \rightarrow D^0\pi) \times Br(D^0 \rightarrow K\pi) \times \epsilon_{eff}$$

$$= 1,382,720 \times 21.5\% \times 2 \times 44\% \times 10.4\% \times 55\% \times 3.65\% \times 8.8\%$$

$$\Delta M = M_{D^*} - M_{D^0} = (\sqrt{M_D^2 + 2P_{D^*} \cdot P_{D^0}}) - M_{D^*} \sim 50 \quad (5.3)$$

Both $\bar{b} \rightarrow B^0$ and $b \rightarrow \bar{B}^0$ are considered which contribute a factor of 2 in the calculation. As one can see, for about 1,382,720 multihadronic events recorded between 1990 and 1992, about 50 B^0 events are expected to be successfully reconstructed.

5.3.1 Signal of D^* from B^0 decay

The previously discussed D^* reconstruction and lepton identification are crucial in this analysis. For the D^* reconstruction, the decay chain in this analysis was chosen mainly for two reasons:

- it has the highest branching ratio for the semileptonic decay from B^0 ($(4.9 \pm 0.8)\%$);
- The decay of D^* into D^0 is a two body decay process. The relationship between the *four-vectors* for this decay of $D^* \rightarrow D^0\pi$ is

$$P_{D^*} = P_{D^0} + P_{\pi} \quad (5.2)$$

where the *four-vector* refers to (E, \vec{p}) . Since

$$P^2 = E^2 - \vec{p}^2 = M^2$$

the mass difference between the D^* and D^0 can be expressed as:

$$\Delta M = M_{D^*} - M_{D^0} = (M_{D^0}^2 + M_{\pi}^2 + 2P_{D^0} \cdot P_{\pi})^{1/2} - M_{D^0} \quad (5.3)$$

The mass of the D^* is $2010.1 \pm 0.6 \text{ MeV}/c^2$ while the mass of the D^0 is $1864.5 \pm 0.5 \text{ MeV}/c^2$ [8]. Therefore, the mass difference (ΔM as defined in equation 5.3) between D^* and D^0 is $145.6 \text{ MeV}/c^2$. This small difference in mass will highly constrain the momentum of the three particles (D^*, D^0, π) shown in equation 5.3. A prominent peak will be present in the ΔM plot, resulting from the D^* decay into $D^0\pi$.

In addition, the requirement that a lepton accompany the D^* in the same hemisphere provides a method to cleanly reconstruct B^0 candidate.

Figure 5.2 a) shows the ΔM plot for the data which pass the event selection. Due to the kinematic restriction, ΔM can not be less than $139.6 \text{ MeV}/c^2$ [8], which is the mass of a pion. The ΔM window is determined so that the background shape can also be retained and studied. There are 224 events in this mass window.

As one can see, a significant enhancement is apparent around $\Delta M = 145.6 \text{ MeV}/c^2$ due to the $D^* \rightarrow D^0$ transition. This signal is fit with a Gaussian peak and a smooth background, represented by a function of the form $A_2(\Delta M - m_\pi)^B$. The whole fitting function is shown below in equation 5.4. The background in the D^* region of the ΔM plot is very small, as can be seen in Figure 5.2 b)

$$F(\Delta M) = A_1 e^{-\frac{(\Delta M - \mu)^2}{2\sigma^2}} + A_2(\Delta M - m_\pi)^B \quad (5.4)$$

where A_1 and A_2 are normalization factors determined in the fit, μ and σ are the central value and the standard deviation respectively for the Gaussian peak; m_π is the mass of pion. The parameters A_1, A_2, μ, σ, B are left to be determined by the fit. Since the analysis is limited by statistics, the Log-likelihood method is used instead of the χ^2 fit.

Assuming a Gaussian shape for the signal, the peak value is found to be $(145.6 \pm 1.1) MeV/c^2$, in excellent agreement with the world average value of $145.4 \pm 0.06 MeV/c^2$ [8], and a width of $1.05 MeV/c^2$. The number of events under the Gaussian peak *above* the background and within 3σ of the peak position are considered as D^* signal. Together with a lepton (electron or muon) in the same hemisphere, the invariant mass of the D^*l can be calculated.

5.3.2 Background Estimation

The background to the D^* signal comes mainly from two sources. Random combinations from non-charmed particles is the dominant one. This leads to a smooth distribution in ΔM plot.

The background to the D^* signal can be estimated by taking events with the wrong charge correlations between the kaon and pion [33]. Normally, kaon and pion are of the opposite charge if they arise from the decay D^0 ; thus, an event with wrong-sign charge combination of $(K^\pm \pi_2^\pm) \pi_1^\mp$ is surely a background event to D^* , in comparison to the right-sign combination of $(K^\pm \pi_2^\mp) \pi_1^\pm$ for the

true D^* signal.

The selection procedure for the background events is identical to that for the B^0 signal. Leptons with the same charge sign as the kaon in the same hemisphere are used to form the ‘fake B^0 ’ with the ‘fake D^* ’. The combination of $K^\pm\pi^\pm\pi^\mp l^\pm$ is reconstructed for to estimate the background.

From 1,382,720 multihadron events from 1990 + 1991 + 1992 data, 112 such wrong-sign-combination events have been found. The ΔM plot (Figure 5.2 b.) shows no signal evident in the background. Again the plot is fitted with the same function as that used for the B^0 signal, using a maximum log-likelihood fit. No prominent peak is observed in the ΔM region around $0.1456\text{GeV}/c^2$ within 3 standard deviations. The smooth shape simulates the background of the signal very well. In Figure 5.2 b), the background is plotted with the same vertical scale as it is for the signal plot.

The wrong-sign combination method is just one way of estimating the background. It is also common practice to use the band on the two sides of the signal peak to evaluate the background. This is often referred as ‘the side-band’ method. This method is advantageous in performing the background subtraction. In the bin-by-bin measurement for the $x_E(B^0)$ which will be discussed later in Chapter 7, the side-band method is used to perform background subtraction.

5.3.3 Correction for the Missing ν Energy

In order to convert the measured energy of the D^*l into the energy of the B^0 , it is necessary to correct for the missing energy due to the undetected neutrino. This has been done on an event-by-event basis. One method of doing so is to estimate the B-meson energy (E_b^{corr}) by simply scaling the visible energy by the visible mass

$$E_b^{corr} = \frac{E_b^{D^*l} * m_{B^0}}{m_{D^*l}} \quad (5.5)$$

where $E_b^{D^*l}$ is the measured energy while m_{D^*l} is the invariant mass of the D^*l system. This expression has the desirable feature of asymptotically giving the correct result for $m_{D^*l} \sim m_{B^0}$.

In Figure 5.3 we compare the ratio of B hadron energy (E_b^{corr}) estimated using the above equation to the true B energy (E_b^{MCtree}) as a function of the visible mass for a Monte Carlo simulated sample.

Figure 5.3 a) shows the situation before the correction. Since E_{D^*l} is always less than E_{B^0} due to the undetected neutrino, the ratio of $E_b^{D^*l}$ to E_b^{MCtree} is always below 1. Figure 5.3 b) shows the effect after correction for the missing energy. At high M_{D^*l} , the neutrino contributes only a very small fraction of energy. $E_b^{D^*l}$ is then a good approximation to the B^0 meson energy. The figure

shows that there is very little dispersion about $E_b^{corr}/E_b^{MCtree} = 1$ for the high D^*l mass band. For the lower m_{D^*l} mass band however, the dispersion is observable, and it tends to provide a systematically high energy estimation for the total b-quark energy. Nevertheless this approximation is good to within $\sim 10\%$. The systematic error due to this correction will be discussed in Chapter 8.

In order to confirm that our B energy estimator is independent of the B energy spectrum, the ratio of the estimated B energy to the true B energy, E_b^{MCtree} , as a function of E_b^{MCtree} is examined. Figures 5.4 a) and b) show the situation before and after the correction respectively.

As one can see, there is no obvious variation along the whole energy range of the B meson after the correction and the ratio is centered around 1.

At OPAL, other estimators have been used to perform this correction:

- A modified relationship with higher order term, which becomes[12]:

$$E_b^{corr} = \frac{E_b^{D^*l} * m_{B^0}}{m_{D^*l}} * (1 + a_1 \Delta M + a_2 \Delta M^2)$$

where the above a_1 and a_2 are obtained from a fit of Monte Carlo data.

- A more elaborate method proposed [34] uses the relativistic boost factor γ_B based on the measured kinematics of the D^*l system.

These two methods give the correction to higher order terms but also introduce some systematic errors since the parameters used in these methods, a_1 and

a_2 for example, have to be determined. In this analysis, the first-order correction is sufficient, given the statistics. The small discrepancy of this correction for the low mass band of the D^*l system will be studied in Chapter 6.

In the next Chapter, the energy of the D^*l system for each B^0 candidate will be corrected for the missing neutrino. The ΔM plot is used to estimate the number of B^0 candidates in each energy bin after the correction to obtain the energy spectrum for the B^0 .

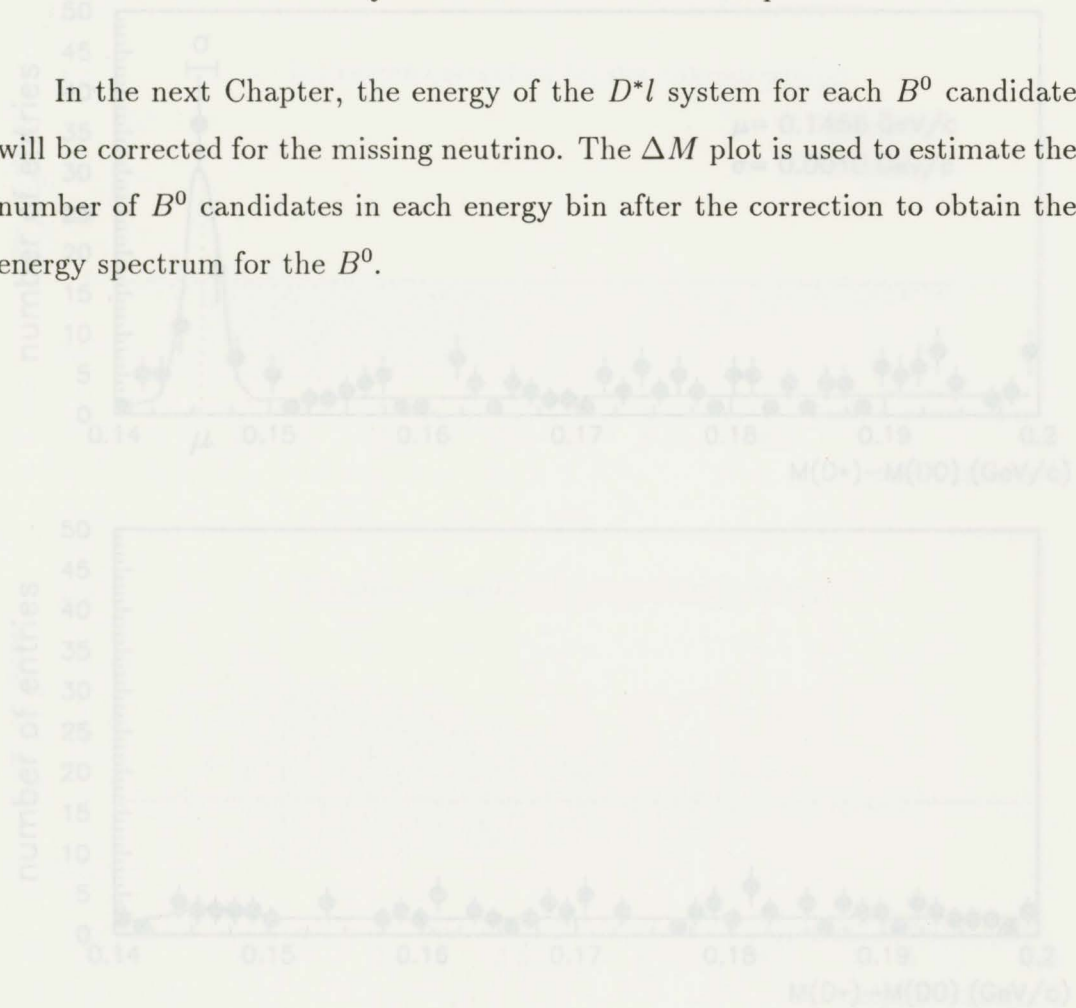


Figure 5.2: ΔM for events with a high p and p_l lepton in the same hemisphere (1990+1991+1992 data from OPAL); a) right-sign combination for signal; b) wrong-sign combination for the background

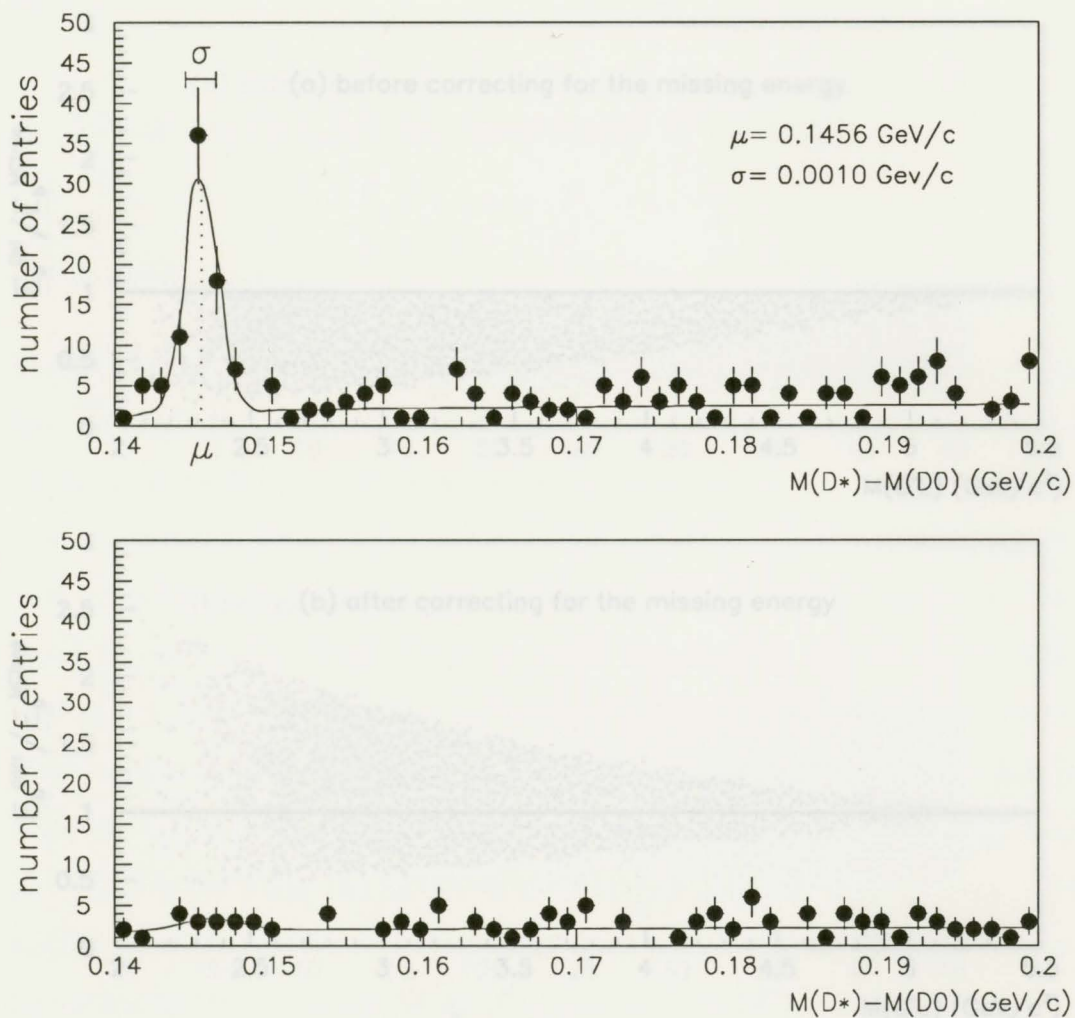


Figure 5.2: ΔM for events with a high p and p_t lepton in the same hemisphere (1990+1991+1992 data from OPAL); a) right-sign combination for signal; b) wrong-sign combination for the background

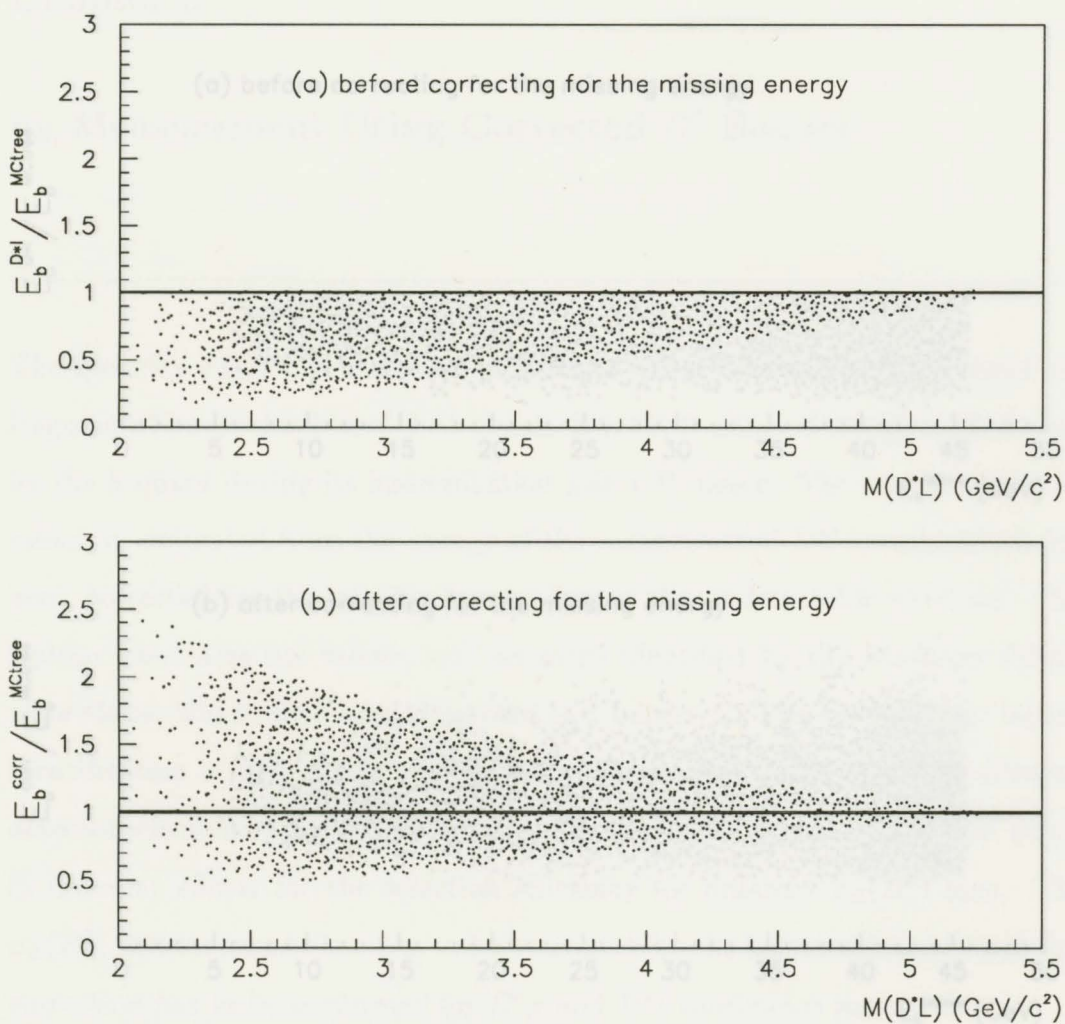


Figure 5.3: Correction for the missing energy; the effect of the correction as a function of $M(D^*l)$. a) $E_b^{D^*l}/E_b^{MCtree}$; b) E_b^{corr}/E_b^{MCtree} , where $E_b^{corr} = E_b^{D^*l} m_{B^0}/m_{D^*l}$

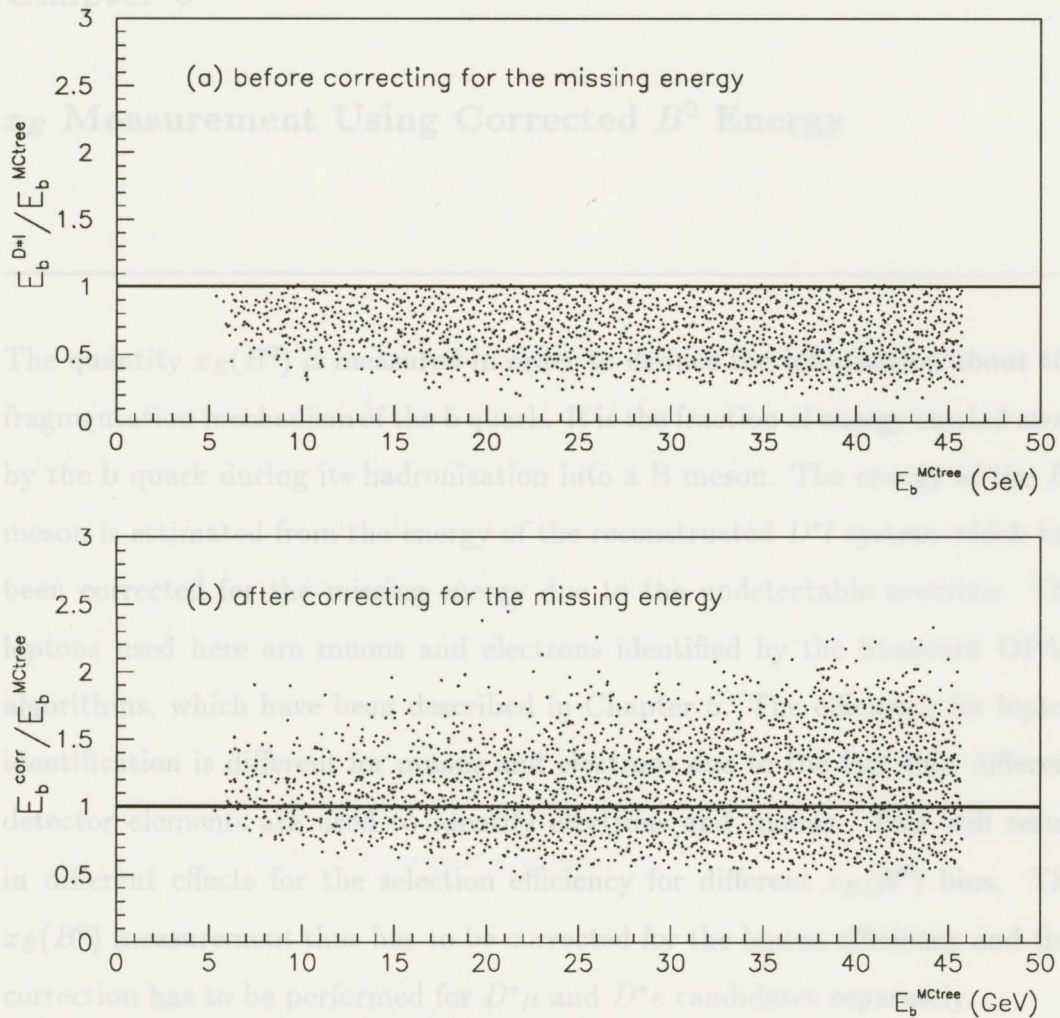


Figure 5.4: Correction for the missing energy; the effect of the correction as a function of E_b^{MCtree} . a) $E_b^{D^*l} / E_b^{MCtree}$. b) $E_b^{corr} / E_b^{MCtree}$, where $E_b^{corr} = E_b^{D^*l} m_{B^0} / m_{D^*l}$

6.1 The measurement of $x_E(B^0)$ distribution**Chapter 6** **x_E Measurement Using Corrected B^0 Energy**

The quantity $x_E(B^0)$ is measured in order to deduce the information about the fragmentation mechanism of the b quark. It is the fraction of energy carried away by the b quark during its hadronization into a B meson. The energy of the B^0 meson is estimated from the energy of the reconstructed D^*l system which has been corrected for the missing energy due to the undetectable neutrino. The leptons used here are muons and electrons identified by the Standard OPAL algorithms, which have been described in Chapter 5. The efficiency for lepton identification is different for muons and electrons due to the fact that different detector elements are used to identify electrons and muons. This will result in different effects for the selection efficiency for different $x_E(B^0)$ bins. The $x_E(B^0)$ measurement thus has to be corrected for the lepton efficiency and this correction has to be performed for $D^*\mu$ and D^*e candidates separately.

The momentum dependence of the muon identification efficiency will affect the shape of the detected $x_E(B^0)$ spectrum. Therefore, the measurement of the

6.1 The measurement of $x_E(B^0)$ distribution

The measurement is done in a bin-by-bin basis for six bins in the $x_E(B^0)$ spectrum, for x_E equals 0.2 to 1.0. The number of candidates for each $x_E(B^0)$ bin is obtained from the fitting result for each of the six ΔM samples for $D^*\mu$ candidates shown in Figure 6.1, and the six ΔM samples for D^*e candidates shown in Figure 6.2.

The ΔM plots are fit with the same fitting function described in equation 5.4. The statistics in each bin are low. To eliminate the binning effect, each plot is fitted using an unbinned log-likelihood method for this low statistical analysis. The curves shown are the fitting functions. The width of the D^* signal in the ΔM plot represents the mass resolution of the detector and it is known to be $0.845 \text{ MeV}/c^2$ from the Monte Carlo. Therefore, the fit was performed with a fixed value for the width.

The number of candidates per $x_E(B^0)$ bin is presented in Table 6.1. These are numbers before the efficiency correction.

6.1.1 Correction for muon efficiency

The momentum dependence of the muon identification efficiency will affect the shape of the detected $x_E(B^0)$ spectrum. Therefore, the measurement of the

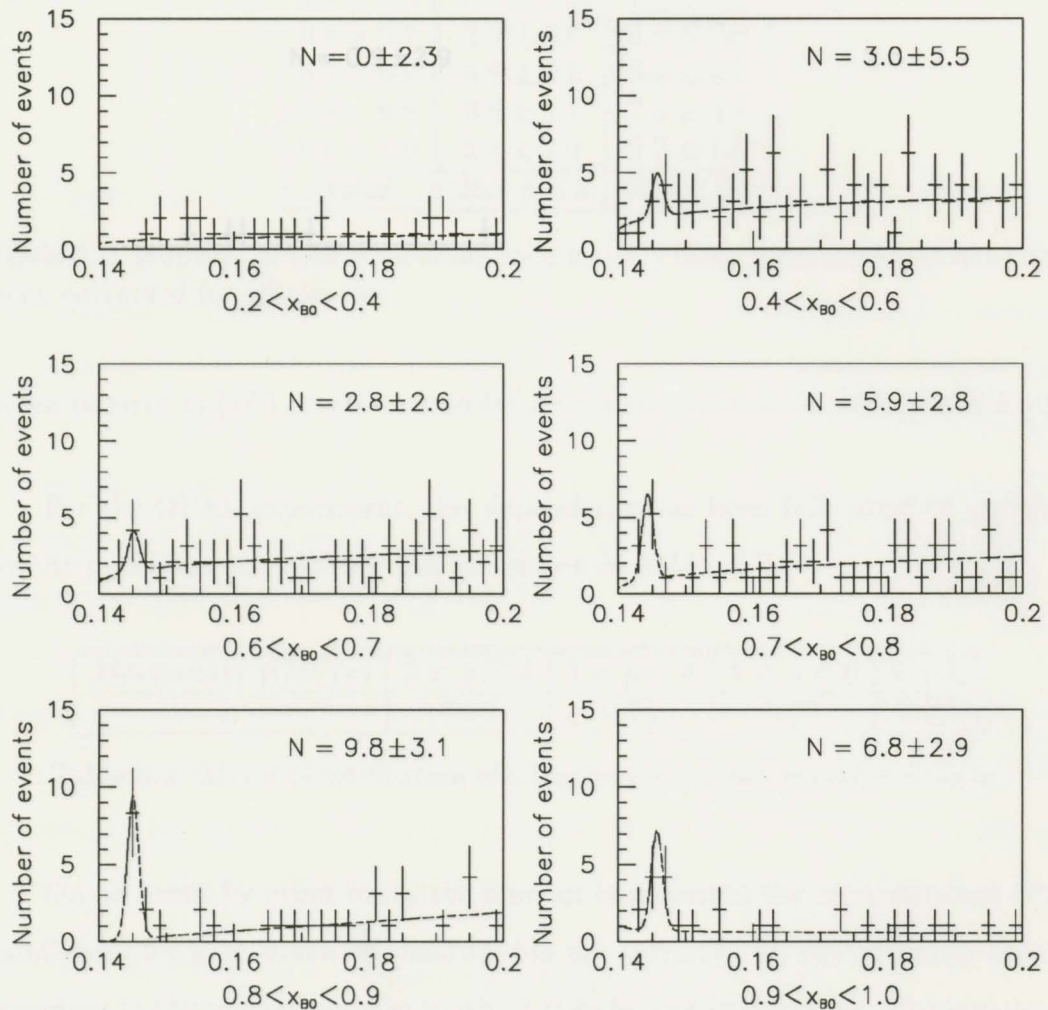


Figure 6.1: The ΔM plots for each $x_E(B^0)$ ($D^*\mu$). Each plot represents the fitting function for the D^*l signal in different bins of $x_E(B^0)$. The N on each plot shows the number of B^0 candidates, as well as its error, in that particular bin obtained from the fit.

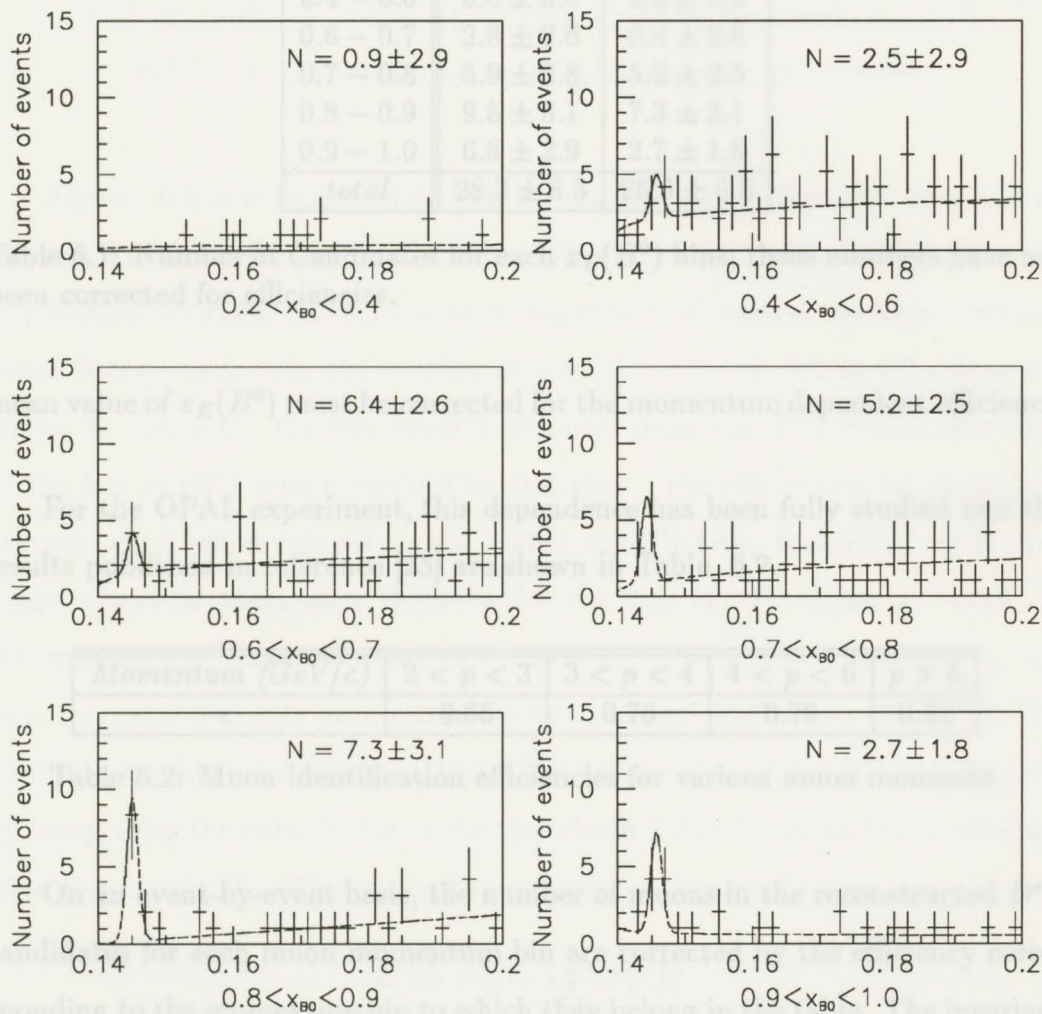


Figure 6.2: The ΔM plots for each $x_E(B^0)$ (D^*e). Each plot represents the fitting function for the D^*l signal in different bins of $x_E(B^0)$. The N on each plot shows the number of B^0 candidates, as well as its error, in that particular bin obtained from the fit.

$x_E(B^0)$	$D^*\mu$	D^*e
0.2 – 0.4	0.0 ± 2.3	0.9 ± 2.9
0.4 – 0.6	3.0 ± 5.5	2.5 ± 2.9
0.6 – 0.7	2.8 ± 2.6	6.4 ± 2.6
0.7 – 0.8	5.9 ± 2.8	5.2 ± 2.5
0.8 – 0.9	9.8 ± 3.1	7.3 ± 3.1
0.9 – 1.0	6.8 ± 2.9	2.7 ± 1.8
<i>total</i>	28.3 ± 8.3	25.0 ± 6.5

Table 6.1: Number of Candidates for each $x_E(B^0)$ bins; these numbers have not been corrected for efficiencies.

mean value of $x_E(B^0)$ must be corrected for the momentum dependent efficiency.

For the OPAL experiment, this dependence has been fully studied and the results published in reference [25] are shown in Table 6.2.

Momentum (GeV/c)	$2 < p < 3$	$3 < p < 4$	$4 < p < 6$	$p > 6$
ϵ	0.66	0.76	0.79	0.82

Table 6.2: Muon identification efficiencies for various muon momenta.

On an event-by-event basis, the number of muons in the reconstructed $D^*\mu$ candidates for each muon momentum bin are corrected by the efficiency corresponding to the momentum bin to which they belong in the table. The invariant mass of the $D^*\mu$ is recalculated. After applying the selection criteria for the B meson reconstruction, the efficiencies for each $x_E(B^0)$ bin are obtained. Taking into account the efficiencies for the event selection, the momentum dependence of the efficiencies for the reconstruction of $D^*\mu$ events are shown in Table 6.3.

$x_E(B^0)$	0.2 – 0.4	0.4 – 0.6	0.6 – 0.7	0.7 – 0.8	0.8 – 0.9	0.9 – 1.0
ϵ_{eff}	0.13	0.13	0.26	0.25	0.36	0.502
$\Delta\epsilon_{eff}$	0.04	0.02	0.06	0.04	0.06	0.08

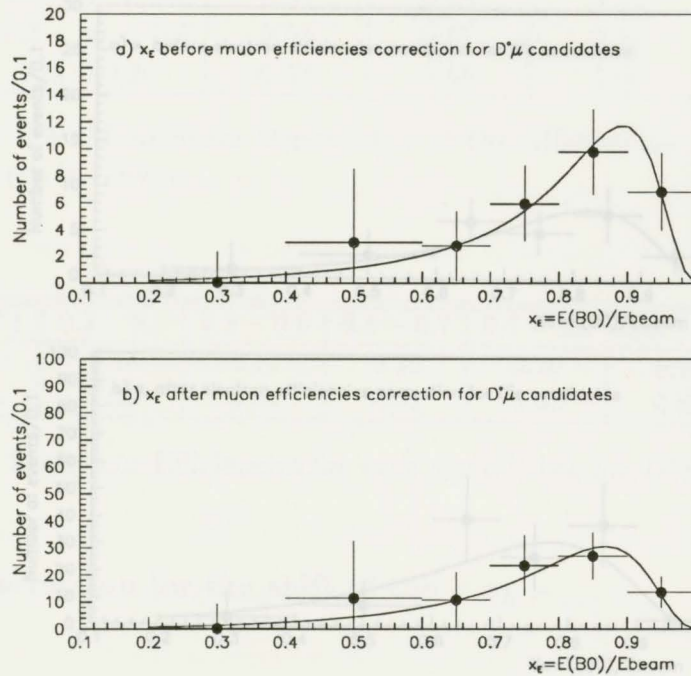
Table 6.3: Efficiencies for each $x_E(B^0)$ bin for $D^*\mu$ events.

Figure 6.3 and Figure 6.4 show the $x_E(B^0)$ plot before and after the efficiency correction for the $D^*\mu$ and the D^*e respectively. Recall that since the requirement of $x_E(B^0) > 0.2$ has been imposed to eliminate the high combinatorial background, only the number of candidates in the 0.2 to 1.0 region are shown in the plot. For the $x_E(B^0)$ obtained from the $D^*\mu$ events, the data of the low $x_E(B^0)$ bins is limited by statistics. The efficiencies for these bins are also very low compared to the higher $x_E(B^0)$ bins, which will yield even bigger errors for these bins. However, for the high $x_E(B^0)$ region on which the determination of the distribution of the fitting function as well as the $\langle x_E \rangle_{B^0}$ rely, the measurements have relatively small errors. Both plots are fitted with the Peterson fragmentation function. The mean value of $x_E(B^0)$ is calculated by integrating the fitted Peterson function from 0.2 to 1.0 using the ϵ_b obtained from the fit. For the $D^*\mu$ events, this quantity is measured to be

$$\langle x_E \rangle_{B^0}^{\mu} = 0.732_{-0.033}^{+0.028}$$

The momentum dependence of the electron identification efficiency has been studied in detail, and the efficiencies for each momentum bin are shown in Table 6.4 [25], in which the uncertainty is statistical only.

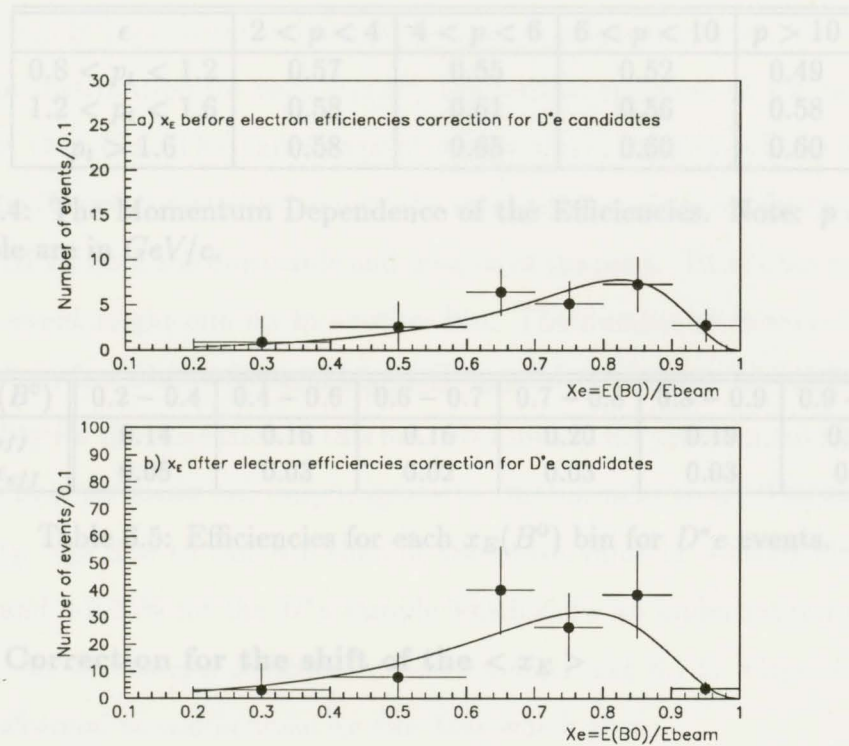
Having been corrected for these electron identification efficiencies, and also including the efficiencies for the event selection, the momentum dependent effi-

Figure 6.3: The $x_E(B^0)$ spectrum for $D^*\mu$

6.1.2 Correction for electron efficiency

The momentum dependence of the efficiencies for electrons has been studied in detail, and the efficiencies for each momentum bin are shown in Table 6.4 [25].

Having been corrected for these electron identification efficiencies, and also including the efficiencies for the event selection, the momentum dependent effi-

Figure 6.4: The $x_E(B^0)$ spectrum for D^*e .

efficiencies for each $x_E(B^0)$ for D^*e events are presented in Table 6.5. The data for $x_E(B^0)$ before and after the efficiency correction are shown in Figure 6.4. The mean value of $x_E(B^0)$ for the D^*e is measured to be

$$\langle x_E \rangle_{B^0}^e = 0.674_{-0.033}^{+0.030}$$

Again, the uncertainty here is statistical only.

ϵ	$2 < p < 4$	$4 < p < 6$	$6 < p < 10$	$p > 10$
$0.8 < p_t < 1.2$	0.57	0.55	0.52	0.49
$1.2 < p_t < 1.6$	0.58	0.61	0.56	0.58
$p_t > 1.6$	0.58	0.65	0.60	0.60

Table 6.4: The Momentum Dependence of the Efficiencies. Note: p and p_t in the Table are in GeV/c .

$x_E(B^0)$	0.2 – 0.4	0.4 – 0.6	0.6 – 0.7	0.7 – 0.8	0.8 – 0.9	0.9 – 1.0
ϵ_{eff}	0.14	0.16	0.16	0.20	0.19	0.70
$\Delta\epsilon_{eff}$	0.05	0.03	0.02	0.03	0.03	0.3

Table 6.5: Efficiencies for each $x_E(B^0)$ bin for D^*e events.

6.1.3 Correction for the shift of the $\langle x_E \rangle$

The B^0 energy is obtained by scaling up the E_{D^*l} using the ratio of M_{B^0}/M_{D^*l} . As shown in Figure 5.4 in Chapter 5, this estimator is independent of the B energy spectrum. The spread of the ratio E_b^{corr}/E_b^{MCtree} about the value of unity shows the imperfection of the detector resolution and the effect of the neutrino energy correction. The resolutions, obtained by projecting Figure 5.4 to the y-axis for the six x_E bins, are slightly different from bin to bin. For example, the resolution is 0.13 when $x_E(B^0) = 0.3$, and the value is 0.17 when $x_E(B^0) = 0.9$. They are almost Gaussian distributions. However, the mean values of these Gaussian distributions are all slightly above unity by about 6% on average. Also, the resolution is larger than the bin width, so a D^*l event

reconstructed in one bin might be corrected to another bin which affects the shape of $x_E(B^0)$ spectrum and hence the $\langle x_E \rangle_{B^0}$ measurement. The projected Gaussian distribution for each $x_E(B^0)$ bin will be centered at 6% beyond the center of that bin. The percentage of events which are beyond the bin width under the Gaussian distribution over the total number of events for each bin was calculated for both the down-side and up-side of the peak. This is the probability that an event might end up in another bin. The number of events that might migrate to other bins is the number of B^0 candidates in that bin multiplied the probability for the migration in this bin. To simplify the problem, an assumption is made that an event can only migrate to the bin next to it. The changes on the $\langle x_E \rangle_{B^0}$ due to this 6% shift of the mean value is +4.93% for the D^*e sample and +5.95% for the $D^*\mu$ sample which show an under-estimation of the $\langle x_E \rangle$ for the results obtained in Section 6.1.1 and 6.1.2. Corrections have been performed to compensate for this bias which give:

$$\langle x_E \rangle_{B^0}^{\mu} = 0.776_{-0.032}^{+0.029}$$

$$\langle x_E \rangle_{B^0}^e = 0.707_{-0.035}^{+0.032}$$

6.1.4 Combining the D^*e and $D^*\mu$ spectra

The numbers of events for six different $x_E(B^0)$ bins after being corrected for the event selection efficiency and the lepton identification efficiency are shown in the first two columns in Table 6.6.

$x_E(B^0)$	D^*e	$D^*\mu$	D^*l ($l = e, \mu$)	# of events/0.1 in x_E
0.2 – 0.4	6.2 ± 20.3	0.0 ± 18.4	5.7 ± 27.2	2.9 ± 13.6
0.4 – 0.6	15.7 ± 18.5	22.9 ± 42.1	33.8 ± 33.8	16.9 ± 16.9
0.6 – 0.7	40.3 ± 17.1	10.9 ± 10.5	37.8 ± 17.9	37.8 ± 17.9
0.7 – 0.8	26.7 ± 13.5	23.3 ± 11.7	49.5 ± 17.6	49.5 ± 17.6
0.8 – 0.9	38.4 ± 17.4	27.1 ± 9.7	59.6 ± 16.9	59.6 ± 16.9
0.9 – 1.0	3.9 ± 3.1	13.5 ± 6.2	11.5 ± 5.5	11.5 ± 5.5

Table 6.6: The numbers of B^0 events in each $x_E(B^0)$ bin **after** being corrected for lepton identification efficiencies and the efficiencies for the event selection.

In the Standard Model the b fragmentation mechanism should be the same for the process $B^0 \rightarrow e$ as it is for $B^0 \rightarrow \mu$. The results obtained for the D^*e and $D^*\mu$ samples are thus combined to obtain better statistics.

For the i th bin, if there are two measurements of the same physical quantity n_i^e and n_i^μ , with standard deviation σ_i^e and σ_i^μ respectively, the best estimation of the average measurement n_i and its uncertainty σ_i are given by [35]

$$n_i = \frac{n_i^e/(\sigma_i^e)^2 + n_i^\mu/(\sigma_i^\mu)^2}{1/(\sigma_i^e)^2 + 1/(\sigma_i^\mu)^2}$$

and

$$1/\sigma_i^2 = 1/(\sigma_i^e)^2 + 1/(\sigma_i^\mu)^2$$

It is assumed that the branching ratio for $B^0 \rightarrow D^*e\bar{\nu}$ is the same as that for $B^0 \rightarrow D^*\mu\bar{\nu}$, apart from the effects of the lepton mass, which is insignificant compared to the B^0 energy for this data sample. Therefore, the efficiency corrected D^*e and $D^*\mu$ samples should each contribute half of the total number of

signal events for the $B^0 \rightarrow D^* l \bar{\nu}$ decay. The result is therefore

$$N_{i \text{ bin}} \pm \text{error} = 2 \times (n_i \pm \sigma_i)$$

The total numbers of events for each bin thus obtained are listed in the third column of Table 6.6 and the $x_E(B^0)$ spectrum for the combined result can be found in Figure 6.5. This spectrum is then fit to the Peterson function. The effect on $\langle x_E \rangle$ introduced in by the 6% shift of the mean value when correcting for the missing neutrino energy, is taken to be 5.29% for the combined sample (the average value from the $D^* \mu$ and $D^* e$ sample). The corrected mean value of $x_E(B^0)$ and its corresponding ϵ_b is

$$\langle x_E \rangle_{B^0}^{\text{comb}} = 0.741_{-0.028}^{+0.025}$$

$$\epsilon_b = 0.0019_{-0.0018}^{+0.0028}$$

in which the error is statistical only.

6.2 Evaluation of the Systematic Error

The sensitivity of the measurement of the mean $x_E(B^0)$ to various systematic effects is discussed. Each independent source of error is considered separately and the errors is added in quadrature to obtain the final systematic error.

The CLEO collaboration considered the free quark model of Altarelli *et*

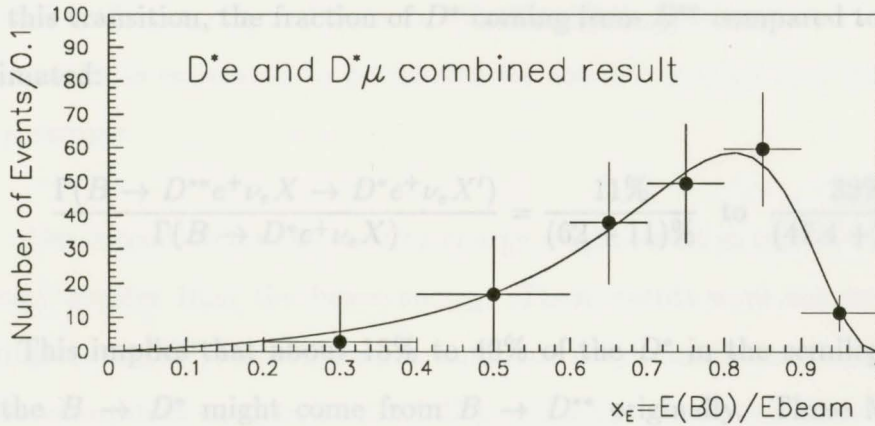


Figure 6.5: The $x_E(B^0)$ spectrum obtained using the D^*e and $D^*\mu$ combined samples.

al [36], and two forms of the decay models of Isgur *et al* [37]. The original model of Isgur *et. al.* (ISGW) predicts that the decays $B \rightarrow De^+\nu_e X$, $B \rightarrow D^*e^+\nu_e X$, and $B \rightarrow D^{**}e^+\nu_e X$, in which the D^{**} would then decay into D^* , have branching ratios of 27%, 62%, and 11% respectively of all semileptonic $B \rightarrow D$ decay modes. The D^* from the D^{**} decay with a high p and high p_t lepton will provide a softened B^0 energy spectrum. A modified version of the ISGW model (ISGW**) was also considered by CLEO where the relative rates to D and D^* were held constant while the branching ratio to D^{**} was increased to 32% of the total. This corresponds to the branching ratios for the decays $B \rightarrow De^+\nu_e X$, $B \rightarrow D^*e^+\nu_e X$, and $B \rightarrow D^{**}e^+\nu_e X$ to be 20.6%, 47.4% and

32% respectively of all semileptonic $B \rightarrow D$ decay modes. The branching ratio for $D^{**} \rightarrow D^* X$ has not been well measured yet. If a 100% decay rate is assumed for this transition, the fraction of D^* coming from D^{**} compared to the total is estimated:

$$\frac{\Gamma(B \rightarrow D^{**} e^+ \nu_e X \rightarrow D^* e^+ \nu_e X')}{\Gamma(B \rightarrow D^* e^+ \nu_e X)} = \frac{11\%}{(62 + 11)\%} \text{ to } \frac{32\%}{(47.4 + 32)\%}$$

This implies that about 15% to 40% of the D^* in the semileptonic decay of the $B \rightarrow D^*$ might come from $B \rightarrow D^{**}$ originally. Three Monte Carlo samples are generated using JETSET, with the first two having the branching ratios for the $B \rightarrow D(D^*, D^{**} l \nu X)$ following the ISGW (15% D^{**}) and ISGW** models (40% D^{**}) while the third sample contains 3% D^{**} , an estimated lower limit for the fraction of D^{**} over the semileptonic decay of $B \rightarrow D$ branching ratio. Assuming that the real data contains 15% of the D^* from the D^{**} decay (as in the ISGW model), the differences on the $\langle x_E \rangle_{B^0}$ measured for the simulated samples with D^{**} fraction varies from 15% up to 40% and down to 3% are then assigned to the $\langle x_E \rangle_{B^0}$ measured from the data as the systematic uncertainties. This uncertainty is also referred to as the *modeling effect for the semileptonic decay of the b-quark* [14]. Since the D^* s from the D^{**} s are among the second generation of decay products from the B^0 s, their momenta must be lower than that of the D^* s arising directly from the B^0 decay. This will result in an uncertainty of +0.006 and -0.005 on $\langle x_E \rangle_{B^0}^e$. The uncertainty from this source is the same for the $D^* \mu$ sample.

The systematic error due to the 6% shift of the center of the mean of the Gaussian when correcting for the missing neutrino energy is estimated by varying the 6% shift up to 8% and down to 4%. The systematic error on $\langle x_E \rangle_{B^0}$ from this source is estimated to be ± 0.010 for the D^*e sample and ± 0.012 for the $D^*\mu$ sample.

The correction for the missing energy might result in events with corrected energy greater than the beam energy. These events were not included when fitting the $x_E(B^0)$ to the Peterson function. A systematic error thus arises from this. In our data sample, $2.5 \pm 3.2 D^*\mu$ and $5.2 \pm 3.5 D^*e$ candidates are of this kind. The averaged $x_E(B^0)$ is calculated with and without these events. This results in changes of $+0.0240$ and $+0.0118$ on $\langle x_E \rangle_{B^0}$ for the $D^*\mu$ and the D^*e samples respectively.

Fixing the width of the Gaussian to 0.845 MeV when fitting the ΔM plots for various bins using equation 5.4 introduces in another systematic error. The value to which the width is fixed reflects the detector resolution. It was obtained from the Monte Carlo and has a Gaussian error of 0.1 MeV . By refitting the ΔM plots for the six $x_E(B^0)$ bins, with a fixed width of 0.745 MeV and 0.945 MeV respectively, and by recalculating the number of events in each bin for the $x_E(B^0)$ spectrum for the $\langle x_E \rangle_{B^0}$ measurement, this systematic error is probed. The uncertainty is estimated to be $+0.0013$ and -0.0011 on the $\langle x_E \rangle_{B^0}$.

A summary of the systematic error studies is listed in Table 6.8 and Table 6.9. The systematic error in the lepton identification efficiency has been studied [38] and is 3% for muon identification and 5% for electron identification. The

effects on ϵ_b due to these uncertainties are also given in the reference. The same results are used here for the ϵ_b which contributed an error of +0.0002 and -0.0002 on $\langle x_E \rangle_{B^0}^e$. The error on the $\langle x_E \rangle_{B^0}^\mu$ is estimated to be +0.001 and -0.001.

For the combined sample of D^*e and $D^*\mu$, the systematic errors from the first two sources are common for the $D^*\mu$ and D^*e sample in the $\langle x_E \rangle_{B^0}$ measurement. They are counted only once for the systematic uncertainty for the combined sample which are estimated to be +0.006 and -0.005 on $\langle x_E \rangle_{B^0}$. The uncertainties due to the correction for the missing neutrino energy and the lepton identification are different for D^*e and $D^*\mu$ and are added in quadrature together with the systematic error from the common origin. This gives the total uncertainty of +0.032 and -0.016 on $\langle x_E \rangle_{B^0}^{e,\mu}$.

The systematic uncertainty for ϵ_b can be estimated from the relationship shown in Figure 3.7, given the $\langle x_E \rangle_{B^0}$ and its uncertainties. The ϵ_b which is very sensitive to $\langle x_E \rangle_{B^0}$. However, the common systematic errors on the $\langle x_E \rangle_{B^0}$, which come from the $D^*\mu$ and D^*e samples respectively, have different effects on the ϵ_b measurement due to the non-linear relationship between $\langle x_E \rangle_{B^0}$ and ϵ_b . All the errors are thus added in quadrature to estimate the systematic uncertainty on ϵ_b for the combined sample.

A summary of the systematic error studies is listed in Table 6.8 and Table 6.9. The largest error arises from discarding the candidates in the $x_E(B^0) > 1$ region. This uncertainty is more than two times larger than the other errors com-

binned. If this source of error could be eliminated, the systematic uncertainty on $x_E(B^0)$ would be dominated by the uncertainty due to the lepton identification efficiency and the uncertainty on the fraction of the D^* from the D^{**} . Recall that the previous OPAL measurement, obtained using leptons from decays of the primary b hadrons, quoted a systematic error on $\langle x_E \rangle_{B^0}$ to be 0.022[14]; a much smaller systematic uncertainty can be obtained if this dominant error can be removed. An alternative method will be presented in the next Chapter to serve this purpose.

From 1990 to 1992, OPAL has collected about 1,382,720 $Z^0 \rightarrow q\bar{q}$ events. In this analysis, about 75 B^0 events have been partially reconstructed through their decay products D^*e or $D^*\mu$. Using the corrected B^0 energy, the results for the $\langle x_E \rangle_{B^0}$ and ϵ_b measurement are listed in Table 6.7 for the D^*e , the $D^*\mu$ and the combined samples respectively.

<i>result</i>	$D^*\mu$	D^*e	$D^*l(l = e, \mu)$
ϵ_b^{corr}	$0.0003^{+0.0015+0.0013}_{-0.0002-0.0017}$	$0.0055^{+0.0058+0.0048}_{-0.0034-0.0023}$	$0.0019^{+0.0028+0.0026}_{-0.0018-0.0051}$
$\langle x_E \rangle_{B^0}^{corr}$	$0.776^{+0.029+0.018}_{-0.032-0.013}$	$0.707^{+0.032+0.027}_{-0.035-0.011}$	$0.741^{+0.025+0.032}_{-0.028-0.016}$

Table 6.7: The results for the $\langle x_E \rangle_{B^0}$ and ϵ_b measurement for the D^*e , the $D^*\mu$ and the combined samples using the corrected B^0 energy.

Systematic uncertainties (D^*e)	$\Delta \langle x_E \rangle_{B^0}$		$\Delta \epsilon_b (10^{-3})$	
	-	+	-	+
fraction of D^* from D^{**} variation from 15% up to 40% and down to 3%	0.005	0.006	1.2	1.2
fitting method	0.0011	0.0013	0.28	0.25
correction for missing mass (6% shift varying by $\pm 2\%$)	0.0100	0.0100	2.0	2.0
correction for missing mass (cutoffs for $x_E(B^0) > 1$)	0.00	0.0240	4.2	0.00
lepton identification efficiency for electron ($\pm 5\%$)[38]	0.0002	0.0002	0.05[38]	0.05[38]
TOTAL	0.011	0.027	4.8	2.3

Table 6.8: Change in the $\langle x_E \rangle_{B^0}$ and the Peterson parameter ϵ_b from various sources of systematic uncertainties (D^*e)

Systematic uncertainties ($D^*\mu$)	$\Delta \langle x_E \rangle_{B^0}$		$\Delta \epsilon_b (10^{-3})$	
	-	+	-	+
fraction of D^* from D^{**} vary from 15% to 40% and down to 3%	0.005	0.006	0.57	0.50
fitting method	0.0011	0.0013	0.13	0.11
correction for missing mass (6% shift varying by $\pm 2\%$)	0.012	0.012	1.2	1.2
correction for missing mass (cutoffs for $x_E(B^0) > 1$)	0.00	0.0118	1.10	0.00
lepton identification efficiency for muon ($\pm 3\%$) [38]	0.0010	0.0010	0.10[38]	0.10[38]
TOTAL	0.013	0.018	1.7	1.3

Table 6.9: Change in the $\langle x_E \rangle_{B^0}$ and the Peterson parameter ϵ_b from various sources of systematic uncertainties ($D^*\mu$)

Chapter 7

x_E Measurement Using Only D^*l Energy

The measurement of the spectrum for $x_E(B^0)$ described in the previous Chapters involves scaling up from the measured D^*l energy to the B^0 energy in order to correct for the missing neutrino energy. From the systematic error analysis, it is apparent that the largest error comes from this estimation. Another method is thus discussed below with the aim at eliminating this systematic error. This is done by extracting the ϵ_b *without* correcting for the missing energy.

7.1 Introduction

Instead of $x_E(B^0)$, the spectrum of $x_E(D^*l)$ is measured, where $x_E(D^*l)$ is defined as the energy of D^*l over the beam energy. The shape of this spectrum also contains the information for b-quark fragmentation. In GOPAL, the spectrum of $x_E(D^*l)$ from B^0 decay can be *simulated* with various ϵ_b . The selection criteria imposed on this Monte Carlo sample are exactly the same as those imposed on the data. The only difference between the $x_E(D^*l)$ distributions for the Monte

Carlo simulated sample and for the data is that, the ϵ_b is a known parameter for the former. It is one of the input parameters when the Monte Carlo samples are generated. This parameter, together with a set of OPAL-tuned parameters, will determine how quarks are going to fragment into hadrons and what fraction of energy, on average, the heavy mesons are going to carry away from the primary quarks. The parameter is chosen such that the heavy quarks fragment according to the Peterson fragmentation scheme.

Taking advantage of this, a series of Monte Carlo samples are generated with various ϵ_b values, resulting in a series of $x_E(D^*l)$ spectra. These $x_E(D^*l)$ distributions are compared to the $x_E(D^*l)$ distribution obtained from the data measurement. The value of ϵ_b used to generate the best fit between these spectra can be found using the χ^2 fitting method. This ϵ_b will then be used to obtain the mean value of x_E .

7.2 The measurement of the $x_E(D^*l)$ distribution

The measurement is done using the same technique as has been described in Chapter 6 except that $x_E(B^0)$ is replaced by $x_E(D^*l)$. The number of candidates for each $x_E(D^*l)$ bin is obtained by counting the number of candidates under the signal peak within 3 standard deviations of the signal peak in each of the six ΔM samples for the D^*l candidates.

The number of candidates per $x_E(D^*l)$ bin is presented in Table 7.1. These are numbers before the efficiency correction.

$x_E(D^*l)$	$D^*\mu$	D^*e
0.2 - 0.4	6.1 ± 3.1	4.9 ± 2.9
0.4 - 0.6	6.2 ± 3.3	9.8 ± 3.8
0.6 - 0.7	11.6 ± 3.6	9.6 ± 3.6
0.7 - 0.8	5.9 ± 2.8	5.2 ± 2.6
0.8 - 0.9	0.9 ± 1.0	3.0 ± 1.7
0.9 - 1.0	0.8 ± 2.3	0.0 ± 2.3
<i>total</i>	31.5 ± 6.9	32.5 ± 7.1

Table 7.1: Number of Candidates for each $x_E(D^*l)$ bins before efficiency correction.

The number of events in each measured bin follows a Gaussian distribution:

The spectra are then corrected for the lepton identification efficiencies and event selection efficiencies. The numbers of candidates for each $x_E(D^*l)$ bin for D^*e samples, $D^*\mu$ samples and $D^*l(l = e, \mu)$ combined samples are listed in Table 7.2. These numbers result from the maximum likelihood fits to the unbinned data, performed using the same technique as described in section 6.1. These spectra are thus ready to be compared with the Monte Carlo samples with different values of ϵ_b .

where y_i is the expected bin content or value of bin i ; n_i is the actual bin content of bin i and N is the total number of bins. The P_{total} is the likelihood of the measured distribution for a given theoretical distribution.

$x_E(D^*l)$	$D^*\mu$	D^*e	$D^*l(l = e, \mu)$	# of $D^*l/0.1$ in x_E
0.2 – 0.4	22.6 ± 8.7	23.9 ± 14.7	45.9 ± 15.0	22.9 ± 7.5
0.4 – 0.6	20.7 ± 18.5	43.3 ± 17.1	65.7 ± 25.1	32.9 ± 12.5
0.6 – 0.7	35.6 ± 8.4	38.9 ± 17.4	72.4 ± 15.2	72.4 ± 15.2
0.7 – 0.8	17.5 ± 8.3	20.1 ± 10.0	37.1 ± 12.8	37.1 ± 12.8
0.8 – 0.9	2.5 ± 8.4	10.8 ± 6.5	15.4 ± 10.3	15.4 ± 10.3
0.9 – 1.0	1.2 ± 4.3	0.0 ± 4.6	1.2 ± 6.2	1.2 ± 6.2

Table 7.2: Number of Candidates for each $x_E(D^*l)$ bins **after** efficiency correction.

7.3 Calculating the χ^2

The number of events in each measured bin follows a Gaussian distribution:

$$P(n_i; \sigma_i, y_i) = \frac{1}{\sigma_i \sqrt{2\pi}} e^{-\frac{(n_i - y_i)^2}{2\sigma_i^2}}$$

The total probability is the product of the $P(n_i; y_i)$ for each bin i , which gives us :

$$P_{total} = \prod_{i=1}^N P_i = \prod_{i=1}^N \frac{1}{\sigma_i \sqrt{2\pi}} e^{-\frac{(n_i - y_i)^2}{2\sigma_i^2}}$$

where y_i is the expected bin content or value of bin i ; n_i is the actual bin content of bin i and N is the total number of bins. The P_{total} is the likelihood of the measured distribution for a given theoretical distribution.

Taking the natural log of the above equation will give us:

$$\text{Log}(P_{total}) = \text{Log}(1/\sqrt{2\pi})^N \prod_{i=1}^N \frac{1}{\sigma_i} - \sum_{i=1}^N \frac{(n_i - y_i)^2}{2\sigma_i^2}$$

This is the so called 'Log-likelihood'. The bigger this number is, the more likely the two distributions are the same. So the maximum of the this 'Loglikelihood' shows the best fit. Considering the $\text{Log}(1/\sqrt{2\pi})^N \prod_{i=1}^N \frac{1}{\sigma_i}$ as a constant for the measured spectrum,

$$\text{max}[\text{Log}(P_{total})] = \text{max} \sum_{i=1}^N -\frac{(n_i - y_i)^2}{2\sigma_i^2}$$

or equivalently, minimize the χ^2 :

$$\chi^2 = -\text{Log}(P_{total}) = \sum_{i=1}^N \frac{(n_i - y_i)^2}{\sigma_i^2}$$

χ^2 is the quantity that is being calculated for each comparison of the Monte Carlo distribution with the data. Here, y_i is the number of entries in bin i from the Monte Carlo distribution, and n_i is that from data. The error on the n_i entry in bin i is σ_i , and was determined by the fits described in Section 7.2, listed in Table 7.2. This method is also called the *least squares* fitting method.

The results of $\chi^2(\epsilon_b)$, the χ^2 of the fit with respect to the corresponding ϵ_b are shown in Figure 7.1 for $D^*\mu$, D^*e , the combined result of the D^*e and $D^*\mu$ sample respectively. The two distributions used for the fit have 6 bins each with only one parameter, ϵ_b , which varies. Therefore the number of the degree of freedom for this fit is five.

The ϵ_b which corresponds to the minimum of the χ^2 , χ_{min}^2 , is the one best describing the data spectrum. An associated error on the ϵ_b is given by seeing how much ϵ_b must be altered in order to make χ^2 increase from χ_{min}^2 to a value of $\chi_{min}^2 + 1$. In this case, the error is asymmetric. The $\langle x_E \rangle_{B^0}$ can therefore be estimated from the measured ϵ_b using the relationship shown in Figure 3.7.

The $x_E(D^*l)$ spectra for the Monte Carlo samples generated with ϵ_b are shown in Figure 7.2 for the D^*e , $D^*\mu$ and $D^*l(l = e, \mu)$ samples respectively. The corresponding measured $x_E(D^*l)$ distributions obtained from the data are also shown together.

7.4 Correcting for the D^{**} effect

When a D^{**} decays into a D^* and a pion, the pion, which is not included in the reconstruction of B^0 , takes away energy and softens the energy spectrum of the D^*l system. In the previous Chapter, when using the corrected B^0 energy to measure the $x_E(B^0)$ spectrum, the invariant mass of the D^*l , namely M_{D^*l} , is also small when the E_{D^*l} is small. Since the energy of the B^0 is estimated by $E_{D^*l}M_{B^0}/M_{D^*l}$, the effect due to the unreconstructed pion energy from the D^{**} is partially cancelled out by the ratio of E_{D^*l}/M_{D^*l} . Therefore, only a small systematic error is obtained in Chapter 6 for the D^{**} correction. However, for the method described in this Chapter, the effect due to the D^{**} will be different from that of the previous method.

For this method, only the D^*l energy is used with no mass correction. There is no cancelling effect from the E_{D^*l}/M_{D^*l} . Moreover, since this method is highly dependent on the $x_E(D^*l)$ distribution for the B^0 decay from the GOPAL Monte Carlo distributions which *does not* simulate the D^{**} decay, this systematic error is expected to be larger. Again, two Monte Carlo samples are generated by JETSET. One sample assumes that no D^* is from the D^{**} decay with its scaled mean energy is denoted as $\langle x_E \rangle^*$; the other sample assumes that 100% of the D^* s are from the D^{**} decay, and has a scaled energy $\langle x_E \rangle^{**}$. The percentage difference in $\langle x_E \rangle$ is then:

$$\delta \langle x_E \rangle = \frac{\langle x_E \rangle^* - \langle x_E \rangle^{**}}{\langle x_E \rangle} = 6.1\%$$

If it is assumed that 15% of the D^* s are from D^{**} s, the measured $\langle x_E \rangle_{B^0}$ obtained from fitting the Monte Carlo distribution with no D^{**} s can be corrected as:

$$\langle x_E \rangle_{B^0}^{corr} = 85\% \langle x_E \rangle_{B^0} + 15\%(1 + 6.1\%) \langle x_E \rangle_{B^0}$$

which gives the correction to $\langle x_E \rangle_{B^0}$ of about +0.0066 on average for each of the sample. The corresponding value of ϵ_b is also corrected accordingly for each of the $D^*\mu$, D^*e , and combined D^*l samples. Results are in Table 7.3.

The final results of the measured values for the corrected ϵ_b and $\langle x_E \rangle_{B^0}$ after the systematic error study are presented in Table 7.3 in the next section

7.5 The Systematic Error study

The systematic errors for this method which arise from the fitting procedure and the lepton identification efficiency are the same as those for the method in Chapter 6. Since no correction for the missing energy is estimated, there is no systematic uncertainty from this source.

The systematic error due to the uncertainty on the fraction of the D^* coming from the D^{**} compared to the total decay rate of $B^0 \rightarrow D^*$ is estimated. It was done by varying this fraction from 15% up to 40% and down to 3% which results in a change of +0.011 and -0.0055, on average, to the corrected $\langle x_E \rangle_{B^0}$ for each of the samples (D^*e , $D^*\mu$, D^*l).

When estimating the systematic errors on ϵ_b for the combined sample of D^*e and $D^*\mu$, the uncertainties from all the sources for each of the samples are added in quadrature. For $\langle x_E \rangle_{B^0}$, the first two systematic errors common to both are counted only once while the uncertainties due to the different lepton identification procedures for the D^*e and $D^*\mu$ samples are added in quadrature. The systematic errors for this analysis are summarized in Table 7.4 and Table 7.5.

Given the value of ϵ_b and its uncertainty, the mean value of $x_E(B^0)$ together with its errors can be calculated from the relationship shown in Figure 3.7 in Chapter 3. The measured ϵ_b and corresponding $\langle x_E \rangle_{B^0}$ are presented in Table

result	$D^*\mu$	D^*e	$D^*l(l = e, \mu)$
ϵ_b^{corr}	$0.0059^{+0.0098+0.0007}_{-0.0046-0.0014}$	$0.0037^{+0.0090+0.0006}_{-0.0036-0.0011}$	$0.0041^{+0.0070+0.0009}_{-0.0033-0.0018}$
$\langle x_E \rangle_{B^0}^{corr}$	$0.704^{+0.044+0.011}_{-0.046-0.006}$	$0.723^{+0.039+0.011}_{-0.056-0.006}$	$0.719^{+0.034+0.011}_{-0.046-0.006}$

Table 7.3: The results from fitting the Monte Carlo simulated $x_E(D^*l)$ spectrum to that of the data after correcting for the small systematic shift described in Section 7.4.

7.3. The first error shows the statistical uncertainty and the second systematic uncertainty.

	-	+	-	+
fraction of D^* from D^{**}				
and down to 3%				
Fitting method	0.0014	0.0010	0.11	0.15
lepton identification efficiency for electron ($\pm 5\%$)[38]	0.0005	0.0005	0.05[38]	0.05[38]
TOTAL	0.006	0.011	1.1	1.6

Table 7.4: Change in the $\langle x_E \rangle_{B^0}$ and the Peterson parameter ϵ_b from various source for systematic error study.

Systematic error(D^*e sample)	$\Delta \langle x_E \rangle_{B^0}$		$\Delta \epsilon_b(10^{-3})$	
	-	+	-	+
fraction of D^* from D^{**} variation from 15% to 40% and down to 3%	0.0055	0.011	1.1	0.6
fitting method	0.0014	0.0010	0.11	0.15
lepton identification efficiency for electron ($\pm 5\%$)[38]	0.0005	0.0005	0.05[38]	0.05[38]
TOTAL	0.006	0.011	1.1	0.6

Table 7.4: Change in the $\langle x_E \rangle_{B^0}$ and the Peterson parameter ϵ_b from various source for systematic error study.

Systematic error ($D^*\mu$ sample)	$\Delta \langle x_E \rangle_{B^0}$		$\Delta \epsilon_b (10^{-3})$	
	-	+	-	+
fraction of D^* from D^{**} variation from 15% up to 40% and down to 3%	0.0055	0.011	1.4	0.7
fitting method	0.0014	0.0010	0.13	0.18
lepton identification efficiency for muon ($\pm 3\%$) [38]	0.0008	0.0026	0.10[38]	0.10[38]
TOTAL	0.006	0.011	1.4	0.7

Table 7.5: Change in the $\langle x_E \rangle_{B^0}$ and the Peterson parameter ϵ_b from various source for systematic error study.

Figure 7.1: The calculated χ^2 with respect to the Peterson parameter ϵ_b . Each value of χ^2 is obtained from fitting the $x_E(D^*)$ spectrum ($D^*\mu$, D^*e and combined $D^*(l = e, \mu)$ samples), for the data and each of the Monte Carlo with specific ϵ_b .

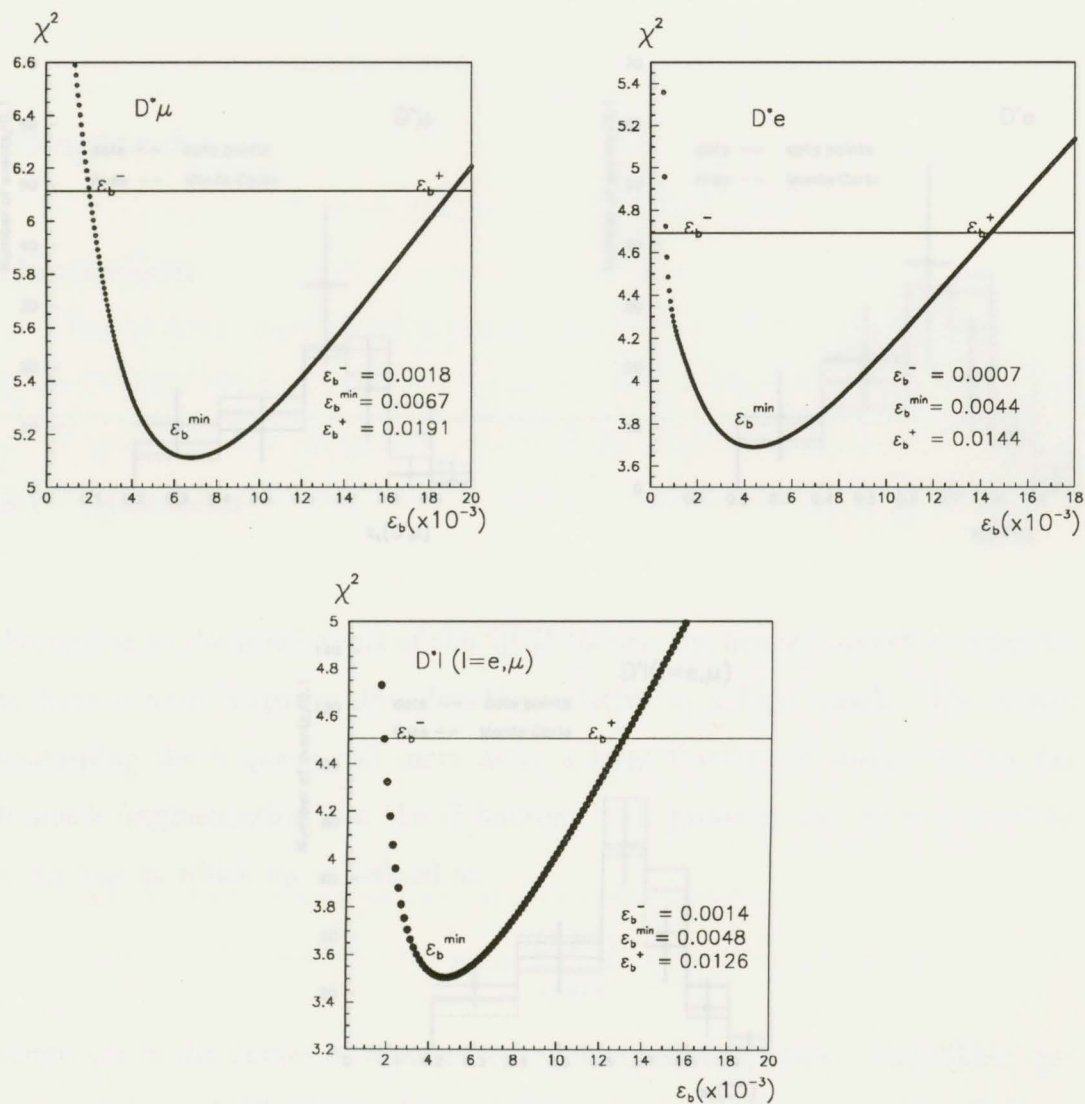


Figure 7.1: The calculated χ^2 with respect to the Peterson parameter ϵ_b . Each value of χ^2 is obtained from fitting the $x_E(D^*l)$ spectrum ($D^*\mu$, D^*e and combined D^*l ($l = e, \mu$) samples), for the data and each of the Monte Carlo with specific ϵ_b^i . (dash line) and ϵ_b^j (dash-dot line), where ϵ_b^j , ϵ_b^{\min} , ϵ_b^i are obtained by the fit described in the text.

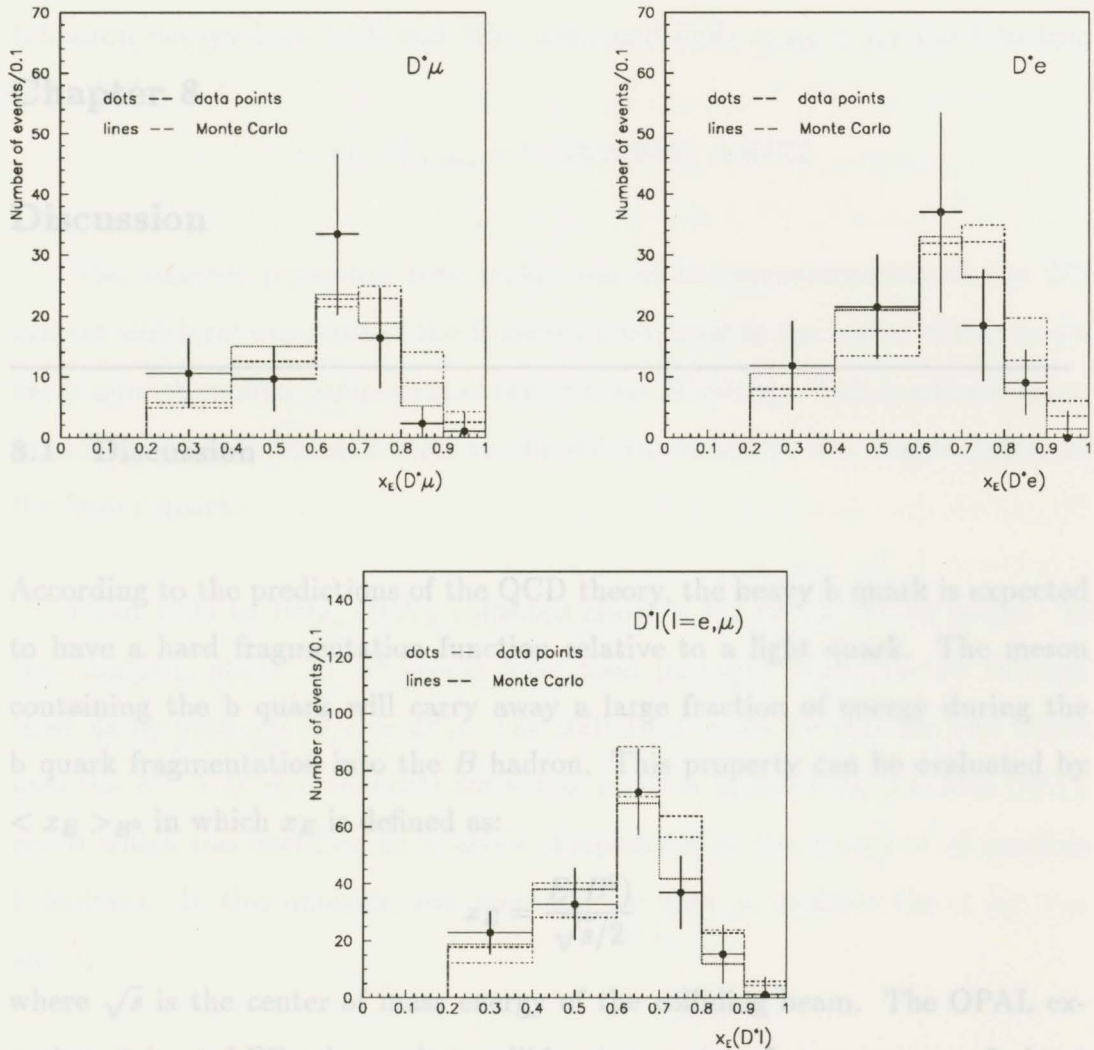


Figure 7.2: The $x_E(D^*l)$ distributions for $D^*\mu$, D^*e and $D^*l(l = e, \mu)$ samples respectively. The dots show the measurements from data. The histograms show the shape of the distributions simulated by Monte Carlo with ϵ_b being ϵ_b^- (dotted line), ϵ_b^{min} (dash line) and ϵ_b^+ (dash-dot line), where ϵ_b^- , ϵ_b^{min} , ϵ_b^+ are obtained by the fit described in the text.

fragmentation function by the OPAL collaboration uses only the muons from b-hadron decays from 1990 and 1991 data, and finds $\langle x_E \rangle$ for the b-hadron

Chapter 8

$$\langle x_E \rangle_{B^0} = 0.726 \pm 0.007 \pm 0.023$$

Discussion

The analysis presented here makes use of the reconstruction of the D^*l system which retains most of the B energy compared to the lepton which would carry a much smaller component of the original B^0 energy. This is advantageous

8.1 Discussion

According to the predictions of the QCD theory, the heavy b quark is expected to have a hard fragmentation function relative to a light quark. The meson containing the b quark will carry away a large fraction of energy during the b quark fragmentation into the B hadron. This property can be evaluated by $\langle x_E \rangle_{B^0}$ in which x_E is defined as:

$$x_E = \frac{E(B^0)}{\sqrt{s}/2}$$

where \sqrt{s} is the center of mass energy of the colliding beam. The OPAL experiment is at LEP where e^+e^- collide at a center-of-mass energy of about 91.65 GeV, which is on the Z^0 resonance.

The results were shown in Table 6.7 in Chapter 6. The measurement agrees

The measured energy of the B^0 is obtained through the reconstruction of its decay products, the D^* and a lepton (e or μ), and a correction for the missing energy due to the undetected neutrino. A previous measurement of the

fragmentation function by the OPAL collaboration uses only the muons from b-hadron decays from 1990 and 1991 data, and finds $\langle x_E \rangle$ for the b-hadron to be [14] :

$$\langle x_E \rangle_{b \text{ hadron}}^{\mu} = 0.726 \pm 0.007 \pm 0.022$$

The analysis presented here makes use of the reconstruction of the D^*l system which retains most of the B energy compared to the lepton which would carry a much smaller component of the original B^0 energy. This is advantageous in reducing the systematic error in the determination of the fragmentation of the heavy quark.

From 1990 to 1992, OPAL collected about 1,382,720 $Z^0 \rightarrow q\bar{q}$ events. In this analysis, about 75 B^0 events have been partially reconstructed through their decay products D^*e or $D^*\mu$. The statistical errors for this analysis which uses the $B^0 \rightarrow D^*e(\mu)$ channels are not as small as those of the previous OPAL result which was based on an analysis of leptons from the decays of *all* possible b hadrons. In this analysis, two methods are used to measure the $\langle x_E \rangle_{B^0}$ and ϵ_b .

- Using the corrected B^0 energy.

The results were shown in Table 6.7 in Chapter 6. The measurement agrees with the previous OPAL measurement within one standard deviation. The largest systematic error is contributed by the estimator used to correct for the missing neutrino energy. Nevertheless, the systematic errors are

comparable to the previous OPAL result.

The fragmentation process of a heavy quark must be calculated by non-perturbative QCD which is still under development. At present, this mechanism can only be investigated through the comparison of the experimental measurements with the theoretical predictions. The Peterson fragmentation function is so far the most widely used function which describes the fragmentation of the heavy quarks (b-quarks and c-quarks). The *only* parameter in the function is ϵ_b , which depicts the hardness and sharpness of the $x_E(B^0)$ spectrum. Using the corrected B^0 energy is advantageous in that it shows the shape of the fractional energy spectrum for the B^0 meson. It clearly indicates that the Peterson fragmentation function is indeed a good description of the fragmentation of the heavy quarks. The value of $\langle x_E \rangle_{B^0}$ is very sensitive to the changes in ϵ_b .

The results for ϵ_b yield the estimations of z to be:

$$\langle z \rangle_\mu = 0.948^{+0.001}_{-0.007}$$

$$\langle z \rangle_e = 0.926^{+0.014}_{-0.0205}$$

and with the combined sample,

$$\langle z \rangle_{e,\mu} = 0.941^{+0.008}_{-0.011}$$

Additional errors will be introduced into the final estimation of $\langle z \rangle$ when one determines $\langle z \rangle$ using ϵ_b which comes from the direct measurement of $x_E(B^0)$. The errors will propagate and a more detailed effort

should be made in order to accurately estimate these effects. Moreover, understanding the relationship between $\langle z \rangle$ and $\langle x_E \rangle_{B^0}$ requires a better knowledge of non-perturbative QCD which is still under development.

■ Using only the D^*l energy

The largest systematic error introduced by the forementioned method is removed by using the fractional energy distribution of x_{D^*l} (Chapter 7). The result is shown in Table 7.3. The results obtained show a smaller systematic error on $\langle x_E \rangle_{B^0}$ and ϵ_b compared to the previous OPAL result.

Given the values for ϵ_b , the corresponding values for $\langle z \rangle$ are then measured to be:

$$\langle z \rangle_{\mu} = 0.922^{+0.019}_{-0.039}$$

$$\langle z \rangle_e = 0.946^{+0.015}_{-0.034}$$

and for the combined sample,

$$\langle z \rangle_{e,\mu} = 0.925^{+0.016}_{-0.036}$$

Published measurements [39, 40, 41, 14] of $\langle x_E \rangle$ for primary b hadrons are given in Table 8.1. The results obtained from this analysis for both methods used are also summarized in Table 8.2 and Table 8.3.

A comparison of the results presented in this analysis for the fragmentation measurement with those obtained from four experiments at LEP (ALEPH,

Experiment	$\langle x_E \rangle$
ALEPH e and μ [39]	$0.67^{+0.04}_{-0.03}$
DELPHI e and μ [40]	$0.69^{+0.02}_{-0.03} \pm 0.01$
L3 e and μ [41]	$0.686 \pm 0.006 \pm 0.016$
OPAL μ [14]	$0.726 \pm 0.007 \pm 0.022$
OPAL single-lepton and dilepton [38]	$0.697 \pm 0.006 \pm 0.011$

Table 8.1: Published fragmentation measurements.

DELPHI, L3 and OPAL) is also shown in Figure 8.1. All the previous measurements presented here use solely leptons (e or μ) to extrapolate the b fragmentation while in this analysis D^*l is used. The solid part of the error bar shows the statistical uncertainty while the dotted parts are the systematic errors. The ALEPH analysis has combined the statistical error with the systematic error. The L3 detector has a very high efficiency to detect leptons, which results in a small statistical error. The first OPAL result listed used muons from b-flavoured hadron decay for 1990 and 1991 data. Another OPAL result is also quoted for an analysis from the $B^0 - \bar{B}^0$ mixing measurement which uses single-lepton and dilepton events and includes 1992 data as well. The two previous measurements from OPAL are compatible within the errors.

The results from this analysis for both methods are also shown for the $D^*\mu$, D^*e , and the combined samples respectively. The separate results are statistically limited; Combining the $D^*\mu$ and the D^*e samples increases the statistics. The results from the two methods used in this analysis are compatible. The systematic error on $\langle x_E \rangle_{B^0}$ and ϵ_b using the $x_E(D^*l)$ spectrum is smaller

<i>result</i>	$D^*\mu$	D^*e	$D^*l(l = e, \mu)$
ϵ_b^{corr}	$0.0003^{+0.0015+0.0013}_{-0.0002-0.0017}$	$0.0055^{+0.0058+0.0048}_{-0.0034-0.0023}$	$0.0019^{+0.0028+0.0026}_{-0.0018-0.0051}$
$\langle x_E \rangle_{B^0}^{corr}$	$0.776^{+0.029+0.018}_{-0.032-0.013}$	$0.707^{+0.032+0.027}_{-0.035-0.011}$	$0.741^{+0.025+0.032}_{-0.028-0.016}$

Table 8.2: The results for the $\langle x_E \rangle_{B^0}$ and ϵ_b measurement for the D^*e , the $D^*\mu$ and the combined samples using the corrected B^0 energy.

<i>result</i>	$D^*\mu$	D^*e	$D^*l(l = e, \mu)$
ϵ_b^{corr}	$0.0059^{+0.0098+0.0007}_{-0.0046-0.0014}$	$0.0037^{+0.0090+0.0006}_{-0.0036-0.0011}$	$0.0041^{+0.0070+0.0009}_{-0.0033-0.0018}$
$\langle x_E \rangle_{B^0}^{corr}$	$0.704^{+0.044+0.011}_{-0.046-0.006}$	$0.723^{+0.039+0.011}_{-0.056-0.006}$	$0.719^{+0.034+0.011}_{-0.046-0.006}$

Table 8.3: The results from fitting the Monte Carlo simulated $x_E(D^*l)$ spectrum to that of the data after correcting for the small systematic shift described in Section 7.4.

than that of the previous measurements. Within one standard deviation, our result is in excellent agreement with the previous results at LEP and particularly, with the previous OPAL result.

Figure 8.1: The comparison of various LEP measurements of the fragmentation of b-quarks, $\langle x_E \rangle_b$, to the $\langle x_E \rangle_{B^0}$ obtained by this analysis. All the previous results at LEP use solely leptons from b-hadron decays while in this analysis, the D^*l system has been reconstructed to estimate the energy of the B^0 meson. The statistical errors are shown with solid lines, while dotted lines represent systematic uncertainties. The solid vertical line shows the result from the previous OPAL measurement.

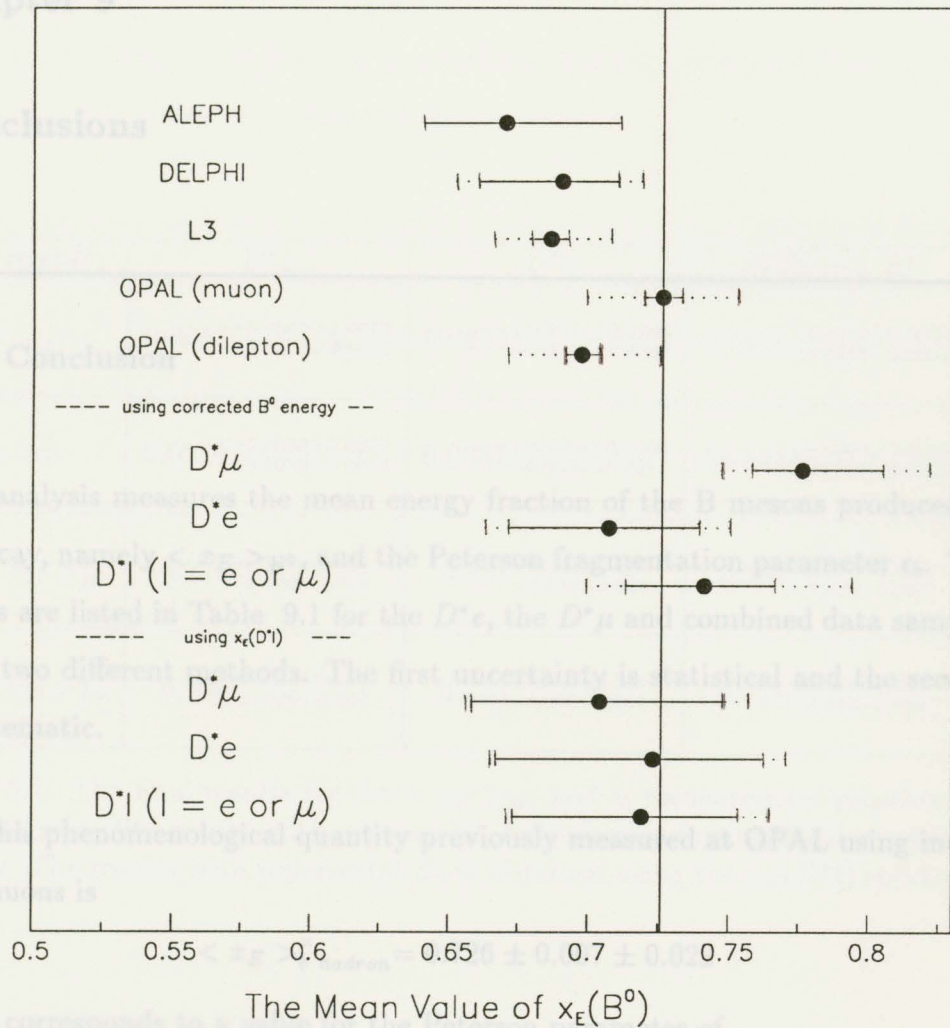


Figure 8.1: The comparison of various LEP measurements of the fragmentation of b -quarks, $\langle x_E \rangle_b$, to the $\langle x_E \rangle_{B^0}$ obtained by this analysis. All the previous results at LEP use solely leptons from b -hadron decays while in this analysis, the D^*l system has been reconstructed to estimate the energy of the B^0 meson. The statistical errors are shown with solid lines, while dotted lines represent systematic uncertainties. The solid vertical line shows the result from the previous OPAL measurement.

Chapter 9

Conclusions

9.1 Conclusion

This analysis measures the mean energy fraction of the B mesons produced in Z^0 decay, namely $\langle x_E \rangle_{B^0}$, and the Peterson fragmentation parameter ϵ_b . The results are listed in Table 9.1 for the D^*e , the $D^*\mu$ and combined data samples using two different methods. The first uncertainty is statistical and the second is systematic.

This phenomenological quantity previously measured at OPAL using inclusive muons is

$$\langle x_E \rangle_{b \text{ hadron}}^\mu = 0.726 \pm 0.007 \pm 0.022$$

which corresponds to a value for the Peterson parameter of

$$\epsilon_b = 0.0035$$

The value predicted by the theory is in good agreement with the measurement obtained by this analysis (the two values differ by approximately 1σ). This

measurement implies that the b quark has a very hard fragmentation and thus carries away a large portion of the available beam energy from the primary quark during its hadronization process into a B meson. It also shows that the Peterson fragmentation function successfully describes the hard fragmentation of the b -quark, using the parameter ϵ_b .

In summary, both the $\langle x_E \rangle_{B^0}$ and ϵ_b measurements are in excellent agree-

result	$D^*\mu$	D^*e	$D^*l(l = e, \mu)$
ϵ_b^1	$0.0003^{+0.0015+0.0013}_{-0.0002-0.0017}$	$0.0055^{+0.0058+0.0048}_{-0.0034-0.0023}$	$0.0019^{+0.0028+0.0026}_{-0.0018-0.0051}$
ϵ_b^2	$0.0059^{+0.0098+0.0007}_{-0.0046-0.0014}$	$0.0037^{+0.0090+0.0006}_{-0.0036-0.0011}$	$0.0041^{+0.0070+0.0009}_{-0.0033-0.0018}$
$\langle x_E \rangle_{B^0}^1$	$0.776^{+0.029+0.018}_{-0.032-0.013}$	$0.707^{+0.032+0.027}_{-0.035-0.011}$	$0.741^{+0.025+0.032}_{-0.028-0.016}$
$\langle x_E \rangle_{B^0}^2$	$0.704^{+0.044+0.011}_{-0.046-0.006}$	$0.723^{+0.039+0.011}_{-0.056-0.006}$	$0.719^{+0.034+0.011}_{-0.046-0.006}$

Table 9.1: The final results for the $\langle x_E \rangle_{B^0}$ and ϵ_b measurement presented in this analysis. The results with superscript **1** are obtained using the corrected B^0 energy. The results with superscript **2** are obtained using the $x_E(D^*l)$ spectrum.

measurement implies that the b quark has a very hard fragmentation and thus carries away a large portion of the available beam energy from the primary quark during its hadronization process into a B meson. It also shows that the Peterson fragmentation function successfully describes the hard fragmentation of the b-quark, using the parameter ϵ_b .

In summary, both the $\langle x_E \rangle_{B^0}$ and ϵ_b measurements are in excellent agreement with the previous LEP measurements. Using the $x_E(D^*l)$ spectrum to derive $\langle x_E \rangle_{B^0}$ and ϵ_b , the systematic errors are compatible with the previous measurements at LEP. The previous techniques only measured b-hadron fragmentation, while this analysis specifically measures B^0 fragmentation, and uses a different technique.

4. S.L. Glashow, J. Iliopoulos and L. Maiani, *Phys. Rev. D*2(1970)1285.
5. S. Weinberg, *Phys. Rev. Lett.* 19 (1967) 1264.
6. A. Salam, *Elementary Particle Theory*, Ed. N. Svartholm, (Almqvist and Wiksells, Stockholm, 1969) 367.
7. Kobayashi and Maskawa, *CP violation in the renormalizable theory of weak interaction.*, *Prog. Theor. Phys* 49 (1973)
8. M. Aguilar-Bonitez et al. *Review of Particle Properties*, *Physical Review D* 45 (1992).
9. G. Arnison et al., *Phys. Letters* 122B, (1983) 103
10. Henning Schröder, DESY, *Physics of B mesons*, *Rept. Prog. Phys.* 52, 765, 1989.

Bibliography

1. G.Kane, *Modern Elementary Particle Physics*, Addison Wesley, 1987.
2. E.Fermi, *Nuovo Cimento* **11** (1934)1.
3. Donald H. Perkins, *Introduction to High Energy Physics*, Addison Wesley, 1987.
4. S.L.Glashow, J.Iliopoulos and L.Maiani,, *Phys.Rev.* **D2**(1970)1285.
5. S. Weinberg, *Phys. Rev. Lett.* **19** (1967) 1264.
6. A. Salam, *Elementary Particle Theory*, Ed. N. Svartholm, (Almqvist and Wiksells, Stockholm, 1969) 367.
7. Kobayashi and Maskawa, *CP violation in the renormalizable theory of weak interaction.*, *Prog. Theor. Phys.***49** (1973)
8. M. Aguilar-Benitez et al. *Review of Particle Properties*, *Physical Review D* **45** (1992).
9. G.Arnison *et al.*, *Phys.Letters* **122B**, (1983) 103
10. Henning Schröder, DESY, *Physics of B mesons*, *Rept. Prog. Phys.* **52**, 765, 1989.

11. S. W. Herb et al., Phys. Rev. Lett. **39**, (1977) 252
12. OPAL collaboration, *Updated measurement of the B^0 and B^+ lifetimes* Physics Note-106. (internal OPAL document)
13. C. Peterson, D. Schlatter, I. Schmitt and P. M. Zerwas, Phys. Rev. **D 27** (1983) 105.
14. M.Z.Akrawy et al., Phys. Lett. **B263** (1991) 311. This OPAL result uses inclusive muons only.
15. The OPAL Collaboration, *The OPAL Detector at LEP*, Nuclear Instrumentation and Methods **A 305** (1991) 275.
16. OPAL Primer, internal OPAL document.
17. U.Fano, Ann. Rev. Nucl. Sci. **13**, 1 (1963).
18. A.H.Walenta, Physica Scripta **23** (1981) 354.
19. T. Sjöstrand; Computer Phys. Comm. **39** (1986) 347.
20. P. Mättig, *The Structure of Jets in the e^+e^- Collisions*, Published in Phys. Rept. 177:141, 1989.
21. J. D. Bjorken, Phys. Rev. **D 17** (1978) 171.
22. M.Suzuki, Phys. Lett. B **71** (1977) 139.
23. T. Sjöstrand et al, Pythia 5.6 and JETSET 7.3 Physics and Manual, CERN-TH.6488/92.

24. GOPAL Primer, internal OPAL document.
25. The OPAL Collaboration, P. D. Acton et al. *Measurement of $B^0 - \bar{B}^0$ Mixing in Hadronic Z^0 Decays* Phys. Letters **B276** (1992) 379-392.
26. The OPAL Collaboration, G. Alexander et al., *Zeit f. Physik C* **52** (1991) 175.
27. The OPAL Collaboration, M. Z. Akrawy et al., *A Study of Heavy Flavour Production using Muons in Hadronic Z^0 Decays* Phys. Lett. **B 263** (1991) 311-324.
28. The OPAL Collaboration, P. Acton et al. *Measurement of the B^0 and B^+ Lifetimes* Physics Lett. **B 307** (1993) 247 - 261.
29. The OPAL Collaboration, P. Acton et al., *A Measurement of Electron Production in Hadronic Z^0 Decays and a Determination of Gamma (Z^0 to $b\bar{b}$)* Zeitschrift fuer Physik **C 55** (1992) 191-207.
30. Louis Lyons and Wade Allison, *Maximum Likelihood or Extended Maximum Likelihood*, NIM **A 245**, 530, 1986.
31. The OPAL collaboration, *A Measurement of B meson production and lifetime Using Dl^- events in Z^0 decays*, CERN-PPE/92-174.
32. The OPAL collaboration, *Update of a study of $D^{*\pm}$ production in Z^0 decays*; PN064-92.
33. OPAL collaboration, *A Study of $D^{*\pm}$ Production in Z^0 decays*. Phys. Letter **B 262**, 1991.

34. R. Kowalewski, *A method for estimating γ_B in $B_s \rightarrow D_s l \nu$ decays*. OPAL Technical Note TN138.
35. L. Lyons, *Statistics for Nuclear and Particle Physicists*, University of Cambridge, 1986.
36. G. Altarelli et al. Nucl. Phys. **B 208** (1982) 365.
37. Isgur et al., Phys. Rev. **D 39** (1989) 799.
38. R. Akers et al., Zeit. f. Physik **C 60** (1993) 199-216
39. ALEPH Collaboration Phys. Lett. **B 244** (1990) 551.
40. DELPHI Collaboration, *Measurement of the partial width of the Z^0 into $b\bar{b}$ final states using their semi-leptonic decays*, CERN-PPE/92-79, submitted to Z. Phys C.
41. L3 Collaboration, Phys. Lett. **B 271** (1991) 461.

Glossary

-
- $\alpha_s(Q^2)$: The coupling constant for the strong interaction. It is a function of the momentum transfer (Q) in the interaction.
 - **boson** : Particle with integer spin.
 - B^0 meson : Meson formed by bound state of a \bar{b} quark and a d-quark in a configuration with no spin, no orbital angular momentum.
 - χ^2 fit : A method for finding the optimum fit to the data by minimizing the weighted sum of squares of deviations (χ^2).
 - **CERN** : European Laboratory for Particle Physics.
 - dE/dx : Energy loss per unit length (dE/dx) of a charged particle, transversing a medium, due to ionization. It is used to identify particle species.
 - dE/dx weight : The probability for a measured track to be identified as a specific particle obtained by comparing the dE/dx measurements to the theoretical predictions of the dE/dx for this specific particle.
 - D^0 meson : Meson formed by bound state of a \bar{u} and a c-quark, with no spin angular momentum ($S = 0$), no orbital angular momentum ($\ell = 0$).

- **D^{*+} meson** : Meson formed by bound state of a \bar{d} and a c-quark, with one unit of spin angular momentum ($S = 1$) and no orbital angular momentum ($\ell = 0$).
- **D^{**} meson** : Meson formed by bound state of a u or d quark with a c-quark, with one unit of orbital angular momentum ($\ell = 1$).
- ϵ_b : The free parameter in the Peterson fragmentation function to be determined by the experiment.
- **fermion** : Particle with half-integer spin.
- **Feynman Diagram** : A visual description of the interactions between the particles with lines representing the incoming and outgoing particles and the intermediate exchanged particles. The arrows on the quarks and leptons represent the direction, or time evolution of the interaction.
- **fragmentation** : A process by which a quark evolves into a system of colourless hadrons.
- **four-vector** : Refers to the four components of the energy and momentum of a particle ($E/c, p_x, p_y, p_z$).
- **gluon** : Neutral massless particle which mediates the strong force of Quantum ChromoDynamics.
- **GOPAL** : A software package written for the OPAL detector where the full detector response is simulated. The GOPAL data is used for background and efficiency studies.

- **hadron** : Composite object composed of 3 quarks or antiquarks (baryon) or a quark and an antiquark (meson).
- **JETSET**: A Monte Carlo simulation package from the LUND family of event generators used for the kinematic study in this analysis.
- **LEP** : Large Electron Positron collider. The LEP accelerator is 27 km in circumference and stores counter rotating electron and positron beams.
- **Loglikelihood fit** : Suppose that a set of independently measured quantities \vec{x} came from $f(\vec{x}; \vec{\theta})$, where $\vec{\theta}$ is an unknown set of parameters. The method of maximum Loglikelihood consists of finding the set of values of $\vec{\theta}$, $\hat{\theta}$, which maximizes the joint probability density for all the data.
- **Multihadron event**: Event in which the final decay products are hadrons. In this analysis, it refers to an event of the type $e^+e^- \rightarrow Z^0 \rightarrow q\bar{q}$.
- **OPAL** : Omni Purpose Apparatus at LEP. The name of the detector used for collecting data for this analysis.
- **Peterson fragmentation function** : A widely used parametrization function to describe the heavy quark fragmentation.
- **photon** : Neutral massless particle which mediates the electromagnetic force.
- **QCD** : Quantum ChromoDynamics, the theory that describes strong interaction.

- **right-sign combination** : A charge combination of $(K^\pm \pi_2^\mp) \pi_1^\pm l^\pm$ for the D^*l events.
- **Semileptonic B decay** : Weak decay of a B hadron in which the W boson decays to a lepton and a neutrino.
- **wrong-sign combination** : A charge combination of $(K^\pm \pi_2^\pm) \pi_1^\mp l^\pm$ for the background events.
- x_E : The energy of the hadron divided by the beam energy.
- z : The fraction of energy carried away by the hadron from the primary quark.
- Z^0, W boson: Massive bosons, mediators of the weak force.

X. Shen, F. Liu, X. Li, *Experimental Study on Photoelectron Statistics of ultraviolet Photon Emission from Some Living Organisms*, *Experientia* 49(1993)

Vita

Surname: Liu
Given Names: Fan
Place of Birth: Beijing, P.R.China
Date of Birth: 14th of October, 1968

Educational Institutions Attended:

Tsinghua University, Beijing, China 1986-1991

Degrees Awarded:

B.Sc. (Engineering) Tsinghua University, Beijing, China 1991

Honours and Awards:

Hedian Scholarship 1989
Hedian Scholarship 1990
Graduate Student Teaching Fellowship 1992
Graduate Student Teaching Fellowship 1993

Publications:

X. Shen, F. Liu, X. Li, *Experimental Study on Photocount Statistics of ultraweak Photon Emission from Some Living Organisms*, *Experientia* 49(1993)

April 28, 1994
(Date)

Partial Copyright License

I hereby grant the right to lend my thesis to users of the University of Victoria Library, and to make single copies only for such users, or in response to a request from the Library of any other university or similar institution, on its behalf or for one of its users. I further agree that permission for extensive copying of this thesis for scholarly purposes may be granted by me or a member of the university designated by me. It is understood that copying or publication of this thesis for financial gain shall not be allowed without my written permission.

Title of Thesis:

Measuring b-Fragmentation through the Decay $\bar{B}^0 \rightarrow D^{*+} l^- \bar{\nu}$
using the OPAL detector at CERN

Author: Fan Liu



April 28. 1994

(Date)